SYSTEM IDENTIFICATION AND CONTROL DESIGN FOR INTERNAL COMBUSTION ENGINE VARIABLE VALVE TIMING SYSTEMS By

Zhen Ren

A DISSERTATION

Submitted to
Michigan State University
in partial fulfillment of the requirements
for the degree of

DOCTOR OF PHILOSOPHY

Mechanical Engineering

2011

ABSTRACT

SYSTEM IDENTIFICATION AND CONTROL DESIGN FOR INTERNAL COMBUSTION ENGINE VARIABLE VALVE TIMING SYSTEMS

By

Zhen Ren

Variable Valve Timing (VVT) systems are used on internal combustion engines so that they can meet stringent emission requirements, reduce fuel consumption, and increase output. Also, VVT plays a critical role in order for the engine to smoothly transit between spark ignition (SI) and homogeneous charge compression ignition (HCCI) combustion modes. In order to achieve these performance benefits and SI/HCCI transition, it is required that the VVT system be controlled accurately using a model based controller. This work studies hydraulic and electric VVT system modeling and controller design.

The VVT system consists of electric, mechanical, and fluid dynamics components. Without knowledge of every component, obtaining physical-based models is not feasible. In this research, the VVT system models were obtained using system identification method. Limited by the sample rate of the crank-based camshaft position sensor, a function of engine speed, the actuator control sample rate is different from that of cam position sensor. Multi-rate system identification is a necessity for this application. On the other hand, it is also difficult to maintain the desired actuator operational condition with an open-loop control. Therefore, system identification in a closed-loop is required. In this study, Pseudo Random Binary Sequence (PRBS) *q*-Markov Cover identification is used to obtain the closed-loop model. The open-loop system model is calculated based on information of the closed-loop controller and identified closed-loop system model. Both open and closed-loop identifications are performed in a

Hardware-In-the-Loop (HIL) simulation environment with a given reference model as a validation process. A hydraulic VVT actuator system test bench and an engine dynamometer (dyno) are used to conduct the proposed multi-rate system identification using PRBS as excitation signals. Output covariance constraint (OCC) controllers were designed based upon the identified models. Performance of the designed OCC controller was compared with those of the baseline proportional integral (PI) controller. Results show that the OCC controller uses less control effort and has less overshoot than those of PI ones.

An electric VVT (EVVT) system with planetary gear system and local speed controller was modeled based on system dynamics. Simulation results of the EVVT system model provided a controller framework for the bench test. The EVVT system test bench was modified from the hydraulic VVT bench. Multi-rate closed-loop system identification was conducted on the EVVT system bench and a model based OCC controller was designed. The bench test results show that the OCC controller has a lower phase delay and lower overshoot than a tuned proportional controller, while having the same or faster response time. It is also observed that engine oil viscosity has a profound impact on the EVVT response time. The maximum response speed is saturated at a slow level if the viscosity is too high.

From the bench and dyno tests, it is concluded that multi-rate closed-loop identification is a very effective way to retrieve controller design orientated VVT models. It is possible to use an OCC controller to achieve lower energy consumption, lower overshoot, and better tracking compared to PI and proportional controllers on both hydraulic and electric VVT systems.

Copyright by ZHEN REN 2011 TO MY PARENTS AND WIFE

ACKNOWLEDGEMENTS

Completion of my dissertation and Ph.D. program would not be possible without support and help from many people.

First of all, my thanks are due to Dr. Guoming Zhu for supporting and advising my Ph.D. program in the last four years. During that period, Dr. Zhu shared his broad knowledge in theory, hands-on experience, and enthusiasm in automotive control field. As my advisor, a senior scholar and engineer, Dr. Zhu taught me not only in academic level but also in career, family, and life.

My thanks are due to Dr. Hassan Khalil, Dr. Clark Radcliffe, and Dr. Harold Schock for providing helpful and insightful discussions, comments, and serving as my Ph.D. program committee members. I have also learned a lot from the lectures these professors taught.

Most of the experiments in this dissertation require team effort. I would like to thank the staff and fellow graduate students I worked with and learned a lot from during the last four years in the Engine Research Lab. In particular: Xuefei Chen, Jeff Higel, Andrew Huisjen, Gary Keeney, Kevin Moran, Stephen Pace, Cody Squibb, Tom Stuecken, Andrew White, and Xiaojian Yang.

Thanks to all the faculty and staff members in Mechanical Engineering at Michigan State University for the classes they taught, useful suggestions to my research work, and support they provided. I enjoyed every day of my past five years here at MSU.

Finally, thanks to my parents, my wife, and my friends for encouraging me for so many years.

TABLE OF CONTENTS

List of Tablesix			
List of Figures		X	
Chapter 1 Introduction		1	
*			
1.2 Research Overview		3	
1.2.1 Control Oriented Modeli	ing	3	
	Oyno Tests		
	•		
Chapter 2 Closed-loop System Identifi	ication Framework	9	
- · ·			
2.2 Inverse PRBS		11	
2.3 Closed-loop System Identification	cation Framework	12	
2.4.1 Closed-loop Model Cont	trollers	15	
	System Identification		
	First-order System		
_	econd-order System		
*	al Order		
e e e e e e e e e e e e e e e e e e e			
Chapter 3 Hydraulic Variable Valve T	iming System Identification and Controller Design	.27	
	work		
	(OCC)		
<u>*</u>	an HIL Simulator		
	etup		
•			
•	ies		
	on		
	Model		
	gnal Input		
	with Multi-input		
	Comparison		
	nometer Test Setup		
	r		
	on Setup the Engine Dyno		
	on Results		

3.8.	3 Validation of Identified Model	65
3.8.		
3.10	Conclusion	
2.10		
Chapter	4 Electric Variable Valve Timing System Modeling and Controller Design	74
4.1	Introduction	74
4.2	Modeling	77
4.2.	1 Planetary VVT Components	77
4.2.	2 Planetary Gear System Kinematics	78
4.2.		
4.2.		
4.3	Controller Design	84
4.3.	1 Control Design Parameters	84
4.3.	2 Feedforward Controller	86
4.3.	3 Baseline Controllers	86
4.3.	4 OCC feedback Controller	87
4.4	Simulation and Results	87
4.5	The Electric VVT Bench Setup	90
4.6	Electric VVT System Test the Test Bench	92
4.6.	1 Closed-loop Identification for Electric VVT System on Test Bench	92
4.6.	2 Control Design for Electric VVT System Test Bench	93
4.6.		
4.7	Engine Oil Viscosity	103
4.8	Conclusion	106
Chapter	5 Conclusions and Future Works	108
5.1	Conclusions	
5.2	Suggestions for Future Works	109
Bibliogr	anhy	111

LIST OF TABLES

Table 2-1. Nonzero coefficients of PRBS polynomial	11
Table 2-2: CL controllers and transfer functions of the first order plant	16
Table 2-3: CL controllers and transfer functions of the second order plant	16
Table 2-4. PRBS q-Markov COVER system ID parameters	17
Table 2-5. Identified closed/open-loop models for the first-order plant	20
Table 2-6. Identified closed/open-loop models for the second-order plant	23
Table 3-1. Closed-loop PRBS q-Markov COVER system ID results	38
Table 3-2. System identification parameters	46
Table 3-3. Identified open-loop plant transfer functions	49
Table 3-4. Controller performance comparison	58
Table 3-5. Plant gains At different operating conditions	59
Table 3-6. Controller mean advance performance comparison	61
Table 3-7. Controller mean retard performance comparison	61
Table 3-8. System identification parameters for engine dyno	64
Table 3-9. Identified intake and exhaust VVT system models	65
Table 3-10. Cam phaser performance when motoring	71
Table 3-11. Cam phaser performance when combusting	71
Table 4-1. Planetary system parameters	85
Table 4-2. Output comparison at end of each cycle	89
Table 4-3. Output comparison at 1500 rpm with different sample rate	90
Table 4-4. Closed-loop identification parameters for the EVVT system	93
Table 4-5. Frequency response of close-loop EVVT system	98

LIST OF FIGURES

Figure 2-1. Closed-loop system identification framework	10
Figure 2-2. Frequency response of identified and original first-order models	14
Figure 2-3. Frequency response of identified and original second-order models	15
Figure 2-4. First-order OL models with a proportional controller in all setups	18
Figure 2-5. First-order OL models with a first order controller in all setups	19
Figure 2-6. First-order OL models with a PI controller in three setups	21
Figure 2-7. Second-order OL models with a proportional controller in all setups	22
Figure 2-8. Second-order OL models with a first-order controller in all setups	24
Figure 2-9. Second-order OL models with a PI controller in three setups	24
Figure 2-10. Effect of PRBS order	25
Figure 3-1. Closed-loop identification framework	30
Figure 3-2. Closed-loop identification framework on an HIL simulator	37
Figure 3-3. Identified model frequency responses of the HIL simulator	38
Figure 3-4. Identified phase delay at different engine speeds	39
Figure 3-5. Identified model and physical system responses with PRBS input	40
Figure 3-6. VVT phase actuator test bench	40
Figure 3-7. VVT phase actuator test bench diagram	41
Figure 3-8. VVT system Diagram	42
Figure 3-9. Cam phase actuator open-loop step response	43
Figure 3-10. Vane type cam phase hydraulic pulley	44
Figure 3-11. Cam phase actuator open-loop steady-state responses	45
Figure 3-12. Identified and physical responses	47

Figure 3-13. Identified model order selection	47
Figure 3-14. Bode diagram of open-loop plant at 1500 rpm	48
Figure 3-15. Root locus of the identified fourth-order plant at 1000 rpm	49
Figure 3-16. Bode diagram of open-loop plant at 1000 rpm	50
Figure 3-17. Closed-loop step response comparison at 1000 rpm	51
Figure 3-18. Closed-loop step response comparison at 1500 rpm	51
Figure 3-19. Family of Identified models	52
Figure 3-20. Step response for OCC controllers	54
Figure 3-21. OCC design framework with an integrator	55
Figure 3-22. Multi-input OCC design framework	56
Figure 3-23. Step response comparison	56
Figure 3-24. Control effort comparison at 900 rpm with 45 psi oil pressure	57
Figure 3-25. Step response comparison of OCC, PI and LPV controllers	60
Figure 3-26. Control effort comparison of OCC, PI and LPV controllers	60
Figure 3-27. Single cylinder engine on the engine dyno	62
Figure 3-28. Dyno control room	63
Figure 3-29. Bode diagram for the identified VVT system models	66
Figure 3-30. Step response of the physical systems and nominal model	67
Figure 3-31. VVT system step response at 1800 rpm with combustion	69
Figure 3-32. VVT control effort on the engine dyno	70
Figure 4-1. Electric planetary gear VVT system	78
Figure 4-2. Free body diagrams of planetary gear components	80
Figure 4-3. Block diagram of electric motor with planetary gear system	83

Figure 4-4. Electric motor VVT control framework	84
Figure 4-5. Torque load for single cylinder	85
Figure 4-6. Output comparison at 1500 rpm	88
Figure 4-7. Output comparison at 2000 rpm	89
Figure 4-8. EVVT system test bench diagram	91
Figure 4-9. EVVT test bench.	91
Figure 4-10. Step response comparison on EVVT bench	95
Figure 4-11. Trajectory tracking comparison on EVVT bench	96
Figure 4-12. Frequency response of the closed-loop EVVT system	99
Figure 4-13. Measured and predicted VVT frequency response at 1000 rpm	103
Figure 4-14. Impact of engine oil viscosity on EVVT response	105

Chapter 1 Introduction

1.1 Background and Motivation

Continuously variable valve timing (VVT) systems used in internal combustion engines were developed in the nineties [1] and have since been widely used due to growing fuel economy demands and emission regulations. A VVT system is capable of changing the intake and/or exhaust valve timing(s) to the optimal positions at different operating conditions while the engine is still running. By doing so, the VVT system improves fuel economy and reduces emissions at low engine speed, as well as improves engine power and torque at high engine speed.

There are different kinds of VVT systems. Conventional electronic-hydraulic VVT ([1] and [2]), also called hydraulic VVT, is the most widely used in the industry today. The hydraulic VVT systems require minor changes when applied to a previously non-VVT valve-train [1], which makes design and engineering relatively easy. However, due to its mechanism, the hydraulic VVT system also has its limitations [3]. The response and performance of the hydraulic VVT system are significantly affected by the engine operating conditions such as engine oil temperature and pressure. For instance, at low engine temperature, the hydraulic VVT system cannot be activated and has to remain at its default position so that the cold start performance and emissions cannot be improved [3]. This leads to the study of other variable valve-train systems, such as electromagnetic [4]; hydraulic [5]; electro-pneumatic [6]; and electric motor driven planetary gear system ([7] and [8]).

Electric motor driven VVT operational performance is independent of engine oil temperature and pressure [3]. Compared to a hydraulic VVT system, an electric motor driven VVT system is less limited by engine operating conditions and therefore gives better

performance and better emission in a wider operational range. Especially, since the electric VVT (EVVT) is independent of the engine oil pressure, the response time is greatly improved. Also, the (EVVT)can be phased while the engine is not running. This allows for overlapping of the intake and exhaust valves during the engine crank start. As a result, the pumping loss can be significantly reduced when the engine starts, and the vehicle can achieve better fuel economy. This feature is particularly useful in hybrid vehicles, which involve a great number of engine stop-start cycles. The research work in this paper mainly focused on the dynamic system modeling and control design of both hydraulic and electric VVT's.

The major advantage of Homogeneous Charge Compression Ignition (HCCI) combustion is realized by eliminating the formation of flames. This results in much lower combustion temperature. As a consequence of the low temperature, the formation of NOx (nitrogen oxides) is greatly reduced. The lean burn nature of the HCCI engine also enables un-throttled operation to improve engine fuel economy. Unfortunately, HCCI combustion is feasible only over a limited engine operational range due to engine knock and misfire. To make a HCCI engine work in an automotive internal combustion engine, it has to be capable of operating at both a Spark Ignition (SI) combustion mode at high load and an HCCI combustion mode at low and medium load ([9] and [10]). This makes it necessary to have a smooth transition between SI and HCCI combustion modes.

Achieving the HCCI combustion and controlling the mode transition between SI and HCCI combustions in a practical engine require implementation of enabling devices and technologies. There are a number of options, and the necessary prerequisite for considering any of them is their ability to provide control of thermodynamic conditions in the combustion chamber at the end of compression. The range of devices under consideration include variable

valve actuation (cam-based or camless), variable compression ratio, dual fuel systems (port and direct fuel injection with multiple fuel injections), supercharger and/or turbocharger, exhaust energy recuperation and fast thermal conditioning of the intake charge mixture, spark-assist, etc. Variable Valve Actuation can be used for the control of the effective compression ratio (via the intake valve closing time), the internal (hot) residual fraction via the negative valve overlap (also called recompression), or secondary opening of the exhaust valve (residual re-induction) ([11] and [12]). In addition to providing the basic control of the HCCI combustion, i.e., ignition timing and burn rate or duration, the VVT systems plays a critical role in accomplishing smooth mode transitions from SI to HCCI and vice versa ([13] to [17]). Due to the fast response time and independence to the engine operation, the EVVT system is selected for the HCCI engine. The EVVT controls the engine valve timings when it is operated at SI and HCCI combustion modes. During the combustion mode transition, the EVVT is controlled to track a desired trajectory.

1.2 Research Overview

1.2.1 Control Oriented Modeling

There are two approaches to obtain a VVT model for control development and validation: physics based system modeling [18] and system identification. In this paper, the closed-loop system identification approach is employed to obtain the hydraulic VVT system model. In order to provide a control framework for the electric VVT system, physics-based modeling is used to obtain the electric VVT system model for simulation purposes. Closed-loop identification is used to obtain the system model on the test bench.

System identification using closed-loop experimental data was developed in the seventies [19], and it has been widely used in engineering practice ([20], [21], and [22]). Closed-loop system identification can be used to obtain the open-loop system models when the open-loop

plant cannot be excited at the conditions ideal for system identification. For instance, the open-loop plant could be unstable. In this paper, closed-loop identification was selected due to many factors. One main reason is that the system gain of a VVT actuator is a function of engine speed, load, oil pressure, and temperature, which made it impossible to maintain the cam phase at a desired value. Therefore, open-loop system identification at a desired cam phase is not practical. In order to maintain at a desired operational condition for identifying the VVT actuator system, closed-loop identification was selected.

The purpose of using closed-loop system identification is to obtain linear system models for the VVT actuator system at certain operating conditions using the indirect closed-loop system identification method that is discussed in [21]. In this paper, the *q*-Markov COVariance Equivalent Realization (*q*-Markov COVER) system identification method ([23], [24], and [25]) using Pseudo-Random Binary Signals (PRBS) was used to obtain the closed-loop system models. The *q*-Markov cover theory was originally developed for model reduction. It guarantees that the reduced order system model preserves the first *q*-Markov parameters of the original system. The realization of all *q*-Markov Covers from input and output data of a discrete time system is useful for system identification. Q-Markov Cover for system identification uses pulse, white noise, or PRBS as input excitations. It can be used to identify a linear model representing the same input/output sequence for a nonlinear system [25]. It was also been extended to identify multirate discrete-time systems when input and output sampling rates are different [26].

For the proposed study, the multi-rate system identification is required, because the actuator control signal is updated at a different sample rate from that of the cam position sensor, which is a function of engine speed. For our test bench setup, the cam position sample rate is limited to eight samples per engine cycle. That is, when the engine is operated at 1500 rpm, the

sample period is 10ms, while the control output is updated at a fixed period of every 5ms. In this paper, the multi-rate PRBS closed-loop identification was used to conduct closed-loop system identification on a VVT actuator HIL (Hardware-In-the-Loop) system for debugging and validation. The HIL simulation results show that the closed-loop identified models represent the system dynamics very well. Then, the HIL simulator was replaced by a hydraulic VVT test bench and an engine dynamometer (dyno) with hydraulic VVT. The closed-loop system identification was repeated on these systems. The test bench consists of an AC motor driven crank shaft that is connected to the cam shaft on a cylinder head through a VVT actuator. The engine on the dyno has two hydraulic VVT systems controlling both intake and exhaust valve timing. The PRBS q-Markov Cover system identification was applied to both hydraulic VVT systems, and control oriented models were obtained from the bench and dyno tests. On the test bench, the hydraulic VVT system was also identified at different operating conditions. A family of the system models was obtained and a linear parameter varying (LPV) system ([27] to [32]) was constructed. The varying parameters are functions of engine speed and engine oil pressure.

The EVVT system consists of a planetary gear train and a driving motor. Its kinematics and dynamics can be solved using the relationship of their numbers of teeth, and equations of motions. To construct a controller framework for the EVVT, the system was modeled based on physical dynamics. It is shown in this paper that an EVVT system can be modeled as a first-order dynamic in simulation. An EVVT system bench was constructed and the closed-loop identification method was used to model its dynamics.

1.2.2 Control Design

The OCC (Output Covariance Constraint) control design approach ([33], [34], and [35]) minimizes the system control effort subject to multiple performance constraints on output covariance matrices. An iterative controller design algorithm [35] with guaranteed convergence can be used to find an OCC optimal controller. Note that an OCC controller is a H_2 controller with a special output weighting matrix selected by the OCC control design algorithm. The OCC control scheme was applied to many aerospace control problems due to its minimal control effort ([33], [34], and [35]). In this paper, a nominal model was selected from the family of the identified VVT models for the OCC control design. Multiple OCC controllers were designed based upon closed-loop identified models, and their performances were compared against these of the well-tuned baseline PI controller. In order to eliminate steady-state error, system control input was increased to add an additional integral input to the system plant used for the OCC control design. A gain-scheduling controller ([36] and [37]) was also designed for the hydraulic VVT test bench based on the LPV system.

In order to control the EVVT system with planetary gears, a feedback controller was introduced ([8]). Due to the steady-state and transient control accuracy requirements of the HCCI combustion, the closed-loop electric VVT system needs not only to meet steady-state performance requirement but also to track a desired trajectory during the combustion mode transition. Therefore, a feedback controller with feedforward control was developed in Simulink environment. In a VVT system, the cam phase is the integration of speed difference between the electric VVT motor and crankshaft. This leads to using the rate of the reference cam phase as feedforward command. OCC controller was used in feedback to reduce the tracking error. For

the EVVT bench, half engine crankshaft speed was used as feedforward, and OCC controller was used as feedback.

1.2.3 Simulation, Bench and Dyno Tests

The OCC controller was tested on a test bench as well as an engine dyno with hydraulic VVT systems. Bench test results show that the OCC controllers were able to achieve the similar system settling time as the PI controller with significantly less overshoot and control effort. The LPV controller was also tested on the test bench and it has advantages of lower overshoot, lower control effort similar to the OCC controller, while having a fast response time similar to the PI controller. On the engine dyno, the feedback signal was limited to one sample per engine cycle. It is shown from the dyno test that low sample rate penalizes the OCC controller performance more than the PI controller.

Simulation and bench test results were presented for the EVVT system. In the simulation, performance of the OCC controller was compared to a well-tuned proportional-derivative (PD) controller, and the OCC with feedforward provides better cam phase tracking performance than the PD controller. Different cam phase sample rates were also studied. Simulation results show that four samples per engine cycle are sufficient for the OCC feedback controller. The OCC controller was also tested on the EVVT test bench, the test results show that the OCC controller has a superior target tracking performance than a well-tuned proportional controller. The OCC controller has a lower overshoot, same or faster response time, and lower phase delay at high frequency references than the proportional controller.

It was also observed from the EVVT bench test that the engine oil viscosity has a large impact on EVVT performance. The engine oil is used to lubricate the planetary gear system. Friction of the engine oil limits the top speed of the EVVT motor. As a result the maximum

phasing speed is limited. Two different engine oil viscosity weightings were tested on the test bench. The results show that at room temperature, the EVVT system response is 1.6 times slower using SAE 30 than using SAE 5W20 engine oil.

1.3 Organization

This dissertation is organized as the follows: Chapter 2 studies the closed-loop system identification error when a dynamic integral controller is used. Chapter 3 applies closed-loop system identification modeling to hydraulic VVT actuator systems, and model based controllers were designed based on the identified models. Chapter 4 discusses modeling, controller design and test for EVVT systems. Conclusion is provided in chapter 5, with suggestions of future works.

Chapter 2 Closed-loop System Identification Framework

2.1 Introduction

System identification using closed-loop experimental data was developed in seventies [19] and it has been widely used in engineering practice ([20], [21], and [22]). Closed-loop system identification can be used to obtain the open-loop system models when the open-loop plant cannot be excited at the conditions ideal for system identification. For instance, the open-loop plant could be unstable.

There are many approaches to identify a system model in a closed-loop framework shown in Figure 2-1. The closed-loop system identification approach falls into three main groups: direct, indirect, and joint input-output approaches [21]. The direct approach ignores the feedback loop and identifies the open-loop system using measurements of plant input and output; the indirect approach identifies the closed-loop system model and then determines the open-loop system model using the knowledge of the linear controller; and the joint input-output approach regards the input and output jointly as the output and uses certain system identification methods to obtain open-loop models. For this study, we mainly use the indirect and joint input-output approaches.

In this paper, the *q*-Markov COVariance Equivalent Realization (*q*-Markov Cover) system identification method ([23], [24], and [25]) with PRBS (Pseudo-Random Binary Signals) was used to obtain the closed-loop system models. The *q*-Markov cover theory was originally developed for model reduction. It guarantees that the reduced order model preserves the first *q*-Markov parameters of the original system. The realization of all *q*-Markov Covers from input and output data of a discrete time system is useful for system identification. Q-Markov Cover for

system identification uses pulse, white noise, or PRBS as input excitations. It has also been extended to identifying multi-rate discrete-time systems [26].

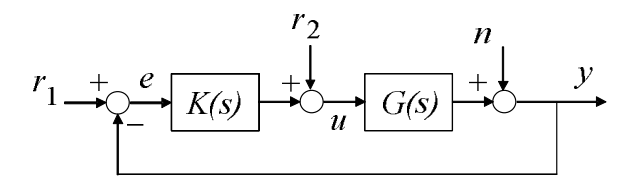


Figure 2-1. Closed-loop system identification framework

This paper was motivated by unexpected low frequency identification error of an open-loop system model when a PI (proportional and integral) controller was used for closed-loop system identification; while the low frequency identification was eliminated when the PI controller was replaced by a proportional controller. For both cases, the PRBS *q*-Markov Cover was used to obtain the closed-loop system transfer function and the open-loop system models were obtained using the indirect approach. Note that the bandwidth of a PRBS signal is bounded by its sample period at high frequency and its period (or order) at low frequency. It was also observed that the system identification error occurs at the frequency around the PRBS signal bandwidth. For this study system identification was applied to both first-order and second-order systems using open-loop system identification and closed-loop system identification with proportional, first-order dynamic, and PI controllers. The system identification results were compared and analyzed at the end of the paper. The effects of different system identification frameworks shown in Figure 2-1 were also studied.

Works introduced in this chapter can be found in [38].

The chapter is organized as the following. Section 2.2 provides the definition of the PRBS signal used in the system identification process, and Section 2.3 describes the framework and formulation of closed-loop identification. System identification results for the first and

second-order systems are provided in Section 2.4, along with the discussions of the simulation results. Conclusions are provided in Section 2.5.

2.2 Inverse PRBS

The most commonly used PRBSs are based on maximum length sequences (called *m*-sequences) [39] for which the length of the PRBS signals is $m = 2^n - 1$, where *n* is an integer (order of PRBS). Let z^{-1} represent a delay operator, and define $\hat{p}(z^{-1})$ and $p(z^{-1})$ to be polynomials

$$p(z^{-1}) = a_n z^{-n+1} \oplus \dots \oplus a_2 z^{-1} \oplus a_1 = \hat{p}(z^{-1}) z^{-1} \oplus 1,$$
 (2.1)

where a_i is either 1 or 0, and \oplus obeys binary addition, i.e.

$$1 \oplus 1 = 0 = 0 \oplus 0 \& 0 \oplus 1 = 1 = 1 \oplus 0,$$
 (2.2)

and the non-zero coefficients a_i of the polynomial are defined in the following Table 2-1.

Table 2-1. Nonzero coefficients of PRBS polynomial

Polynomial order (n)	Period of sequence (m)	Non-zero Coefficient
2	3	a1, a2
3	7	a2, a3
4	15	a3, a4
5	31	a3, a5
6	63	a5, a6
7	127	a4, a7
8	255	a2, a3, a4, a8
9	511	a5, a9
10	1023	a7, a10
11	2047	a9, a11

Then the PRBS can be generated by the following formula:

$$\hat{u}(k+1) = \hat{p}(z^{-1})\hat{u}(k), \quad k = 0, 1, 2, \dots,$$
(2.3)

where $\hat{u}(0) = 1$ and $\hat{u}(-1) = \hat{u}(-2) = \cdots = \hat{u}(-n) = 0$. Defined in the following sequence:

$$s(k) = \begin{cases} a; & \text{If } k \text{ is even;} \\ -a; & \text{If } k \text{ is odd.} \end{cases}$$
 (2.4)

Then, the signal

$$u(k) = s(k) \otimes [-a + 2 \ a \ \hat{u} \ (k)]$$
 (2.5)

is called the *inverse* PRBS, where \otimes obeys

$$a \otimes a = -a = -a \otimes -a \otimes a \otimes -a = a = -a \otimes a. \tag{2.6}$$

It is clear after some analysis that u has a period 2m and u(k) = -u(k+m). The mean of the inverse PRBS is

$$m_u = E_{2m}u(k) \equiv \frac{1}{2m} \sum_{k=0}^{2m-1} u(k) = 0$$
 (2.7)

and the autocorrelation ($R_{uu}(\tau) = E_{2m}u(k+\tau)u(k)$) of u is

$$R_{uu}(\tau) = \frac{1}{2m} \sum_{k=0}^{2m-1} u(k+\tau)u(k) = \begin{cases} a^2, & \tau = 0; \\ -a^2, & \tau = m; \\ -a^2/m, & \tau \text{ even}; \end{cases}$$

$$a^2/m, \quad \tau \text{ odd.}$$
(2.8)

The inverse PRBS is used in the *q*-Markov Cover identification algorithm. For convenience, in the rest of this paper, the term "PRBS" is used to represent the inverse PRBS.

2.3 Closed-loop System Identification Framework

Consider a general form of a linear time-invariant closed-loop system shown in Figure 2-1 (see [21], [22], and [40]), where r_1 is the reference signal, r_2 is an extra input, n is the measurement noise, u and y are input and output.

As discussed in the Introduction section, there are many approaches for the closed-loop identification, which are categorized as direct, indirect, and joint input-output approaches. The indirect approach utilizes the knowledge of the closed-loop controller [41] while the joint input-output approach obtains the open-loop system model using only the identified closed-loop model. In this chapter, both indirect and joint input-output approaches are used. Noise is ignored in the discussion.

The input and output relationship of the generalized closed-loop system, shown in Figure 2-1, can be expressed below

$$\mathbf{y} = \begin{bmatrix} \mathbf{H}_1 & \mathbf{H}_2 \end{bmatrix} \begin{bmatrix} \mathbf{r}_1 \\ \mathbf{r}_2 \end{bmatrix} = \begin{bmatrix} \left(\mathbf{GK} (\mathbf{I} + \mathbf{GK})^{-1} \right)^T \\ \left(\mathbf{G} (\mathbf{I} + \mathbf{GK})^{-1} \right)^T \end{bmatrix}^T \begin{bmatrix} \mathbf{r}_1 \\ \mathbf{r}_2 \end{bmatrix}$$
(2.9)

Let $\hat{\mathbf{H}}_1$ and $\hat{\mathbf{H}}_2$ be identified closed-loop transfer functions from r_1 and r_2 to y, respectively. When both excitations r_1 and r_2 are used, the open-loop system model \mathbf{G}_{ID} can be calculated using identified $\hat{\mathbf{H}}_1$ and $\hat{\mathbf{H}}_2$ (joint input-output approach); see below.

$$\mathbf{G}_{ID} = \hat{\mathbf{H}}_{2} (\mathbf{I} - \hat{\mathbf{H}}_{1})^{-1}. \tag{2.10}$$

Assuming that $(\mathbf{I} - \hat{\mathbf{H}}_1)^{-1}$ is invertible. We also consider two special cases $r_1 = 0$ and $r_2 = 0$. For both cases the indirect approach will be used, that is, the closed-loop controller transfer function is used to solve for the open-loop system models. For the case that $r_2 = 0$, we have

$$\mathbf{G}_{ID} = \hat{\mathbf{H}}_{1} (\mathbf{I} - \hat{\mathbf{H}}_{1})^{-1} \mathbf{K}^{-1}$$
 (2.11)

and for the case that $r_1 = 0$,

$$G_{ID} = \hat{H}_2 (I - K\hat{H}_2)^{-1}.$$
 (2.12)

We define system identification using (2.10) as the general setup, (2.11) as the controller setup, and (2.12) as the compensator setup.

2.4 Simulation Results

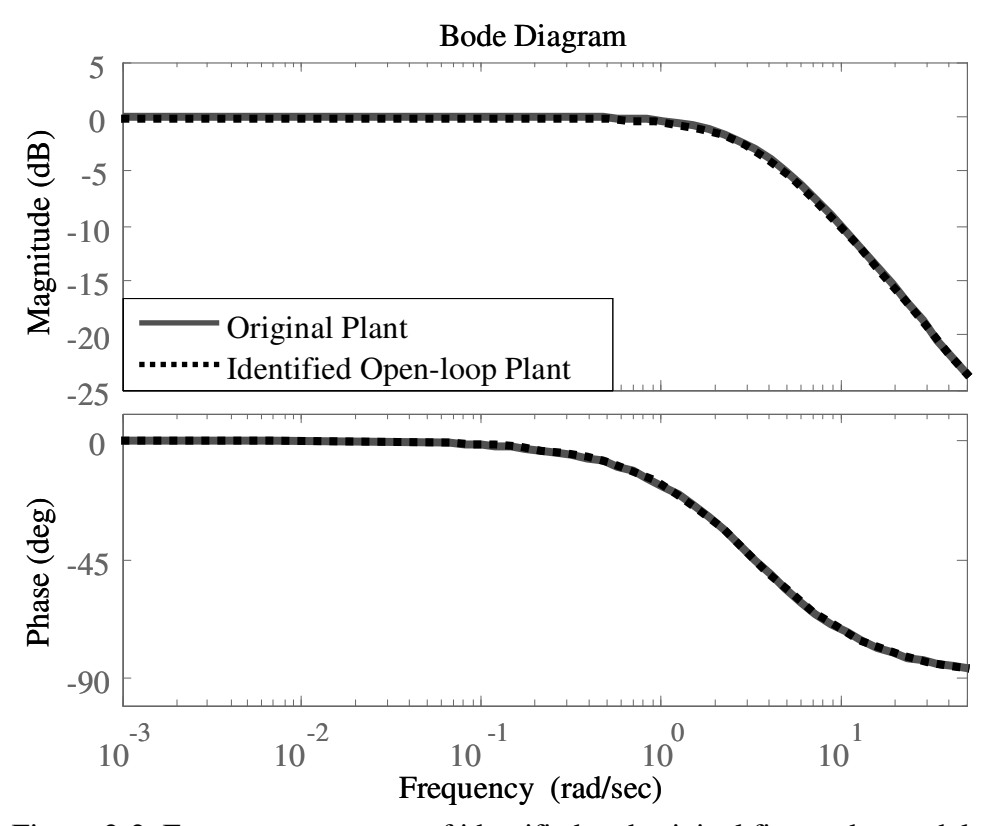


Figure 2-2. Frequency response of identified and original first-order models

To study the identification error due to integral control we selected the following first and second-order systems:

$$G_1(s) = \frac{1}{0.3s+1}$$
 and $G_2(s) = \frac{1}{s^2+s+1}$. (2.13)

PRBS q-Markov Cover was used to identify the open-loop transfer functions using r_2 as excitation by setting K(s) = 0, where the orders of the PRBS are n=8 for the first-order plant and n=11 for the second-order plant. The magnitude of PRBS is a=1 (see Table 2-1). The identified open-loop transfer functions

$$\hat{G}_{1}(s) = \frac{-6 \times 10^{-5} s + 0.984}{0.298s + 1} \text{ and}$$

$$\hat{G}_{2}(s) = \frac{-1.7 \times 10^{-5} s^{2} - 0.0037s + 0.993}{s^{2} + 0.98s + 1}$$
(2.14)

match the original plants (2.13) very well, see Figure 2-2 and Figure 2-3. Both identified and original frequency responses are almost identical.

2.4.1 Closed-loop Model Controllers

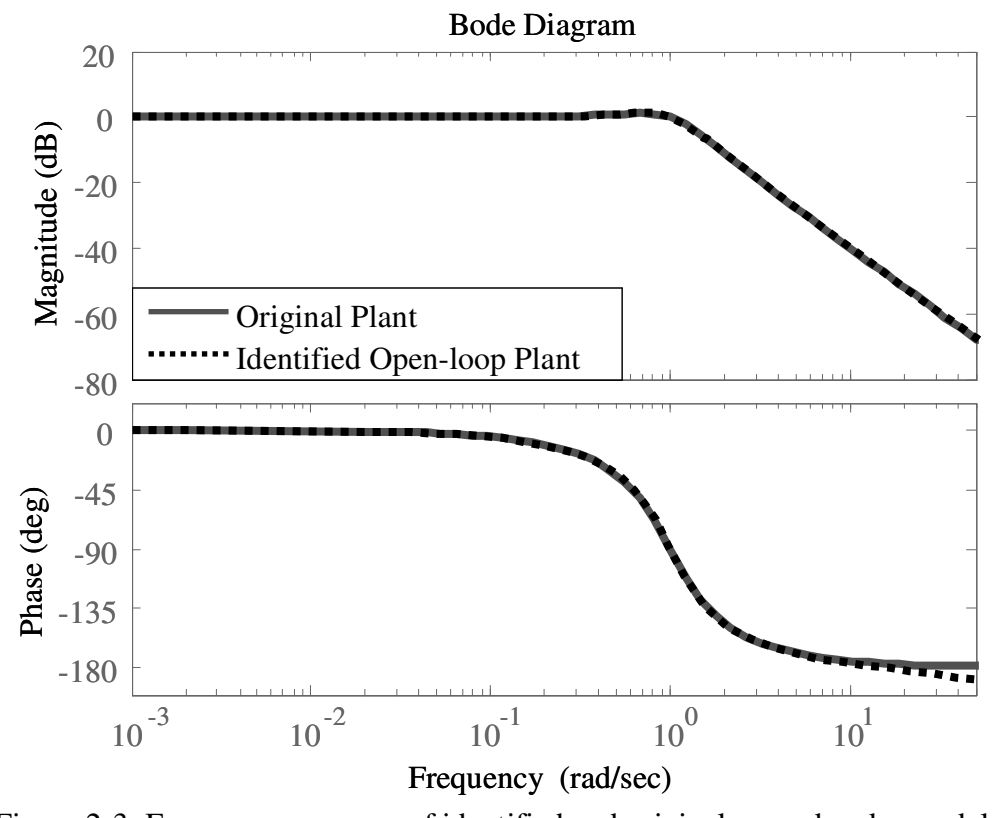


Figure 2-3. Frequency response of identified and original second-order models

Three closed-loop controllers are considered for this study. For the first-order system, they are proportional $(K_{P1}(s))$, dynamic $(K_1(s))$, and PI $(K_{PI1}(s))$ controllers shown in Table 2-2. Then, the corresponding closed-loop system can be expressed as follows.

$$y = \begin{bmatrix} H_1 & H_2 \end{bmatrix} \begin{bmatrix} r_1 \\ r_2 \end{bmatrix} = H \begin{bmatrix} r_1 \\ r_2 \end{bmatrix}, \tag{2.15}$$

where the closed-loop transfer functions (H) are provided in Table 2-2.

Table 2-2: CL controllers and transfer functions of the first order plant

Closed-loop Controllers				
$K_{P1}(s) = 0.2$	$K_1(s) = \frac{s + 0.5}{s + 1}$	$K_{PI1}(s) = \frac{0.2s + 5}{s}$		
Corresponding Closed-Loop Transfer Functions H^T				
$\begin{bmatrix} \frac{0.2}{0.3s+1.2} \\ \frac{1}{0.3s+1.2} \end{bmatrix}$	$\begin{bmatrix} \frac{s+0.5}{0.3s^2 + 2.3s + 1.5} \\ \frac{s+1}{0.3s^2 + 2.3s + 1.5} \end{bmatrix}$	$ \begin{bmatrix} 0.2s+5 \\ 0.3s^2+1.2s+5 \\ s \\ 0.3s^2+1.2s+5 \end{bmatrix} $		

For the second order system, the proportional $(K_{P2}(s))$, dynamic $(K_2(s))$, and PI $(K_{PI2}(s))$ controllers are used and defined in Table 2-3. The associated closed-loop system can be written in the form of (2.15), where the closed-loop transfer functions (H) are provided in Table 2-3.

Table 2-3: CL controllers and transfer functions of the second order plant

Closed-loop Controllers				
$K_{P2}(s) = 0.2$	$K_2(s) = \frac{s + 0.5}{s + 1}$	$K_{PI2}(s) = \frac{0.5s + 0.2}{s}$		
Corresponding Closed-Loop Transfer Functions H^T				
$\begin{bmatrix} \frac{0.2}{s^2 + s + 1.2} \\ \frac{1}{s^2 + s + 1.2} \end{bmatrix}$	$\begin{bmatrix} \frac{s+0.5}{s^3+2s^2+3s+1.5} \\ \frac{s+1}{s^3+2s^2+3s+1.5} \end{bmatrix}$	$\begin{bmatrix} \frac{0.5s + 0.2}{s^3 + s^2 + 1.5s + 0.2} \\ \frac{s}{s^3 + s^2 + 1.5s + 0.2} \end{bmatrix}$		

In order to conduct closed-loop system identification, all models were discretized with a sample period of 5ms. Discrete closed-loop models were obtained using PRBS q-Markov Cover. There are two approaches to obtain a continuous time plant model: a) solving the plant model in

discrete-time domain first, then converting it to a continuous-time model or b) converting the identified closed-loop model into a continuous model, and then solving for the plant model in continuous time. In this study, it is found that both approaches provide almost identical models. The rest of paper only presents the results associated with approach b).

2.4.2 PRBS q-Markov Cover System Identification

The closed-loop system models are identified in discrete time domain using PRBS-GUI (Graphic User Interface) [26] developed for PRBS q-Markov Cover. Identification parameters used for this study are listed in Table 2-4. When general setup is used, both $\hat{\mathbf{H}}_1$ and $\hat{\mathbf{H}}_2$ are identified. $\hat{\mathbf{H}}_1$ is identified in controller setup and $\hat{\mathbf{H}}_2$ is identified in compensator setup.

Table 2-4. PRBS q-Markov COVER system ID parameters

1 st order System Identification settings				
Controller	Open-loop Proportional		PI	First order
Sample rate (s)	0.005	0.005	0.005	0.005
PRBS order	8	8	9	10
Signal length (s)	25.6	25.6	51.2	102.4
# of Markov parameters	10	10	60	60
ID model order	1	1	2	2
2 nd order System Identification settings				
Controller	Open-loop	Proportional	PI	First order
Sample rate (s)	0.005	0.005	0.005	0.005
PRBS order	11	11	13	11
Signal length (s)	204.8	204.8	819.2	204.8
# of Markov parameters	60	60	60	60
ID model order	2	2	3	3

2.4.3 Closed-loop ID for the First-order System

For the first-order plant, identified closed-loop models of proportional, first-order dynamic, and PI controllers, and their corresponding open-loop models are listed in Table 2-5. Figure 2-4 shows the frequency responses of the calculated plant when proportional controller is used in closed-loop identification. The calculated plant models have almost identical frequency response to the original system in all three setups.

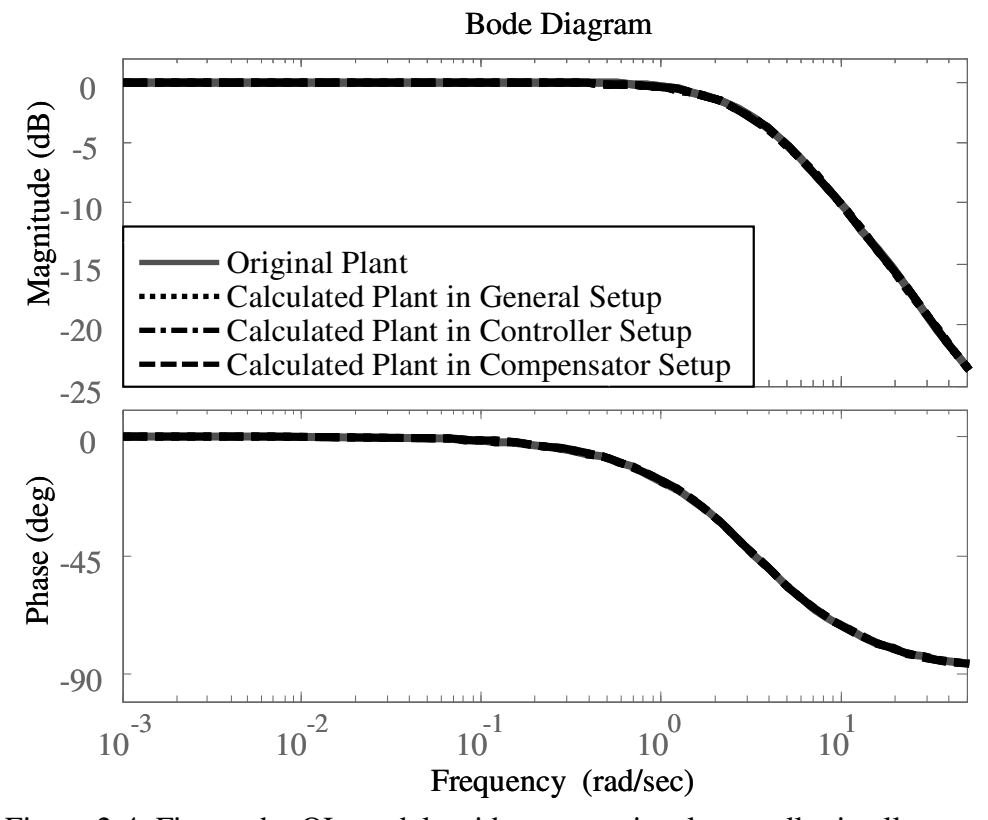


Figure 2-4. First-order OL models with a proportional controller in all setups

Similarly, it can be found from Figure 2-5 the open-loop models calculated from identified closed-loop models with the first-order dynamic controller also have very close frequency responses to these of original systems. There is only very small deviation of DC gain.

However, open-loop models obtained from identified closed-loop models with PI controllers have significant DC gain drop at low frequency (Figure 2-6). It also shows that compensator setup generates the worst calculated plant model.

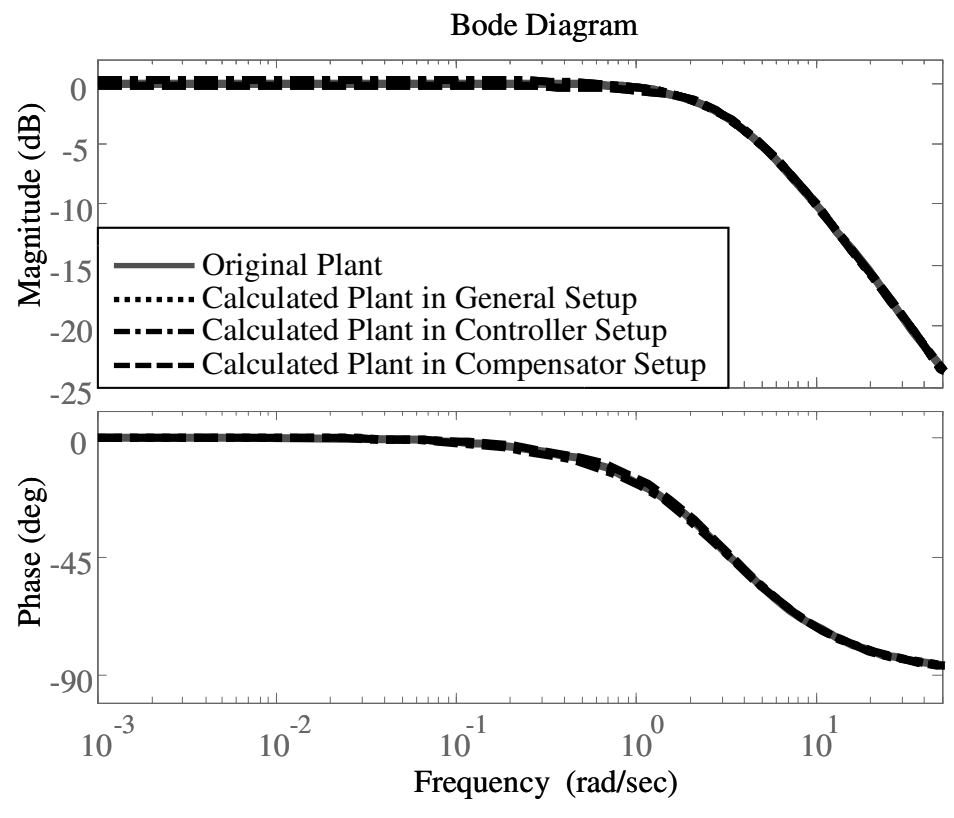


Figure 2-5. First-order OL models with a first order controller in all setups

Therefore, for the first order system, the closed-loop system identifications with a proportional controller are accurate for all three setups. For all setups with a first order controller, the calculated plant models are similar to the original plant. With the PI controller, plant models calculated from all setups have significant gain drop at low frequency. The compensator setup with the PI controller provides the worst calculated plant model.

Table 2-5. Identified closed/open-loop models for the first-order plant

Setup	Controller	Identified Closed-loop Model	Calculated Plant
	Proportional	$ \begin{bmatrix} -1.40 \times 10^{-5} & s + 0.665 \\ s + 4.02 \\ -6.97 \times 10^{-5} & s + 3.33 \\ s + 4.02 \end{bmatrix} $	$\frac{0.992}{0.298s + 1}$
General Setup	Dynamic	$ \left[\frac{2.26 \times 10^{-5} s^2 + 3.34 s + 1.99}{s^2 + 7.78 s + 5.65} \right. \\ \left. \frac{-1.03 \times 10^{-5} s^2 + 3.33 s + 3.67}{s^2 + 7.78 s + 5.65} \right] $	$\frac{-1.03s^2 + 3.33s + 3.67}{s^2 + 4.43s + 3.65}$
	PI	$ \left[\frac{-2.18 \times 10^{-5} s^2 + 0.657 s + 16.9}{s^2 + 4.03 s + 16.7} \\ \frac{0.000132 s^2 + 3.37 s + 0.0460}{s^2 + 4.03 s + 16.7} \right] $	$\frac{1.3 \times 10^{-4} s^2 + 3.34 s + 0.046}{s^2 + 3.37 s - 0.19}$
tup	Proportional	$\frac{-1.395 \times 10^{-5} \ s + 0.6651}{s + 4.019}$	$\frac{-2.1 \times 10^{-5} s + 0.99}{0.298 s + 1}$
Controller Setup	Dynamic	$\frac{2.263 \times 10^{-5} s^2 + 3.339 s + 1.775}{s^2 + 7.689 s + 5.185}$	$\frac{-1 \times 10^{-5} s^3 + 3.33 s^2 + 6.38 s + 3}{s^3 + 5.21 s^2 + 7.49 s + 3.14}$
Cor	PI	$\frac{-2.18 \times 10^{-5} s^2 + 0.662 s + 16.7}{s^2 + 3.95 s + 16.8}$	$\frac{-2.2 \times 10^{-5} s^3 + 0.662 s^2 + 16.7 s}{0.2 s^3 + 5.66 s^2 + 16.5 s + 0.4}$
tup	Proportional	$\frac{-6.97 \times 10^{-5} \ s + 3.33}{s + 4.02}$	$\frac{-2.1 \times 10^{-5} s + 0.992}{0.298 s + 1}$
Controller Setup	Dynamic	$\frac{-1.03 \times 10^{-5} s^2 + 3.33 s + 3.05}{s^2 + 7.54 s + 4.67}$	$\frac{-1 \times 10^{-5} s^3 + 3.33 s^2 + 6.38 s + 3}{s^3 + 5.21 s^2 + 7.49 s + 3.14}$
Con	PI	$\frac{0.000132s^2 + 3.38s - 0.188}{s^2 + 4.03s + 15.9}$	$\frac{1.3 \times 10^{-4} s^3 + 3.38 s^2 - 0.188 s}{s^3 + 3.38 s^2 - 0.433 s - 0.939}$

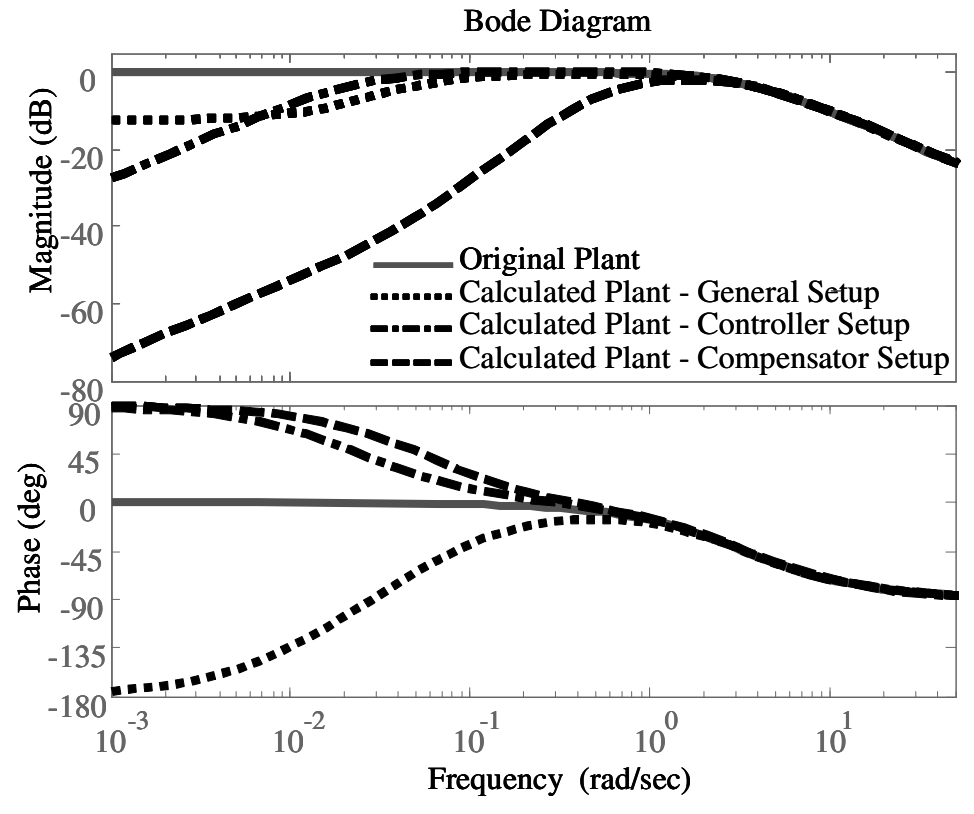


Figure 2-6. First-order OL models with a PI controller in three setups

2.4.4 Closed-loop ID for the Second-order System

For the second-order plant, identified closed-loop models and corresponding calculated plants are listed in Table 2-6. From Figure 2-7, the calculated plant models with proportional controllers have almost identical frequency response to the original system in all three identification setups. However there is certain phase shift beyond the PRBS frequency bandwidth (around 20Hz), indicating that high frequency PRBS excitation might needed.

Similarly, it can be found from Figure 2-8 the identified open-loop models with first order controllers have similar frequency response to the original system. Plant models obtained from closed-loop systems using controller and compensator setups have slight error in DC gain, and phase shifts near corner frequency.

Figure 2-9 shows the frequency response for the identified open-loop plants when the PI controller is used. The identified open-loop model using the general setup provides the closest

frequency response to the original one. Plant models obtained from the compensator setup have the worst accuracy.

Therefore, similar to the first-order system case, in the second-order system, the closed-loop system identifications for all three setups are accurate with proportional controller. Plant models obtained from closed-loop systems with the first order controller provide similar frequency response as the original plant. With the PI controller, only the general setup provides the accurate identified model.

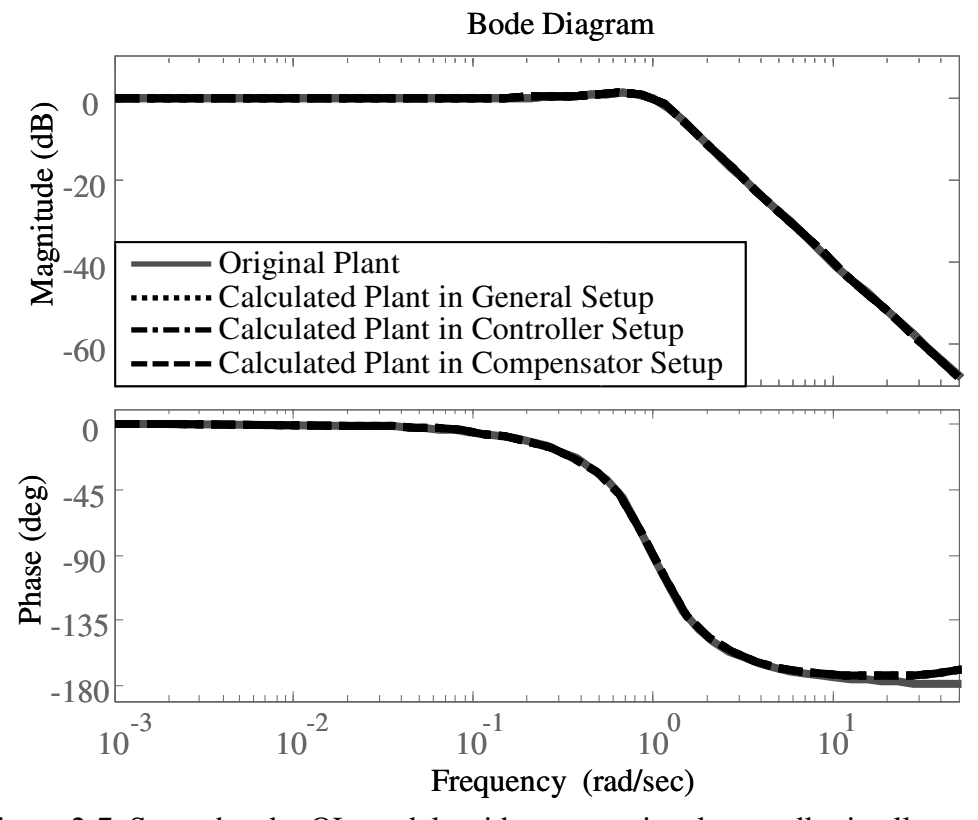


Figure 2-7. Second-order OL models with a proportional controller in all setups

Table 2-6. Identified closed/open-loop models for the second-order plant

Setup	Control	Identified Closed-loop Model	Calculated Plant
	Proportional	$ \begin{bmatrix} \frac{3.2 \times 10^{-6} s^2 + 0.00064s + 0.2}{s^2 + 1.0s + 1.2} \\ \frac{1.6 \times 10^{-5} s^2 + 0.0032s + 1}{s^2 + 1.0s + 1.2} \end{bmatrix} $	$\frac{1.6 \times 10^{-5} s^2 + 0.0032s + 1.0}{s^2 + 1.0s + 0.99}$
General Setup	Dynamic	$ \left[\frac{-3.7 \times 10^{-6} s^3 - 0.00074 s^2 + s + 0.35}{s^3 + 1.8 s^2 + 2.8 s + 1.2} -3.0 \times 10^{-6} s^3 - 0.00061 s^2 + s + 0.84}{s^3 + 1.8 s^2 + 2.8 s + 1.2} \right] $	$\frac{-3 \times 10^{-6} s^3 - 0.00061 s^2 + 0.99 s + 0.84}{s^3 + 1.8 s^2 + 1.99 + 0.84}$
	Id	$ \left[\frac{-1.3 \times 10^{-6} s^3 - 0.00026 s^2 + 0.5 s + 0.2}{s^3 + 1.0 s^2 + 1.5 s + 0.2} \right] \\ \frac{1.5 \times 10^{-6} s^3 + 0.0003 s^2 + s + 0.002}{s^3 + 1.0 s^2 + 1.5 s + 0.20} $	$\frac{1.5^{-6}s^3 - 0.0003s^2 + s + 0.0022}{s^3 + 1.0s^2 + 0.99s + 0.0017}$
dn	Ь	$\frac{3.2 \times 10^{-6} s^2 + 0.00064 s + 0.20}{s^2 + 1.0s + 1.2}$	$\frac{1.6 \times 10^{-5} s^2 + 0.0032 s + 1.0}{s^2 + 1.0 s + 0.99}$
Controller Setup	Dynamic	$\frac{-3.7 \times 10^{-6} s^3 - 0.00075 s^2 + s + 0.2}{s^3 + 1.7 s^2 + 2.6 s + 0.78}$	$\frac{-4 \times 10^{-6} s^4 - 0.001 s^3 + s^2 + 1.2 s + 0.2}{s^4 + 2.3 s^3 + 2.5 s^2 + 1.4 s + 0.28}$
Cc	PI	$\frac{-1.3 \times 10^{-6} s^3 - 0.00025 s^2 + 0.5 s + 0.2}{s^3 + 1.0 s^2 + 1.5 s + 0.20}$	$\frac{-1.3 \times 10^{-6} s^4 - 0.0003 s^3 + 0.5 s^2 + 0.2 s}{0.5 s^4 + 0.7 s^3 + 0.7 s^2 + 0.2 s + 0.00034}$
tup	d	$\frac{1.62 \times 10^{-5} s^2 + 0.0032 s + 1}{s^2 + 1.0 s + 1.2}$	$\frac{1.6 \times 10^{-5} s^2 + 0.0032 s + 1}{s^2 + 1.0 s + 0.99}$
Compensator Setup	Dynamic	$\frac{-3.0 \times 10^{-6} s^3 - 0.00062 s^2 + s + 0.52}{s^3 + 1.5 s^2 + 2.5 s + 0.68}$	$\frac{-3 \times 10^{-6} s^4 - 0.0006 s^3 + s^2 + 1.5 s + 0.5}{s^4 + 2.5 s^3 + 3 s^2 + 2.1 s + 0.42}$
Coı	Id	$\frac{1.5 \times 10^{-6} s^3 + 0.0003 s^2 + s + 0.0023}{s^3 + 1.0s^2 + 1.5s + 0.20}$	$\frac{-1.3 \times 10^{-6} s^4 - 0.0003 s^3 + s^2 + 0.002 s}{s^4 + s^3 + 0.99 s^2 + 0.0006 s - 0.00045}$

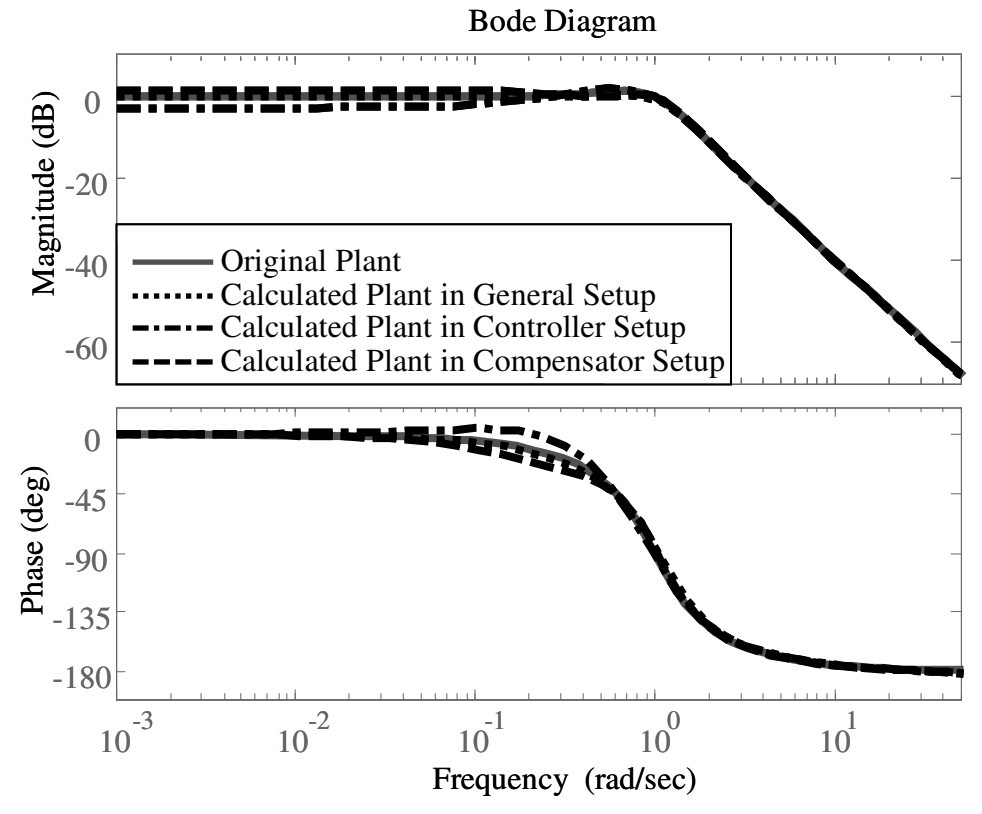


Figure 2-8. Second-order OL models with a first-order controller in all setups

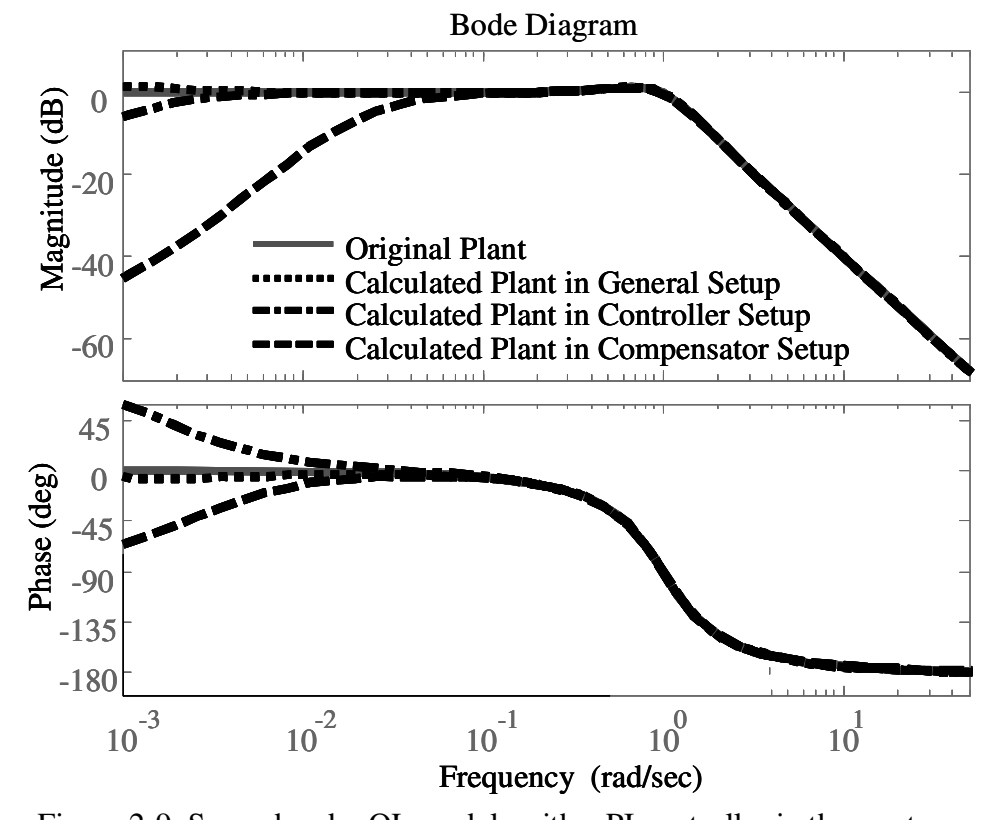


Figure 2-9. Second-order OL models with a PI controller in three setups

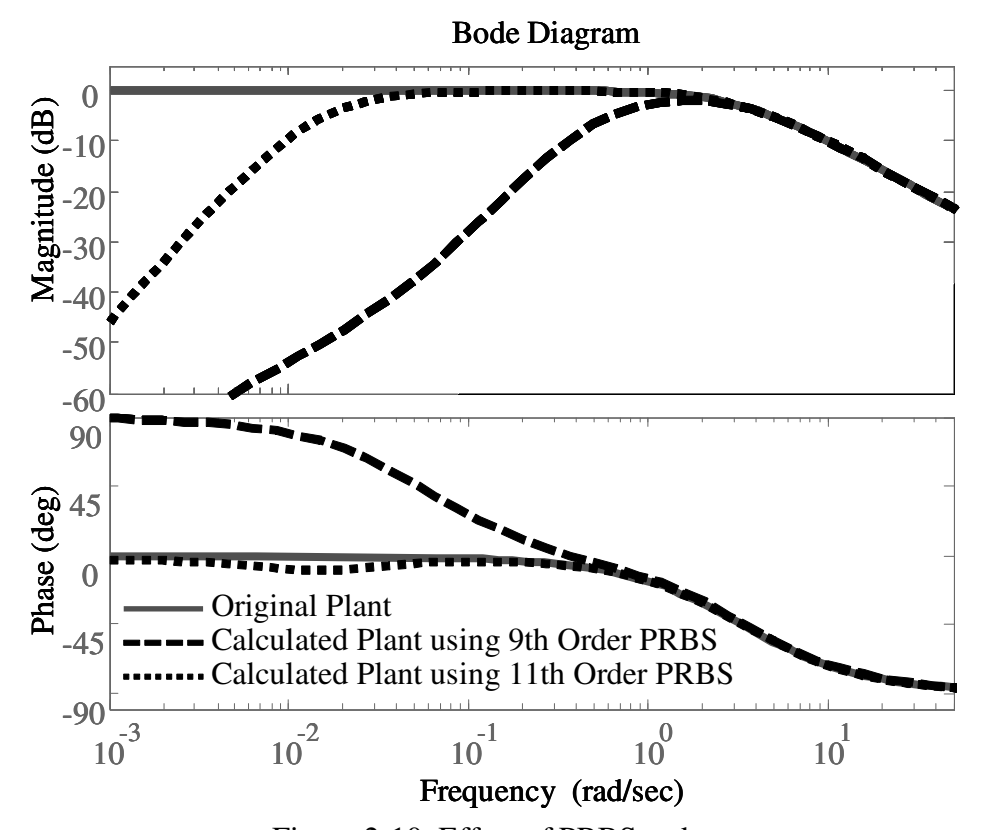
2.4.5 Effect of the PRBS Signal Order

The following example is used to investigate the effect of PRBS order associated with identification error at low frequency. Increasing PRBS order decreases identification excitation signal bandwidth at low frequency. Using the first-order system in the compensator setup with a PI controller, an eleventh-order PRBS signal was used with other parameters defined in 2.4, the identified closed-loop system model is

$$\hat{H}_1 = \frac{4.071 \times 10^{-6} \,s^2 + 3.335 s + 0.0001296}{s^2 + 4.003 s + 16.66} \tag{2.16}$$

and the corresponding open-loop model is

$$G_{cal} = \frac{4.07 \times 10^{-6} s^3 + 3.335 s^2 + 0.00013 s}{s^3 + 3.336 s^2 - 0.015 s - 0.000648}.$$
 (2.17)



As expected (Figure 2-10), the low frequency identification error decreases as PRBS order increases.

2.5 Conclusion

A low frequency system identification error was discovered when an integral controller is used for PRBS q-Markov Cover closed-loop system identification using an indirect approach. Significant low frequency gain of the identified open-loop model was observed when the dynamic integral controller was used. Increasing the order of the PRBS signal decreases the error at low frequencies. The general setup of the closed-loop system identification setup provides fairly accurate identified open-loop models even with the dynamic integral controller. Using the proportional controller in the closed-loop system identification leads to the most accurate plant model. If feasible, it is recommended not to use a dynamic integral controller in the closed-loop system identification when PRBS is used as excitations. In this paper, the framework used for VVT system closed-loop identification is the controller setup with a proportional controller.

Chapter 3 Hydraulic Variable Valve Timing System Identification and Controller Design

3.1 Introduction

Continuously variable valve timing (VVT) system was developed in the early nineties [1]. The benefits of using VVT for internal combustion engines include improved fuel economy with reduced emissions at low engine speed, as well as increased power and torque at high engine speed. Vane-type VVT system [2] is a hydraulic mechanical actuator controlled by a solenoid. Electric motor driven cam phase actuators have become available recently due to their fast responses [42]. This chapter studies the modeling and control of hydraulic VVT systems.

There are two approaches to obtain a control oriented VVT system model for model-based control development and validation: physics based system modeling [18] and system identification using the system input and output data. In this paper, the closed-loop system identification approached is employed to obtain the VVT subsystem model of an internal combustion engine. System identification using closed-loop experimental input and output data was developed in the seventies [19] and has been widely used in engineering practices ([20], [21], and [22]). Closed-loop system identification can be used to obtain the open-loop system models, especially when the open-loop plant cannot be excited at the operational conditions ideal for system identification. For instance, closed-loop system identification is typically applied to identify an unstable open-loop plant. In this paper, the closed-loop identification method was selected due to many factors. The main reason is that the system open-loop gain of the VVT actuator is fairly high and the cam shaft has a torque load disturbance, which makes it almost impossible to maintain the cam phase at a desired operational condition. The other factor is that the VVT system dynamic is also a function of engine speed, load, oil pressure, and temperature,

which make open-loop system identification difficult. Therefore, open-loop system identification at a desired cam phase is not feasible and the closed-loop identification was selected.

The first portion of this paper describes the process of obtaining linearized system models of the VVT actuator subsystem at various operational conditions using the indirect closed-loop system identification approach discussed in [21]. The *q*-Markov COVariance Equivalent Realization (*q*-Markov Cover) system identification method ([23], [24], and [25]) using PRBS (Pseudo-Random Binary Signals) was used to obtain the closed-loop system models. The *q*-Markov Cover theory was originally developed for model reduction. It guarantees that the reduced order system model preserves the first *q* Markov parameters of the original system. The realization of all *q*-Markov Covers using input and output data of a discrete time system is capable of system identification. Q-Markov Cover for system identification uses pulse, white noise, or PRBS as input excitations. It can be used to obtain the linearized model representing the same input/output sequence for nonlinear systems [25]. It was also been extended to identify multi-rate discrete-time systems when input and output sampling rates are different [26].

For the proposed study, the multi-rate system identification is required due to event based cam phase sampling (function of engine speed) and time based control sampling. For our test bench setup, the cam position was sampled four times over an engine cycle. For instance, when the engine is operated at 1500 rpm, the cam position sample period is 20ms, and the control input is updated at a fixed sample period of 5ms. For this study, multi-rate PRBS *q*-Markov Cover was used for closed-loop system identification on the VVT test bench. System models at different engine operational conditions were identified using closed-loop multi-rate identification.

The second portion of this chapter presents the control design and validation. The OCC (Output Covariance Constraint) control design approach ([33], [34], and [35]) and LPV (Linear

Parameter Varying) control were designed and validated on test bench and engine dynamometer (dyno).

The OCC control minimizes system control effort subject to multiple performance constraints on output covariance matrices. An iterative controller design algorithm [35] with guaranteed convergence can be used to find an OCC optimal controller. Note that an OCC controller is a H_2 controller with a special output weighting matrix selected by the OCC control design algorithm. The OCC control scheme was applied to many aerospace control problems due to its minimal control effort ([33], [34], and [35]). In this paper, a nominal model was selected from the family of the identified VVT models for the OCC control design. Multiple OCC controllers were designed based upon closed-loop identified models, and their performances were compared against these of the well tuned baseline PI controller. In order to eliminate steady-state error, system control input was increased to add an additional integral input to system plant used for the OCC control design. Comparing with the PI control, the OCC controllers were able to achieve the similar system settling time to PI ones with significantly less overshoot and control effort.

The system model identification and controller design approach was tested and validated on a VVT test bench. The control design model is obtained from the closed-loop system identification, and the designed controller was evaluated in an actual VVT test bench. The same approach was then used on an engine dyno with dual VVT system. Both test results show that the integrated system identification and control design provides satisfactory controllers.

A modern internal combustion engine operates at a wide range of temperatures, as well as different loads and speeds. Due to the physical dynamics of the VVT system, its performance is affected by operating temperature, engine oil pressure, and engine rpm. In order to optimize the

performance at all the operating conditions, a family of VVT system models was identified at different engine oil pressure and engine speed. A linear parameter varying (LPV) system ([27] to [32]) was constructed based on the models. A gain-scheduling controller ([36] and [37]) was designed based on the LPV system and was tested on the test bench.

Closed-loop identification and OCC design of a hydraulic VVT system on the test bench introduced in the dissertation can also be found in [43] and [44]. The detailed work of LPV modeling and gain-scheduling design can be found in [45].

The chapter is organized as the following. Section 3.2 provides framework and formulation of closed-loop system identification for the VVT actuator system. Section 3.3 presents the OCC control problem and associated design framework. HIL simulation is conducted in Section 3.4. Section 3.5 describes the test bench setup. Section 3.6 introduces the closed-loop system identification and the OCC controller design results obtained from the test bench, along with the discussions of the experiment results. LPV controller design and validation is in Section 3.7. Section 3.8 introduces engine dyno setup and dyno test results are shown in Section 3.9. Conclusions are provided in Section 3.10.

3.2 System Identification Framework

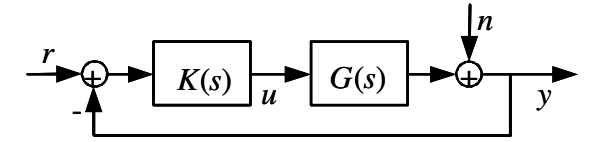


Figure 3-1. Closed-loop identification framework

Consider a general form of linear time-invariant closed-loop system in Figure 3-1, where r is the reference signal, u is the input, and y is the output. As discussed in the Introduction section, there are many approaches for the closed-loop identification, which are categorized as direct, indirect, and joint input-output approaches. In this paper, we utilize the knowledge of the

controller to calculate the open-loop plant model from identified closed-loop plant model, which is called the indirect approach. To ensure the quality of the identified plant, the closed-loop controller in this paper is selected to be proportional ([38], and [46]).

The input and output relationship of the generalized closed-loop system, shown in Figure 3-1, can be expressed below

$$\mathbf{v} = \mathbf{H} \cdot \mathbf{r} = \mathbf{G} \mathbf{K} (\mathbf{I} + \mathbf{G} \mathbf{K})^{-1} \mathbf{r}$$
 (3.1)

Let $\hat{\mathbf{H}}$ be identified closed-loop transfer functions from r to y. The open-loop system model \mathbf{G}_{ID} can be calculated using identified $\hat{\mathbf{H}}$, assuming that $(\mathbf{I} - \hat{\mathbf{H}})^{-1}$ is invertible. The closed-loop controller transfer function is used to solve for the open-loop system models. We have

$$\mathbf{G}_{ID} = \hat{\mathbf{H}} (\mathbf{I} - \hat{\mathbf{H}})^{-1} \mathbf{K}^{-1}$$
 (3.2)

PRBS signal is used as an input signal for identifying the closed-loop system model. The most commonly used PRBSs are based on maximum length sequences (called *m*-sequences) [39] for which the length of the PRBS signals is $m = 2^n - 1$, where *n* is an integer (order of PRBS). Let z^{-1} represent a delay operator, and define $\hat{p}(z^{-1})$ and $p(z^{-1})$ to be polynomials

$$p(z^{-1}) = a_n z^{-n+1} \oplus \dots \oplus a_2 z^{-1} \oplus a_1 = \hat{p}(z^{-1}) z^{-1} \oplus 1$$
 (3.3)

where a_i is either 1 or 0, and \oplus obeys binary addition, i.e.

$$1 \oplus 1 = 0 = 0 \oplus 0 \& 0 \oplus 1 = 1 = 1 \oplus 0 \tag{3.4}$$

and the non-zero coefficients a_i of the polynomial are defined in the following Table 2-1 and also in [39].

Then the PRBS can be generated by the following formula:

$$\hat{u}(k+1) = \hat{p}(z^{-1})\hat{u}(k), \quad k = 0, 1, 2, \dots$$
 (3.5)

where $\hat{u}(0) = 1$ and $\hat{u}(-1) = \hat{u}(-2) = \cdots = \hat{u}(-n) = 0$. Defined the following sequence:

$$s(k) = \begin{cases} a; & \text{If } k \text{ is even;} \\ -a; & \text{If } k \text{ is odd.} \end{cases}$$
 (3.6)

Then, the signal

$$u(k) = s(k) \otimes [-a + 2 \ a \ \hat{u} \ (k)] \tag{3.7}$$

is called the *inverse* PRBS, where \otimes obeys

$$a \otimes a = -a = -a \otimes -a \quad \& \quad a \otimes -a = a = -a \otimes a \tag{3.8}$$

It is clear after some analysis that u has a period 2m and u(k) = -u(k+m). The mean of the inverse PRBS is

$$m_u = E_{2m}u(k) \equiv \frac{1}{2m} \sum_{k=0}^{2m-1} u(k) = 0$$
 (3.9)

and the autocorrelation ($R_{uu}(\tau) = E_{2m}u(k+\tau)u(k)$) of u is

$$R_{uu}(\tau) = \frac{1}{2m} \sum_{k=0}^{2m-1} u(k+\tau)u(k) = \begin{cases} a^2, & \tau = 0; \\ -a^2, & \tau = m; \\ -a^2/m, & \tau \text{ even}; \\ a^2/m, & \tau \text{ odd.} \end{cases}$$
(3.10)

Note that the first and second-order information of the inverse PRBS signal is very close to these of white noise for a large enough m. The inverse PRBS is used in the q-Markov Cover identification algorithm. For convenience, in the rest of this paper, the term "PRBS" is used to represent the inverse PRBS.

Consider an unknown (presumed nonlinear) system

$$\mathbf{x}(k+1) = f(\mathbf{x}(k), \mathbf{w}(k))$$

$$\mathbf{y}(k) = g(\mathbf{x}(k), \mathbf{w}(k))$$
(3.11)

subjected to an input sequence $\{w(0), w(1), w(2), ...\}$ generating the output sequence $\{y(0), y(1), y(2), ...\}$. The unknown system is q-identifiable, if there exists a linear model of the form

$$\mathbf{x}(k+1) = \mathbf{A}\mathbf{x}(k) + \mathbf{D}\mathbf{w}(k)$$

$$\mathbf{y}(k) = \mathbf{C}\mathbf{x}(k) + \mathbf{H}\mathbf{w}(k)$$
(3.12)

that can reproduced the same output sequence $\{y(0), y(1), y(2), ..., y(q-1)\}$, subject to the same input sequence $\{w(0), w(1), w(2), ..., w(q-1)\}$. In case that the system is not *q*-identifiable, it is possible for *q*-Markov cover to construct the least square fit using a linear model for the input-output sequence ([47], and [48]).

In this paper, system models were identified in discrete time domain using the PRBS GUI (Graphic User Interface) [34] developed for multi-rate PRBS *q*-Markov Cover. The advantage of using the PRBS GUI is that the number of Markov parameters and the order of the identified system model can be easily adjusted based upon the calculated Markov singular values from the input-output data.

3.3 Output Covariance Control (OCC)

Consider the following linear time-invariant system:

$$\mathbf{x}_{\mathbf{p}}(k+1) = \mathbf{A}_{\mathbf{p}}\mathbf{x}_{\mathbf{p}}(k) + \mathbf{B}_{\mathbf{p}}\mathbf{u}(k) + \mathbf{D}_{\mathbf{p}}\mathbf{w}_{\mathbf{p}}(k)$$

$$\mathbf{y}_{\mathbf{p}}(k) = \mathbf{C}_{\mathbf{p}}\mathbf{x}_{\mathbf{p}}(k)$$

$$\mathbf{z}(k) = \mathbf{M}_{\mathbf{p}}\mathbf{x}_{\mathbf{p}}(k) + \mathbf{v}(k)$$
(3.13)

where \mathbf{x}_p is the state, \mathbf{u} is the control, \mathbf{w}_p represents process noise, and \mathbf{v} is the measurement noise. Vector \mathbf{y}_p contains all variables whose dynamic responses are of interest. Vector \mathbf{z} represents noisy measurements. Suppose that a strictly proper output feedback stabilizing control law, shown below, is used for plant (13)

$$\mathbf{x_c}(k) = \mathbf{A_c}\mathbf{x_c}(k) + \mathbf{Fz}(k)$$

$$\mathbf{u}(k) = \mathbf{Gx_c}(k)$$
(3.14)

then the resulting closed-loop system is

$$\mathbf{x}(k+1) = \mathbf{A}\mathbf{x}(k) + \mathbf{D}\mathbf{w}(k)$$

$$\mathbf{y}(k) = \begin{bmatrix} \mathbf{y}_{\mathbf{p}}(k) \\ \mathbf{u}(k) \end{bmatrix} = \begin{bmatrix} \mathbf{C}_{\mathbf{y}} \\ \mathbf{C}_{\mathbf{u}} \end{bmatrix} \mathbf{x}(k) = \mathbf{C}\mathbf{x}(k)$$
(3.15)

where $\mathbf{x} = [\mathbf{x}_{\mathbf{p}}^{\mathbf{T}} \quad \mathbf{x}_{\mathbf{c}}^{\mathbf{T}}]^{\mathbf{T}}$ and $\mathbf{w} = [\mathbf{w}_{\mathbf{p}}^{\mathbf{T}} \quad \mathbf{v}^{\mathbf{T}}]^{\mathbf{T}}$. Formulas for \mathbf{A} , \mathbf{C} , and \mathbf{D} are easy to obtain from (3.13) and (3.14).

Consider the closed-loop system (3.15). Let W_p and V denote positive definite symmetric matrices with dimensions equal to the process noise w_p and noisy measurement vector \mathbf{z} , respectively. Define $\mathbf{W} = block\ diag\left[\mathbf{W}_p\ V\right]$ and let \mathbf{X} denote the closed-loop weighted controllability Gramian from the input $\mathbf{W}^{-\frac{1}{2}}\mathbf{w}$. Since \mathbf{A} is stable, \mathbf{X} is given by

$$\mathbf{X} = \mathbf{A}\mathbf{X}\mathbf{A}^{\mathbf{T}} + \mathbf{D}\mathbf{W}\mathbf{D}^{\mathbf{T}} \tag{3.16}$$

In this paper we are interested in finding controllers of the form (14) that minimize the (weighted) control energy $trace(\mathbf{RC_uXC_u^T})$ with $\mathbf{R} > 0$ and satisfy the constraints

$$\mathbf{Y} = \mathbf{C}\mathbf{X}\mathbf{C}^{\mathbf{T}} \le \overline{\mathbf{Y}} \tag{3.17}$$

where $\overline{Y} \ge 0$ are given and X solves (16). This problem, which we call the output covariance constraint (OCC) problem, is defined as: finding a full-order dynamic output feedback controller for system (3.13) to minimize the OCC cost

$$J_{occ} = trace(\mathbf{RC_uXC_u^T}), \qquad \mathbf{R} > 0$$
 (3.18)

subject to (3.16) and (3.17).

The OCC problem may be given several interesting interpretations. For instance, assume first that $\mathbf{w_p}$ and \mathbf{v} are uncorrelated zero-mean white noises with intensity matrices $\mathbf{W_p} > 0$ and $\mathbf{V} > 0$. Let E be an expectation operator, and

$$E[\mathbf{w}_{\mathbf{p}}(k)] = 0; E[\mathbf{w}_{\mathbf{p}}(k)\mathbf{w}_{\mathbf{p}}^{\mathbf{T}}(k-n)] = \mathbf{W}_{\mathbf{p}}\delta(n)$$

$$E[\mathbf{v}(k)] = 0; E[\mathbf{v}(k)\mathbf{v}^{\mathbf{T}}(k-n)] = \mathbf{V}\delta(n)$$
(3.19)

Defining $E_{\infty}[\cdot] := \lim_{k \to \infty} E[\cdot]$ and $\mathbf{W} = block \ diag[\mathbf{W_p} \ \mathbf{V}]$, it is easy to see that the OCC is the problem of minimizing $E_{\infty}\mathbf{u^T}\mathbf{Ru}$ subject to the OCC constraint $\mathbf{Y} := E_{\infty}\mathbf{y}(k)\mathbf{y^T}(k) \le \overline{\mathbf{Y}}$. As it is well known, the constraint may be interpreted as constraint on the variance of the performance variables or lower bounds on the residence time (in a given ball around the origin of the output space) of the performance variables [49].

The OCC problem may also be interpreted from a deterministic point of view. To see this, define the discrete time domain ℓ_∞ and ℓ_2 norms

$$\|\mathbf{y}\|_{\infty}^{2} := \sup_{k \ge 0} \mathbf{y}^{\mathbf{T}}(k)\mathbf{y}(k)$$

$$\|\mathbf{w}\|_{2}^{2} := \sum_{k=0}^{\infty} \mathbf{w}^{\mathbf{T}}(k)\mathbf{w}(k)$$
(3.20)

and define the (weighted) ℓ_2 disturbance set

$$\mathcal{W} := \left\{ \mathbf{w} : \mathbf{R} \to \mathbf{R}^{n_w} \text{ and } \left\| \mathbf{W}^{-1/2} \mathbf{w} \right\|_2^2 \le 1 \right\}$$
 (3.21)

where W>0 is a real symmetric matrix. Then, for any $w\in\mathcal{U}$, we have (from [50], and [51])

$$\|\mathbf{y}\|_{\infty}^{2} \le \overline{\sigma}[\mathbf{Y}], \text{ and } \|\mathbf{u}_{i}\|_{\infty}^{2} \le [\mathbf{C}_{\mathbf{u}}\mathbf{X}\mathbf{C}_{\mathbf{u}}^{\mathbf{T}}]_{ii}, i = 1, 2, \dots n_{u}$$
 (3.22)

where n_u is the dimension of \mathbf{u} ; $\overline{\sigma}[\cdot]$ denotes the maximum singular value; and $[\cdot]_{ii}$ is the *i*-th diagonal entry. Moreover, references [50] and [51] show that the bounds in (22) are the least upper bounds that hold for any signal $\mathbf{w} \in \mathcal{W}$.

Thus, if we define $\overline{\mathbf{Y}} := I\epsilon^2$ in (17) and $\mathbf{R} = diag\left[r_1, r_2, ..., r_{n_u}\right] > 0$ in (18), the OCC problem is minimizing the (weighted) sum of worst-case peak values on the control signals given by

$$J_{occ} = \sum_{i=1}^{n_u} r_i \left\{ \sup_{\mathbf{w} \in \mathcal{V}} \left\| \mathbf{u}_i \right\|_{\infty}^2 \right\}$$
 (3.23)

subject to constraints on the worst-case peak values of the performance variables of the form

$$\sup_{\mathbf{w} \in \mathcal{U}} \|\mathbf{y}\|_{\infty}^{2} \le \epsilon^{2} \tag{3.24}$$

This interpretation is important in applications where hard constraints on responses or actuator signals cannot be ignored, such as space telescope pointing and machine tool control [34].

Detailed proof can be found in [35]. The controller system matrices $\mathbf{A_c}$, \mathbf{F} , and \mathbf{G} can be calculated using an iteration algorithm introduced in [33] and [35].

3.4 System Identification Using an HIL Simulator

Closed-loop system identification was conducted using an HIL simulator. A plant model, described in [52], is loaded into a dSPACE based HIL simulator.

$$G(s) = \frac{-0.01348(s - 2000)}{s + 26.96}$$
 (3.25)

The pulse signal of the cam position sensor is generated in the HIL simulator. In every engine cycle, the HIL simulator generates four evenly positioned pulses, which are sampled by

an Opal-RT real-time controller. The real-time controller processes the cam position signal and calculates the cam phase position. Figure 3-2 shows the architecture of the closed-loop system identification.

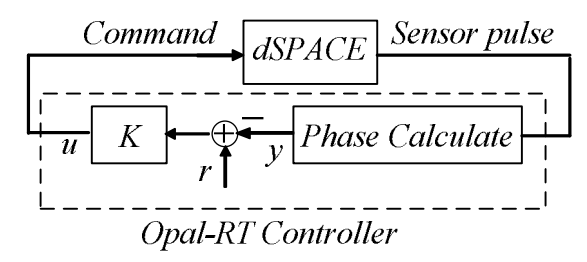


Figure 3-2. Closed-loop identification framework on an HIL simulator

After the error between the calculated cam phase and the reference PRBS signal is calculated, the cam actuator command is generated and sampled by the dSPACE HIL simulator. Reference PRBS signal r and the measured cam phase signal y are recorded for system identification. In this study, the plant model refers to the transfer function between command signal u and calculated phase y.

In this study, a proportional controller K = 0.5 is used. Note that at different engine speeds, the ratio between input and output sample rates is different. Recorded system response data were processed using MATLAB PRBS-GUI. The number of Markov parameter was selected based on the quality of the identified model. The model order was selected based on the dominant dynamics of the recorded data. The open-loop plant models shown in (3.26) are obtained from identified closed loop transfer functions (3.2)

$$G_{1000rpm}(s) = \frac{-0.0001s^2 - 6.32s + 768.6}{1.0001s^2 + 32.98s + 1060.7}$$

$$G_{1500rpm}(s) = \frac{0.00252s^2 - 6.3s + 1339}{0.998s^2 + 52.74s + 1664.5}$$

$$G_{2000rpm}(s) = \frac{0.0006s^2 - 9.99s + 1911.6}{0.999s^2 + 78.86s + 2140.2}$$
(3.26)

Table 3-1. Closed-loop PRBS q-Markov COVER system ID results

Engine Speed (rpm)			1500	2000
DC Gain Error (dB)			-1.9	-1.0
¹ / ₄ Sample Rate limit (Hz)			12.5	16.67
Plant Resp. Error at Freq. above	Gain (dB)	-2.4	-2.9	-2.8
	Phase (deg)	-92.8	-84.7	-87.5

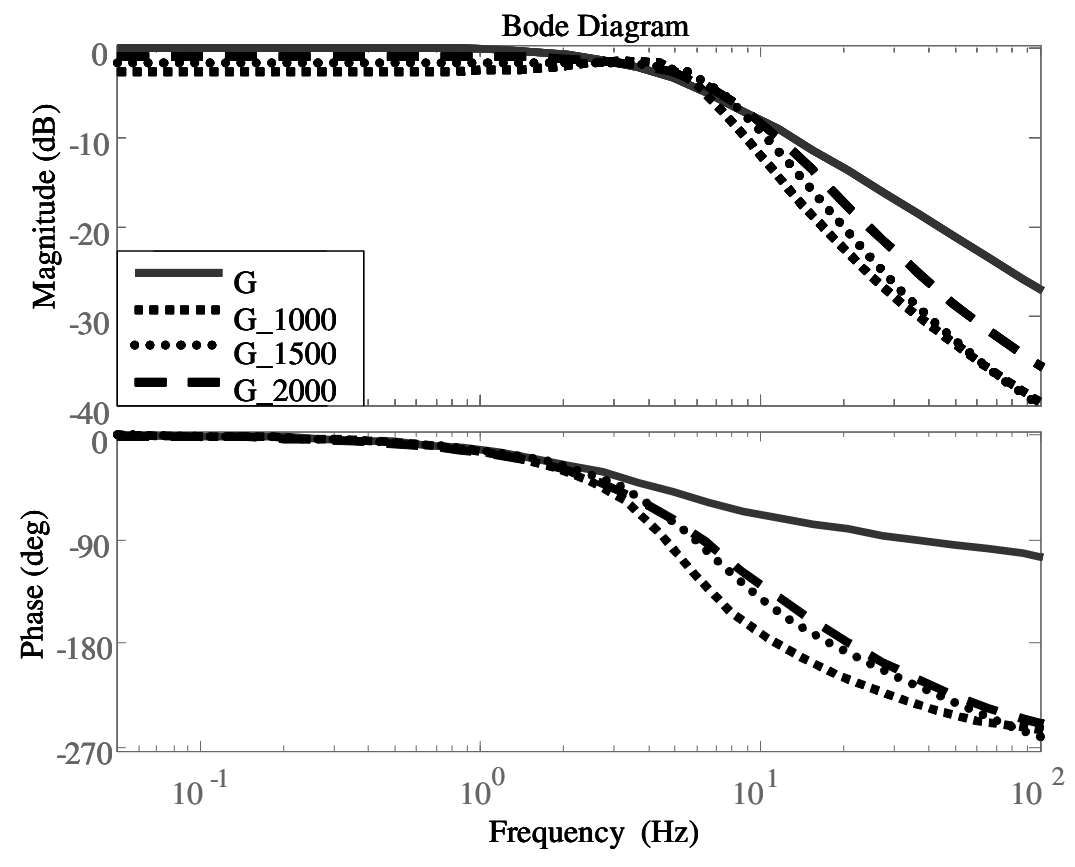


Figure 3-3. Identified model frequency responses of the HIL simulator

From Bode diagrams, all identified models are accurate at low frequency, and the accuracy improves as the engine speed increases (See Figure 3-3 and Table 3-1). Since the HIL sends feedback signals at a rate of 4 cycles per engine cycle, the actual identified systems also include a pure phase delay. Figure 3-4 shows that the identified phase is very close to the model (3.25) with a time delay associated with the engine speed. This figure proved that the closed-loop

identification method retrieved the whole system dynamics very well and can be used for the future bench tests.

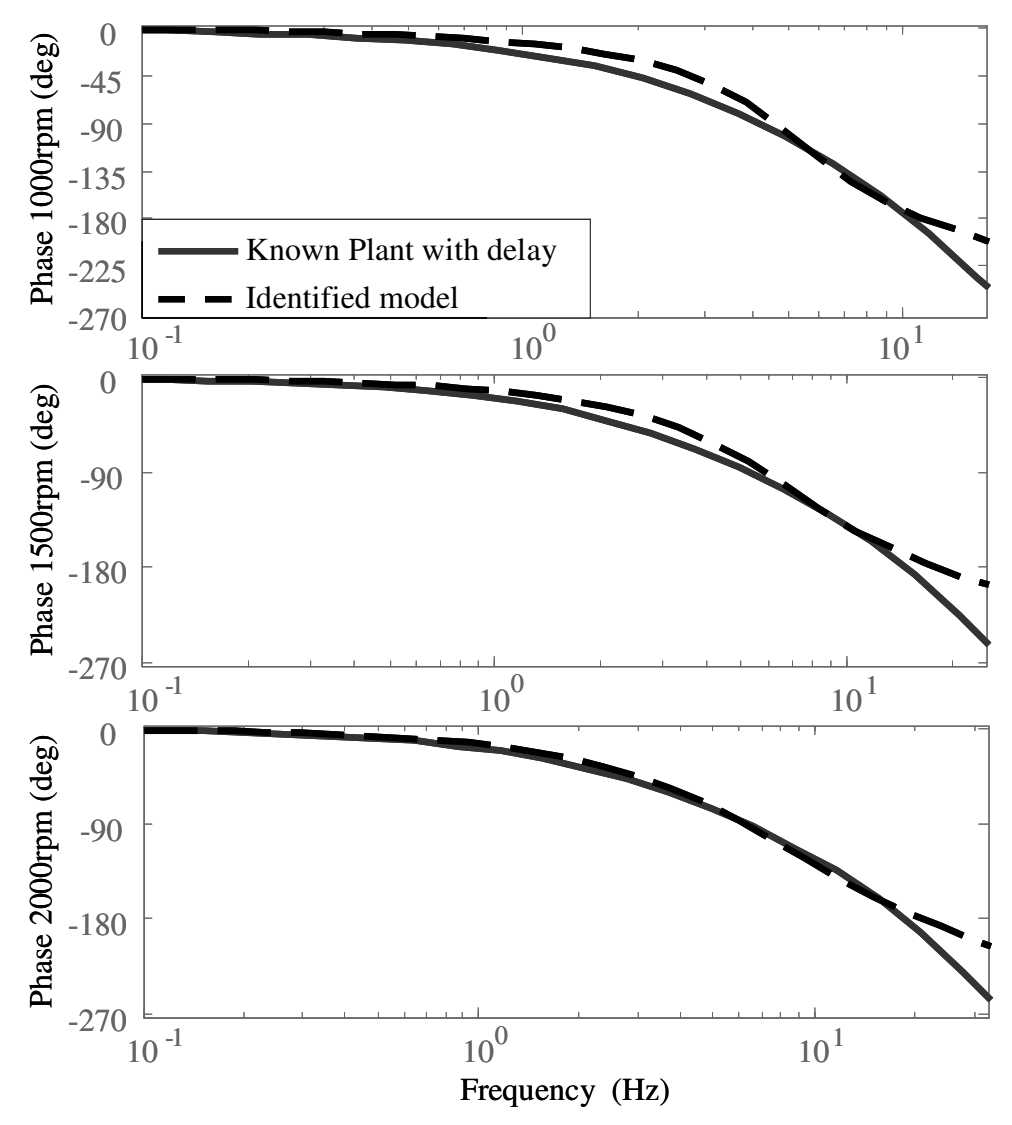


Figure 3-4. Identified phase delay at different engine speeds

Figure 3-5 compares the responses of original plant and closed-loop identified plants at 2000 rpm using PRBS excitation. The figure shows one fourth of eleventh-order PRBS length (about 5 seconds of the responses). From the plot, one can observe that the responses between the original and identified models are very close.

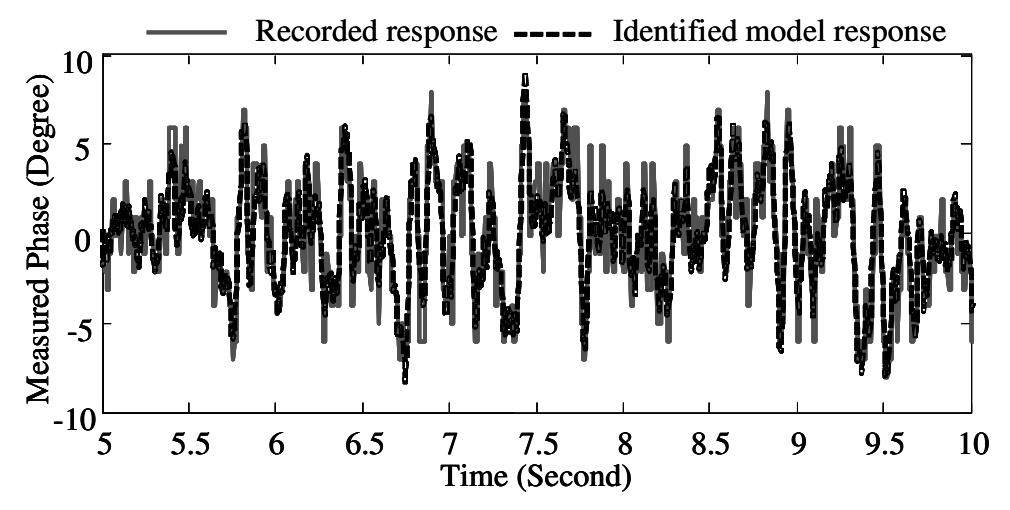


Figure 3-5. Identified model and physical system responses with PRBS input

3.5 VVT System Bench Tests Setup

3.5.1 System Configuration

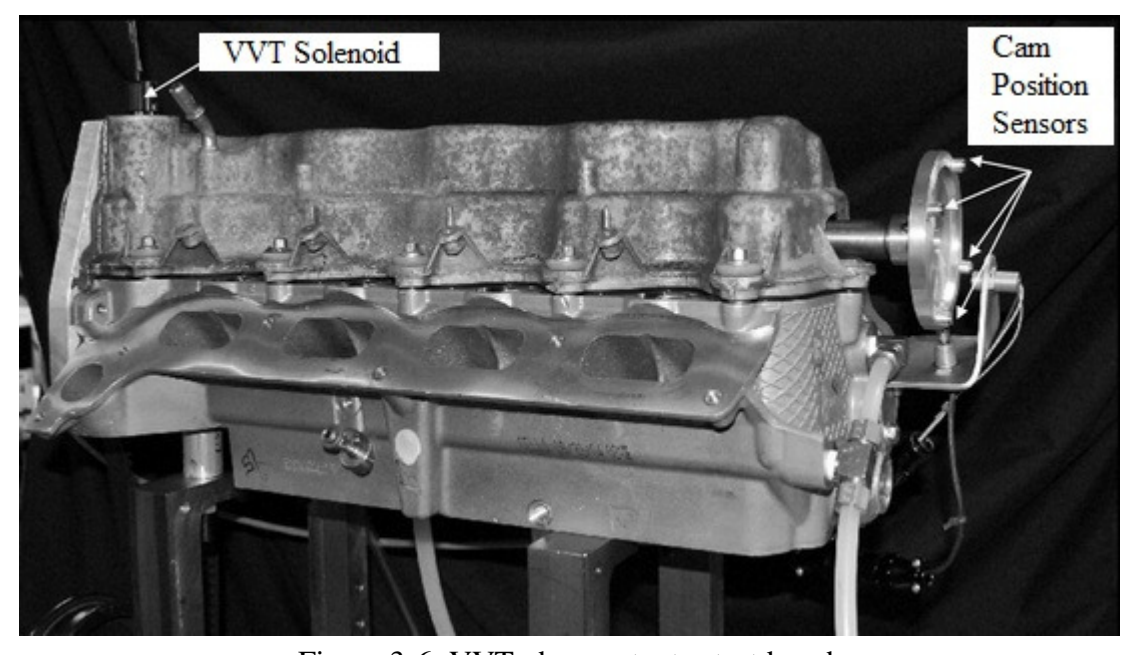


Figure 3-6. VVT phase actuator test bench

Closed-loop system identification and control design tests were conducted on the VVT test bench (Figure 3-6 and Figure 3-7). A Ford 5.4L V8 engine head was modified and mounted on the test bench. The cylinder head has a single cam shaft with a VVT actuator for one exhaust

and two intake valves. These valves introduce a cyclic torque disturbance to the cam shaft. The cam shaft is driven by an electric motor through a timing belt.

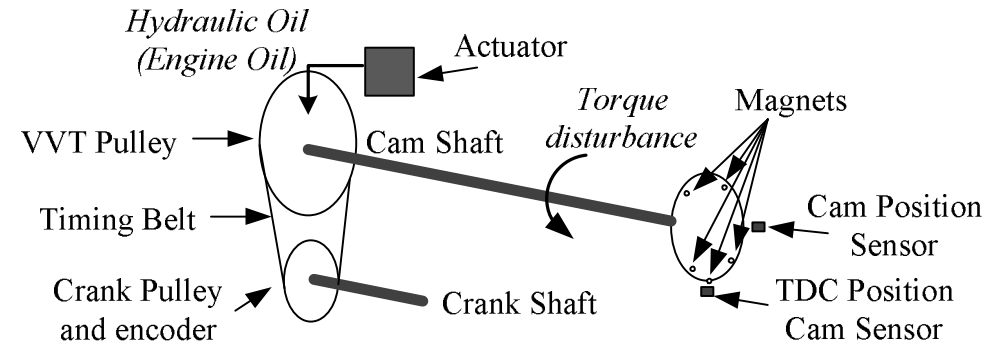


Figure 3-7. VVT phase actuator test bench diagram

An encoder is installed on the motor shaft (simulated the crank shaft), which generates a crank angle signal with one degree resolution, along with a so-called gate signal (one pulse per revolution). A plate with magnets attached was mounted at the other side of the extended cam shaft. These magnets pass two hall-effect cam position sensors when the cam shaft rotates, where one cam sensor was used to determine engine combustion TDC position (combustion phase), along with the encoder signals and the other is used to determine the cam phase. This cam position signal updates four times per cycle.

The cam phase actuator system consists of a solenoid driver circuit, a solenoid actuator, and hydraulic cam actuator. The solenoid driver is controlled by a PWM signal, where its duty cycle is proportional to the DC voltage command. An electric oil pump was used to supply pressurized oil for both lubrication and as hydraulic actuating fluid of the cam phase actuator. The cam actuator command voltage signal is generated by the Opal-RT prototype controller and sent to the solenoid driver. The PWM duty cycle is linearly proportional to input voltage with maximum duty cycle (99%) corresponding to 5V. The solenoid actuator controls the hydraulic fluids (engine oil) flow and changes the cam phase. The cam position sensor signal is sampled by

the Open-RT prototype controller and the corresponding cam phase is calculated within the Opal-RT real-time controller.

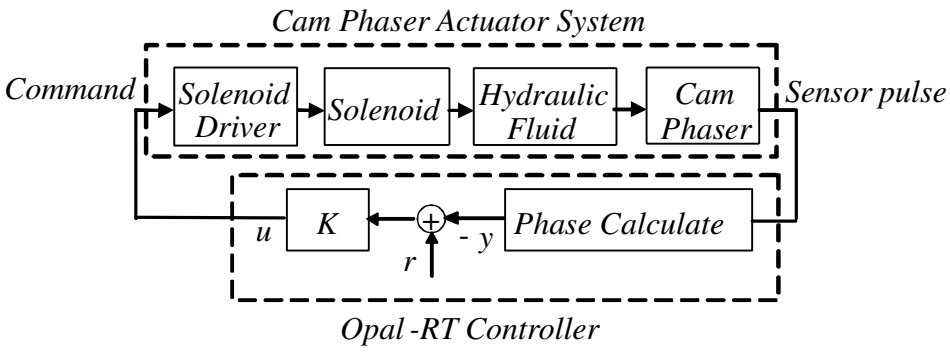


Figure 3-8. VVT system Diagram

Within an engine cycle, the cam position sensor generates four cam position pulses sampled by the Opal-RT real-time controller. By comparing these pulse locations with respect to the encoder gate signal, the Opal-RT controller calculates the cam phase with one crank degree resolution. After the error between the calculated cam phase and the cam reference signal is obtained, the cam actuator control command is obtained from the controller K. Figure 3-8 shows the signal diagram of the VVT control system. Reference signal r and the measured cam phase signal r can be recorded in the Opal-RT controller for system identification. In this paper, "system model" refers to the transfer function between the control input r0 (voltage) and calculated cam phase signal r3 (degree); "controller" refers to transfer function r3 between the error and output.

3.5.2 VVT Open-loop Properties

The cam phase actuator has an output range of ± 30 crank degrees. Figure 3-9 shows an open-loop step response of the VVT phaser. Input to the system is a step between 0V (1% duty cycle) and 5V (99% duty cycle). It can be found that the cam phase system has a settling time about 1.5 seconds for advancing (rising) and 1.0 second for retard (falling), demonstrating its

nonlinear characteristics of the VVT system. This is mainly due to the fact that the VVT pulley (See Figure 3-10) has different dynamics for advancing and retarding. For advancing, the actuating torque generated by the oil pressure overcomes the cam load torque and moves the cam phase forward; and for retarding, the oil trapped in the actuator bleeds back to the oil reserve when the cam phase is pushed back by the cam shaft load. This difference leads to the response characteristics difference for advance and retard operations, which makes the system nonlinear. This phenomenon will be discussed in bench test section.

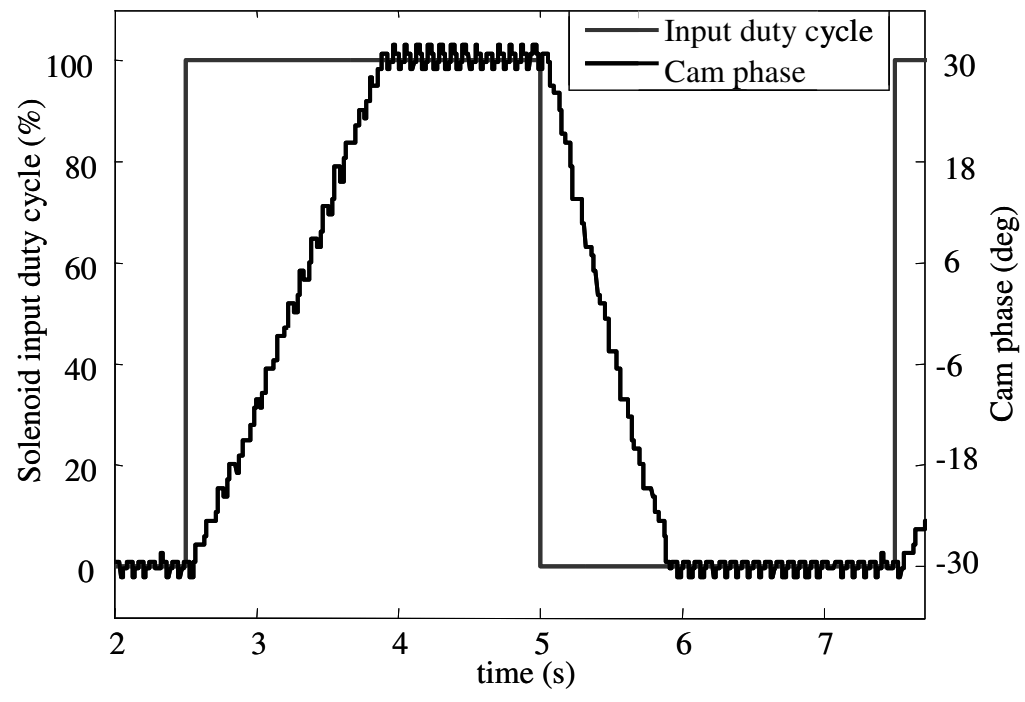


Figure 3-9. Cam phase actuator open-loop step response

Figure 3-11 shows the VVT system steady-state responses via open-loop constant inputs with a 0.1V interval (2% duty cycle) between 0 and 5 volts. It can be observed that for open-loop control, the cam phase actuator behaves almost like a binary state, and it is very difficult for the VVT actuator to maintain at a desired non-saturated cam timing position due to the actuator hysteresis characteristics, cam load and engine oil pressure variations. This indicates that open-loop system identification, which requires to hold the actuator operate at a desired location

during the system identification process, is almost impossible. Therefore, closed-loop system identification is adopted in this research. A proportional controller is selected for the closed-loop system identification in order to ensure good closed-loop system identification accuracy ([38], and [46]).

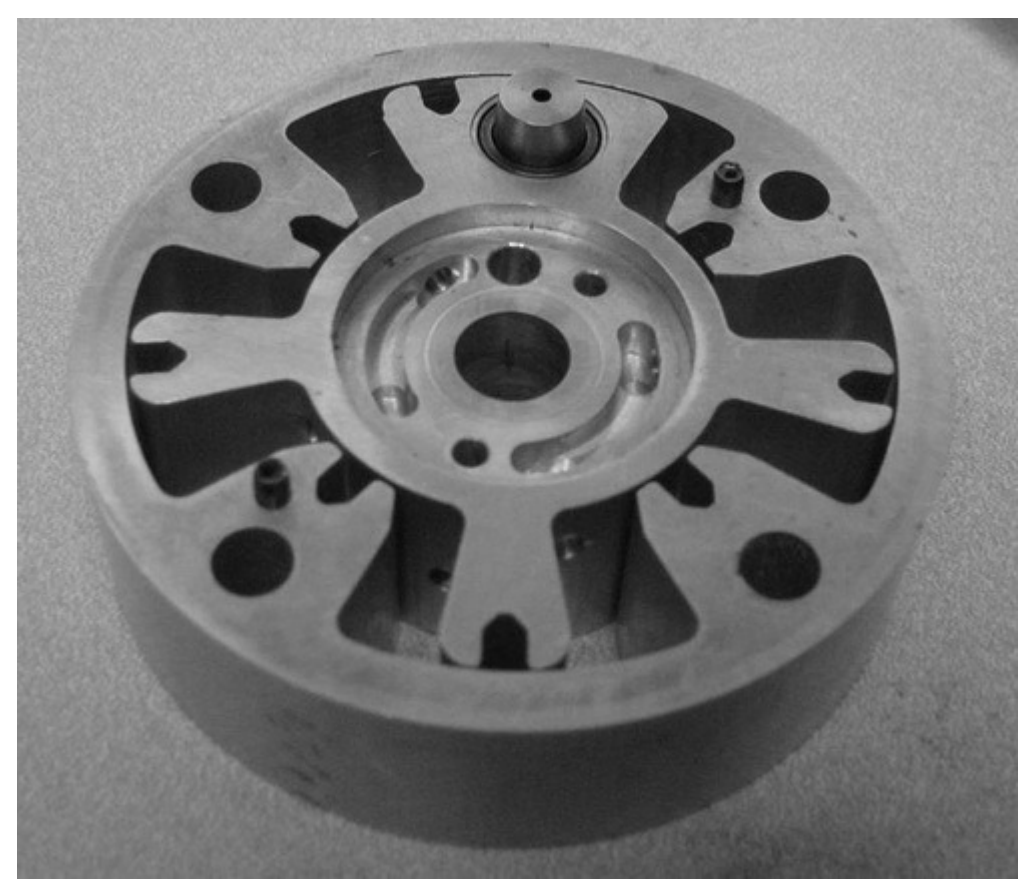


Figure 3-10. Vane type cam phase hydraulic pulley

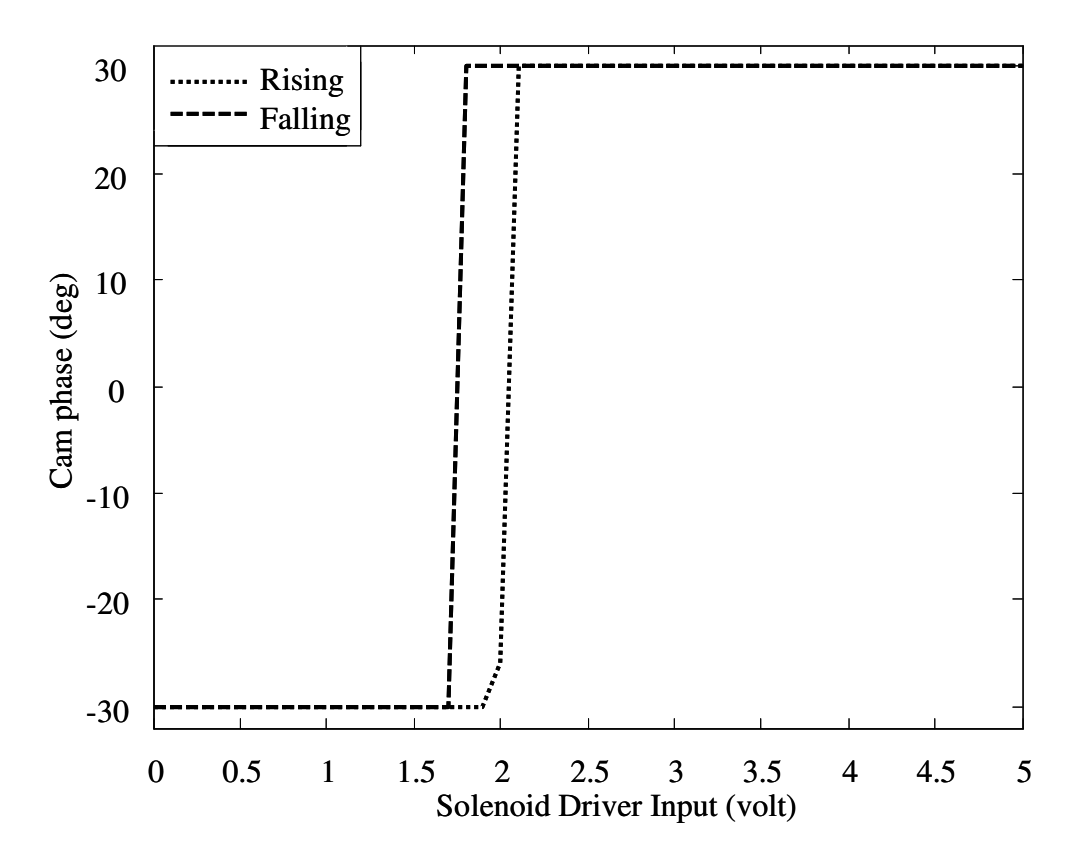


Figure 3-11. Cam phase actuator open-loop steady-state responses

3.6 Bench Test Results

3.6.1 Closed-loop Identification

The operating point and controller gain need to be selected carefully due to the system property. The solenoid drive circuit has an operational range between 0 and 5 volts that corresponds to 1 and 99 percent of the solenoid PWM duty cycle. Therefore, in order to avoid saturation, we have to select the phase actuator operation condition carefully; otherwise, the control input might be saturated, leading to high system identification error. Therefore, the PRBS signal magnitude was selected to be 12°, nominal operational condition was centered at -14° cam phase, and the controller proportional gain was 0.1 (volt/degree). To obtain a family of system transfer functions, the system identification bench tests were conducted at different engine speeds and oil pressures. For demonstration, we selected two engine speeds at 1000 and 1500

rpm and a constant oil pressure of 60 psi. Recorded reference signals and system response data were processed using MATLAB PRBS-GUI [26].

Table 3-2. System identification parameters

Engine Speed (rpm)	1000	1500
Input Sample Rate (ms)	5	5
Output Sample Rate (ms)	30	20
Output/Input Sample Ratio	0.167	0.25
PRBS order	13	13
Signal length (s)	81.88	81.88
Markov parameter. #	90	60
ID open-loop model order	4	2 and 4

The number of Markov parameters to be matched by system identification was used to optimize the identification accuracy (see Figure 3-12). Identified system model order was determined by the dominant dynamics of PRBS response data (see Figure 3-13). Figure 3-13 shows the order selection diagram produced during PRBS system ID at 1500 rpm. It shows the diagonal elements of Schur decomposition of the system response data matrix. The diagonal elements of the Schur decomposition were plotted in a decreased order. Each dot in the plot corresponds to one state of the identified model. Detailed algorithms can be found in [26]. The plot shows a dominant first order dynamic because the order index chart has the largest gap between the first and second dots. The gap between fourth and fifth dots is larger than the gap between second and third dots. Therefore, the order of the identified model was selected to be four in order to keep the model order low without losing major system dynamics. The rest of system identification parameters are shown in Table 3-2.

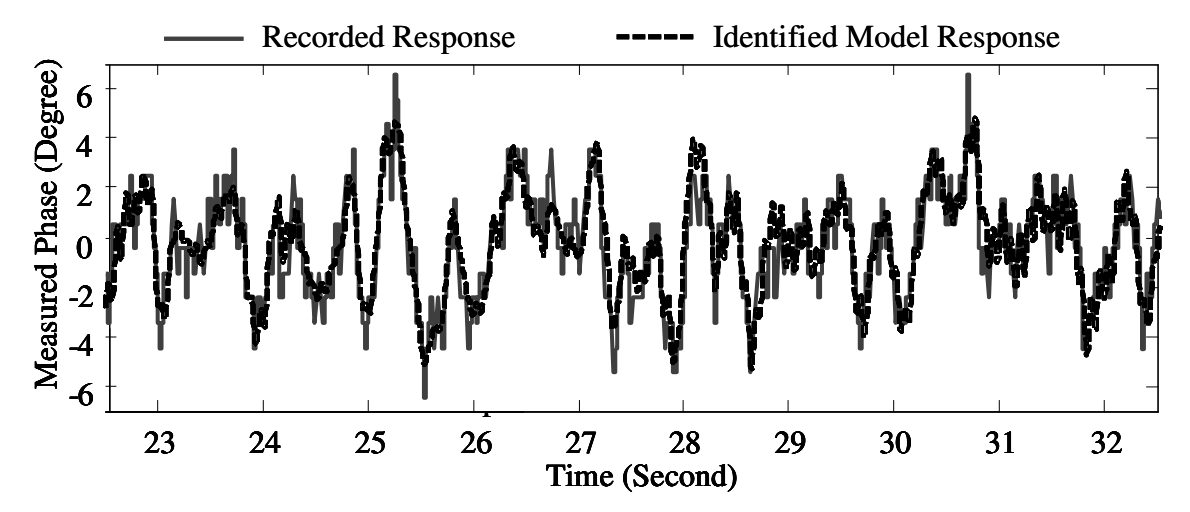


Figure 3-12. Identified and physical responses

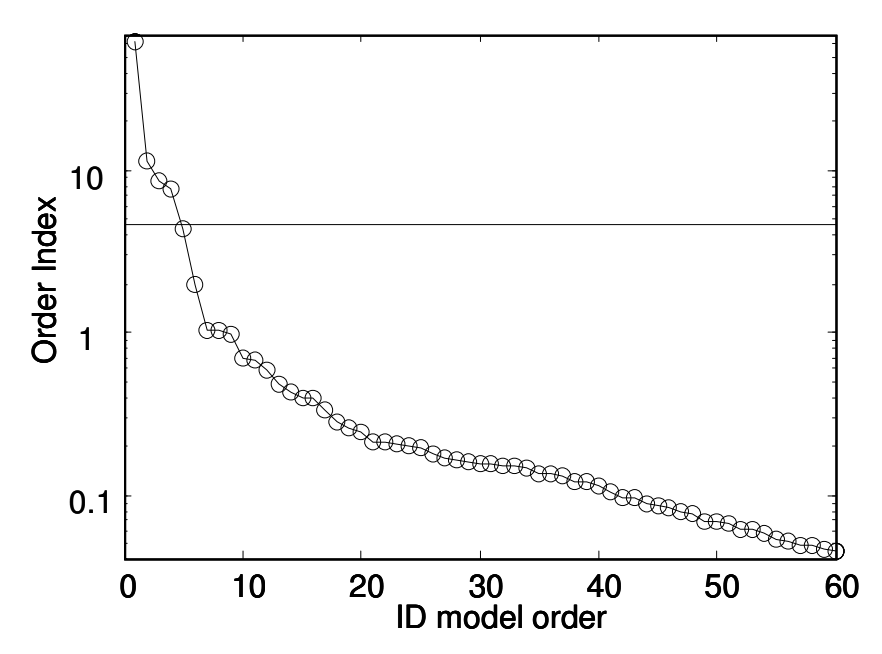


Figure 3-13. Identified model order selection

Using the identified closed-loop model and equation (3.2), a fourth order open-loop plant model (see Table 3-3) at 1500 rpm is obtained. The corresponding open-loop Bode diagram (Figure 3-14) shows that there exists a dynamic mode at around 12.5 Hz, which is equal to the engine cycle frequency of 12.5 Hz (80ms/cycle) at 1500 rpm. It is believed that the resonance observed was not due to the system dynamics of the cam phaser system but rather the external disturbance due to the cyclic dynamics of the timing belt and cam shaft torque disturbance due to

valve actuations. Therefore, we decided to exclude it from the identified model used for control design. A second order model is obtained by selecting the order of identified closed-loop model to be two. Plant model calculated from the identified second-order model has almost identical behavior to the fourth-order model without the 12.5 Hz mode (see Figure 3-14 and Table 3-3).

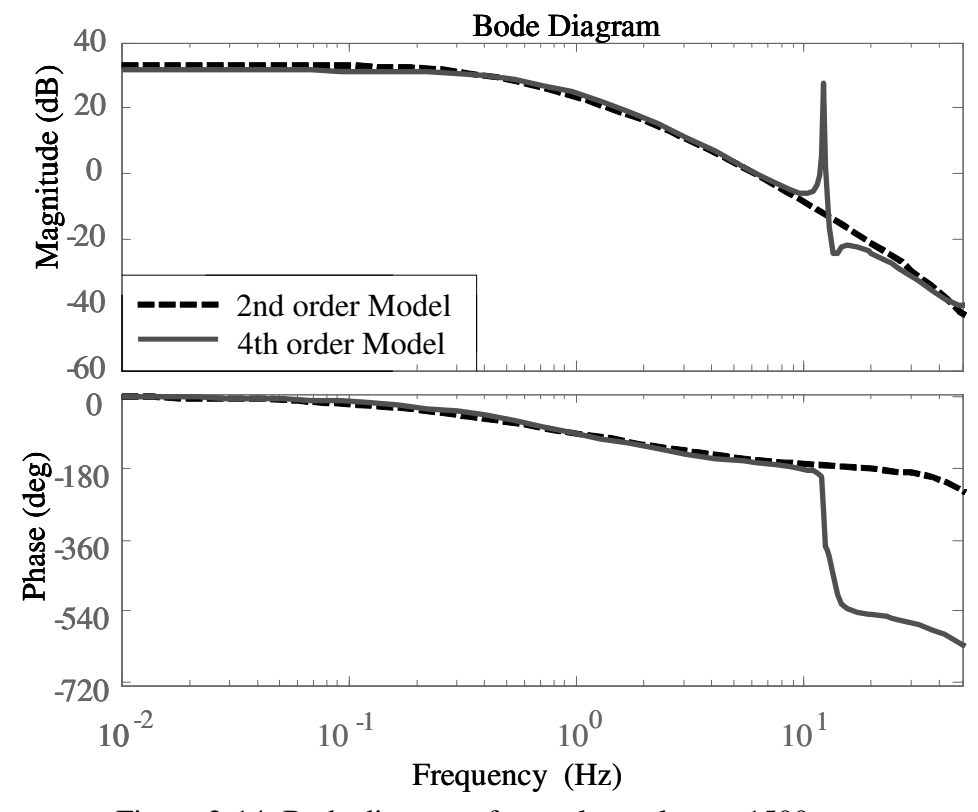


Figure 3-14. Bode diagram of open-loop plant at 1500 rpm

A fourth-order closed-loop model was identified at 1000 rpm. Similar to the case at 1500 rpm, the identified model has a dynamic mode at about 8 Hz, which corresponds to the engine cycle period (8.3 Hz, 120ms/cycle). However, in this case, a second-order open-loop model was not obtained directly from system identification. Note that in this case there exists a pair of non-minimal phase zeros shown in the Root Locus (Figure 3-15) at the frequency close to engine cycle frequency. To eliminate the dynamics at this frequency, a second order model was obtained by removing the pairs of pole-zero from the fourth-order plant model (Table 3-3). The second-

order plant model has very similar frequency response to the fourth-order plant model except without the dynamics introduced by the cyclic engine cam load (Figure 3-16).

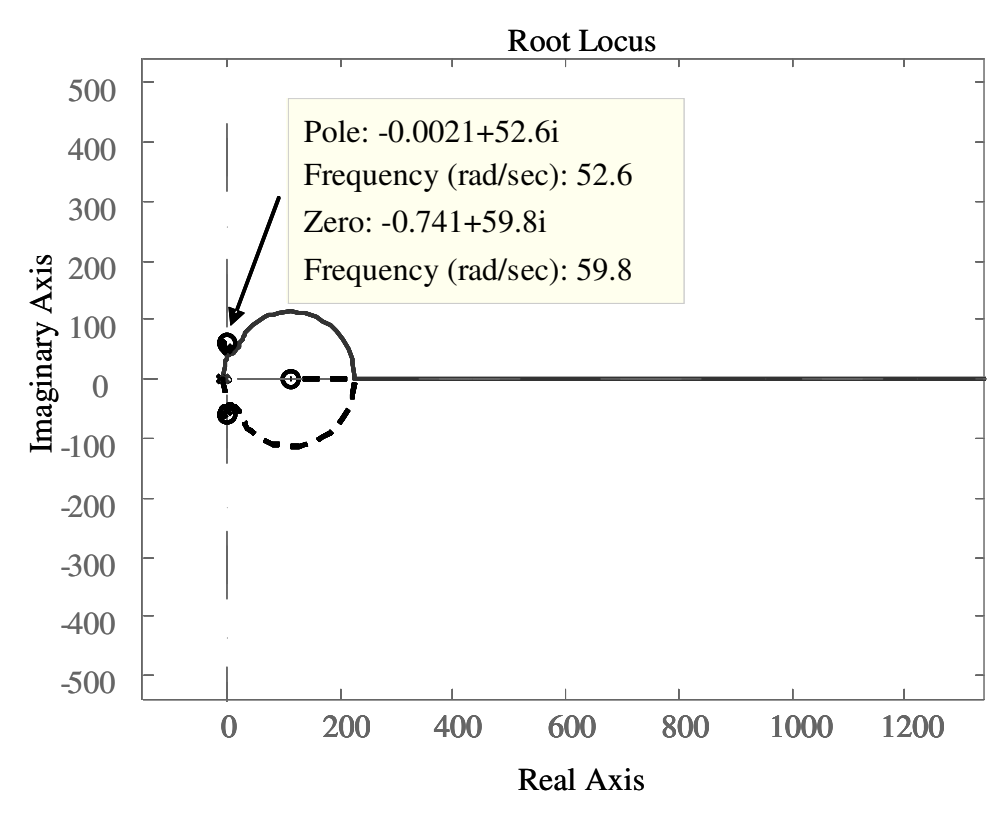


Figure 3-15. Root locus of the identified fourth-order plant at 1000 rpm

Table 3-3. Identified open-loop plant transfer functions

Condition	Open-loop Plant Transfer Function		
1000 rpm, identified fourth-order model	$G_{1000rpm_4}(s) = \frac{3.6 \times 10^{-4} s^4 - 5.3 s^3 + 586 s^2 - 1.8 \times 10^4 s + 2.1 \times 10^6}{s^4 + 11.63 s^3 + 2780 s^2 + 3.21 \times 10^4 s + 4.6 \times 10^4}$		
1000 rpm, calculated second-order model	$G_{1000rpm_2}(s) = \frac{3.56 \times 10^{-4} s^2 - 5.27s + 592.2}{s^2 + 11.63s + 16.7}$		
1500 rpm, identified fourth-order model	$G_{1500rpm_4}(s) = \frac{0.012s^4 - 3.1s^3 + 1354s^2 - 2.9 \times 10^4 s + 9.0 \times 10^6}{s^4 + 14.54s^3 + 5971s^2 + 8.54 \times 10^4 s + 2.38 \times 10^5}$		
1500 rpm, identified second-order model	$G_{1500rpm_2}(s) = \frac{0.0124s^2 - 2.04s + 1582}{s^2 + 16.78s + 34.82}$		

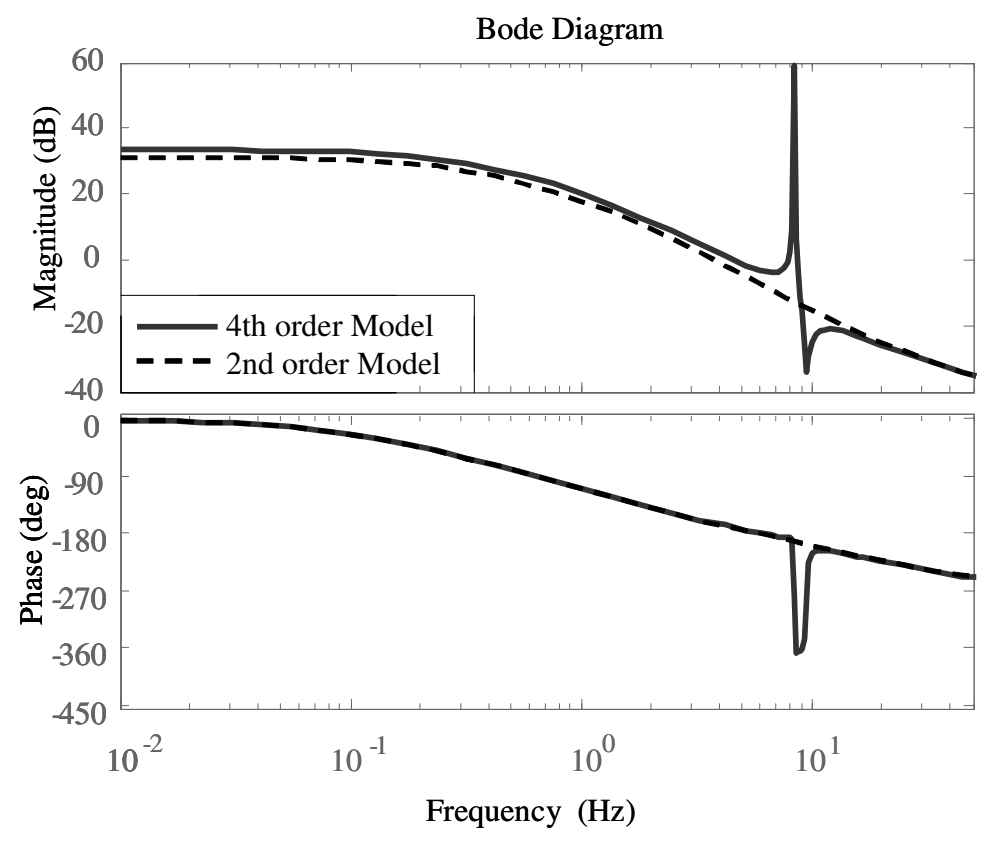


Figure 3-16. Bode diagram of open-loop plant at 1000 rpm

3.6.2 Validation of Identified Model

To evaluate the accuracy of these identified models, their step responses were compared with those from the bench tests. Since the open-loop step response cannot be obtained for the VVT actuator, their closed-loop responses were compared in this study. The same proportional control gain of 0.1 Volts/degree was used for the step responses. A step input of 12 crank degrees was used. For the identified models, simulations were conducted in Simulink under the same conditions. The normalized step responses are compared in Figure 3-17 at 1000 rpm and Figure 3-18 at 1500 rpm. Note that the oscillations in the recorded responses are mainly due to the cyclic valve torque load disturbance and low cam phase sampling resolution, which demonstrates the difficulty for a proportional controller to maintain the cam phase at a desired level.

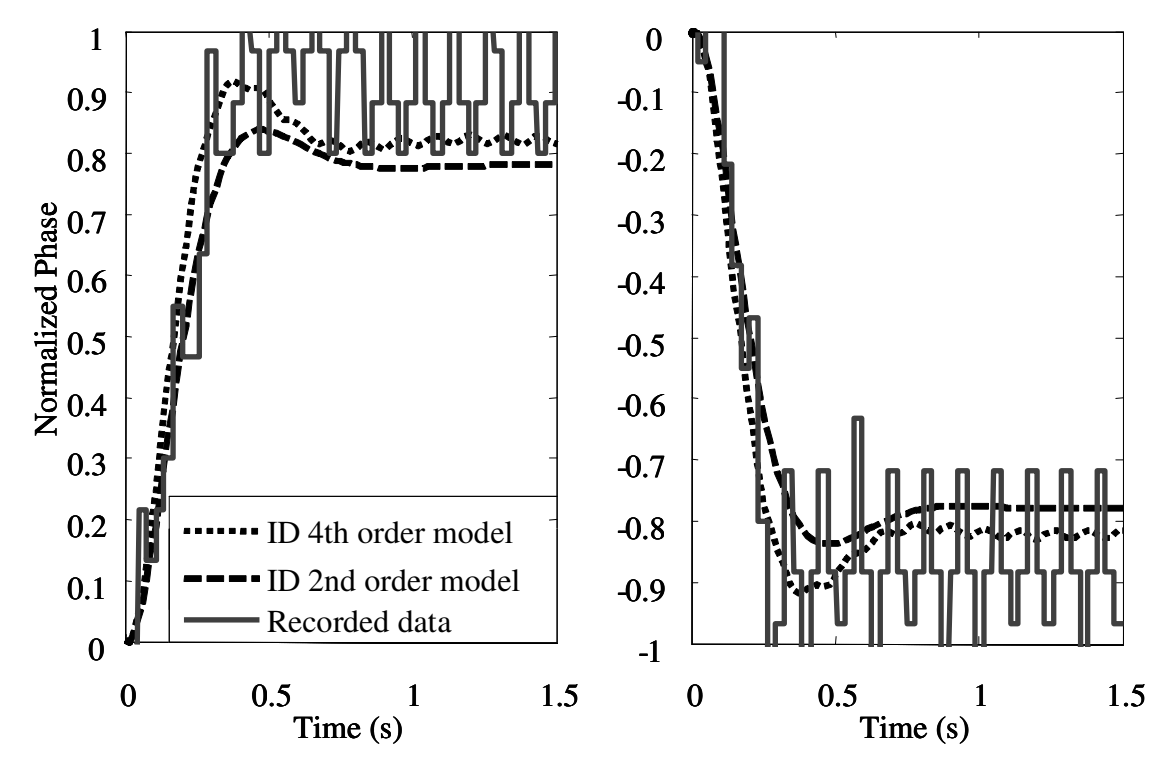


Figure 3-17. Closed-loop step response comparison at 1000 rpm

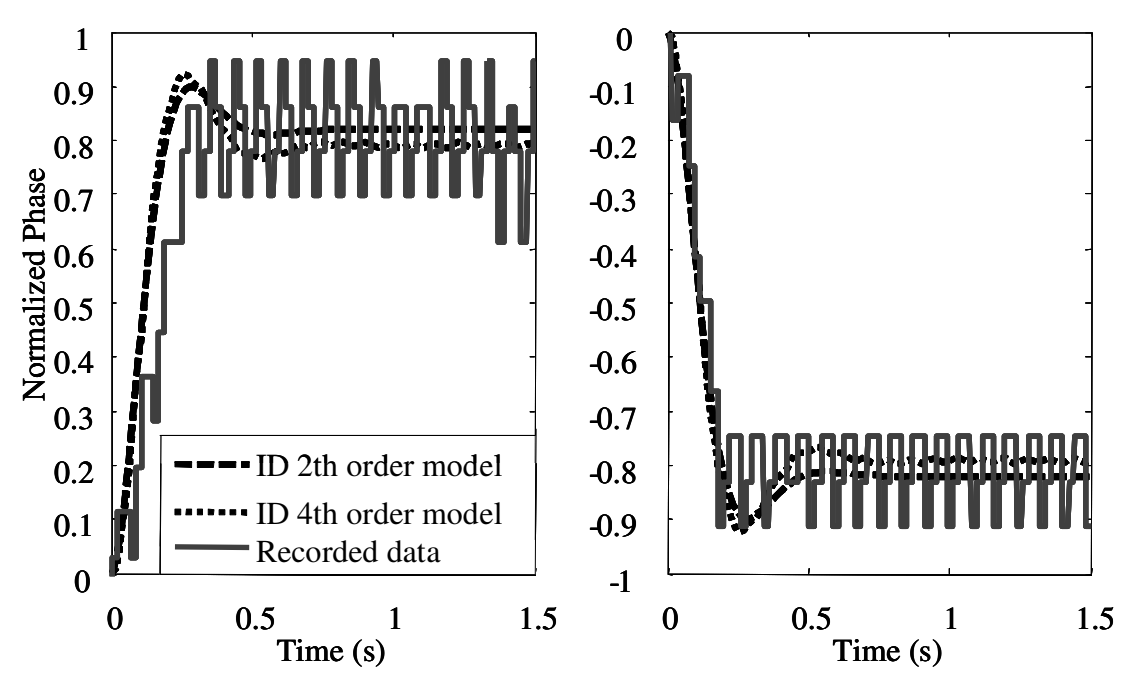


Figure 3-18. Closed-loop step response comparison at 1500 rpm

From both Figure 3-17 and Figure 3-18, it can be observed that the system DC gains of both the actual system and the identified model are fairly close; and for the transient response,

the step down responses are very close for both the model and actual system at both engine speeds, but the step up responses of the identified model at 1500 rpm is faster than the actual system. This is mainly due to the nonlinear characteristics of the VVT actuator discussed in the VVT open-loop property section. When cam phase is advanced, the VVT actuator is driven by the engine oil pressure to overcome the cam shaft torque load, while when cam phase is retarding, the VVT actuator is pushed by cam load torque and returns freely. This is why the system has different step up and step down responses. The test results show that the identified mode approximates the step down response.

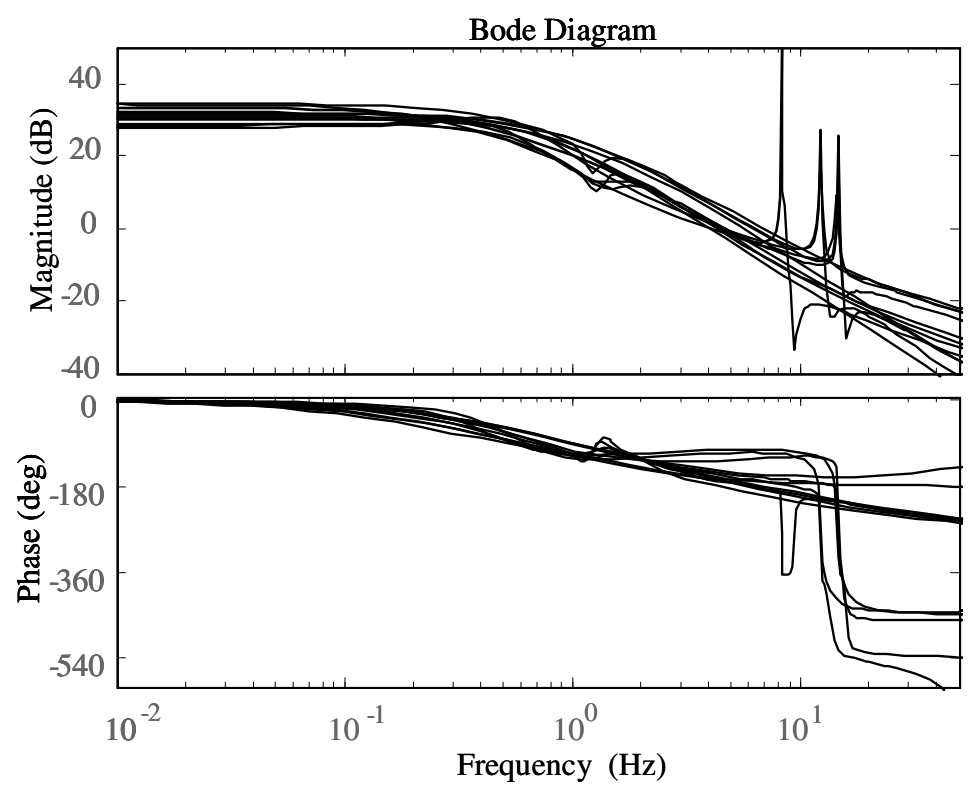


Figure 3-19. Family of Identified models

A family of system models was obtained from bench tests at different engine speeds and oil pressures (Figure 3-19). A second-order model (3.27) was selected as the nominal model for control design below

$$G = \frac{0.0003s^2 - 0.06s + 647.2}{s^2 + 7.615s + 20.67}$$
(3.27)

Note that this system plant has a pair of non-minimal phase zeros, indicating that high control gain will destabilize the closed-loop system.

3.6.3 OCC Controller with Signal Input

In this section, controllers were designed and validated on the test bench. The step input was used as reference signal and varies between -20 and 0 degrees. A PI controller was well tuned for the VVT system on the test bench for comparison purpose. The PI tuning process was completed at different engine speeds and oil pressures. The tuned PI controller (3.28) achieves good balance between fast response time and little oscillations at different conditions

$$K_{base}(s) = 0.2 + \frac{0.1}{s} \tag{3.28}$$

For the OCC design, system plant matrices of the nominal model were obtained from equation (3.27)

$$\mathbf{A}\mathbf{p} = \mathbf{A} = \begin{bmatrix} -7.62 & -20.68 \\ 1 & 0 \end{bmatrix} \qquad \mathbf{B}\mathbf{p} = \mathbf{D}\mathbf{p} = \mathbf{B} = \begin{bmatrix} 1 \\ 0 \end{bmatrix}$$

$$\mathbf{C}\mathbf{p} = \mathbf{M}\mathbf{p} = \mathbf{C} = \begin{bmatrix} -0.063 & 647.39 \end{bmatrix} \qquad \mathbf{D} \cong \mathbf{0}$$
(3.29)

Controller design parameters were selected as

$$\mathbf{W_p} = 1, \quad \mathbf{V} = 0.01, \quad \mathbf{R} = [1]$$
 (3.30)

Using the OCC iterative control design algorithm in [35], an OCC controller was obtained

$$K_{occ_direct}(s) = \frac{194.8 \text{ s} + 2701}{s^2 + 131s + 8582}$$
(3.31)

However, the controller was not able to maintain the cam phase at the desired level, and it has large steady-state error (see Figure 3-20). To improve the performance, an integrator was

added to the plant to eliminate steady-state error (see Figure 3-21). A fourth-order controller (the third-order OCC controller plus the first-order integrator) was obtained below:

$$K_{occ-i} = \frac{-239.9s^2 - 2751s - 1.1 \times 10^4}{s(s^3 + 51.3s^2 + 1305s + 1.97 \times 10^4)}$$
(3.32)

Notice that the order of plant used for controller design is increased by one and as a result the order of the full order controller is also increased by one. After combining the full order controller with the added integrator, the order of the new controller is increased by two compared with the original controller.

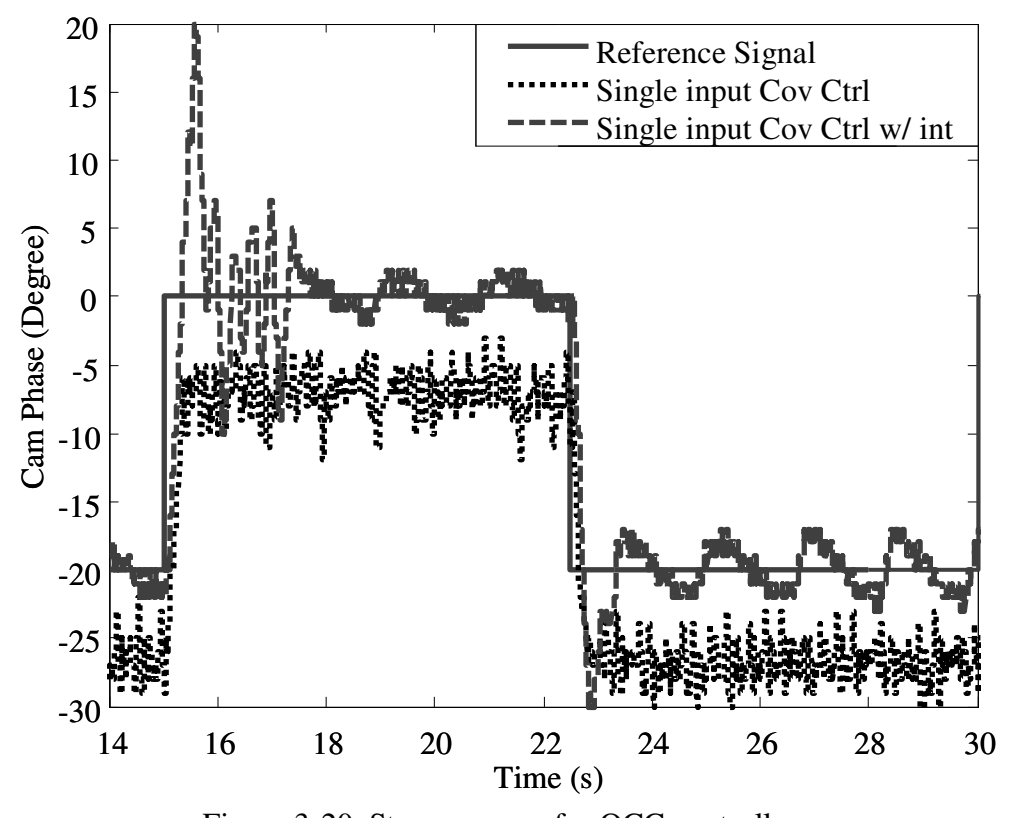


Figure 3-20. Step response for OCC controllers

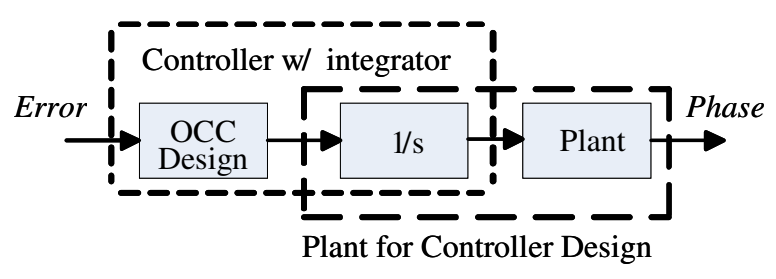


Figure 3-21. OCC design framework with an integrator

The OCC control with integrator has a large overshoot with oscillations (Figure 3-20). In order to eliminate steady-state error and reduce response time, a multi-input control design with proportional and integral inputs was proposed.

3.6.4 OCC Controller Design with Multi-input

For the dual-input control design, the controller has an additional integrator input to the plant (Figure 3-22). Noise intensity matrices W_p and V were the same as (3.28). The input weighting matrix dimension increased to two due to additional integral input and it was selected as $\mathbf{R} = diag[1\ 20]$. Note that in this case the input effort cost ratio between direct control and integral control is 1 to $\sqrt{20}$. The dual-input controller was designed and shown in (3.33), and its performance at 900 rpm with 45 psi oil pressure is compared with the base PI controller in (3.28). Figure 3-23 shows that both controllers have very similar response times and steady-state errors and the OCC controller has significantly less overshoot. The major reason for the OCC controller (with an integrator) to have less overshoot than that of the PI controller, is due to the fact that the full-order OCC controller contains more dynamics than the PI controller.

$$K_{occ-2in} = \frac{84.5s^3 + 935.2s^2 + 1164.5s + 220}{s^4 + 122.2s^3 + 7464.7s^2 + 3022s}$$
(3.33)

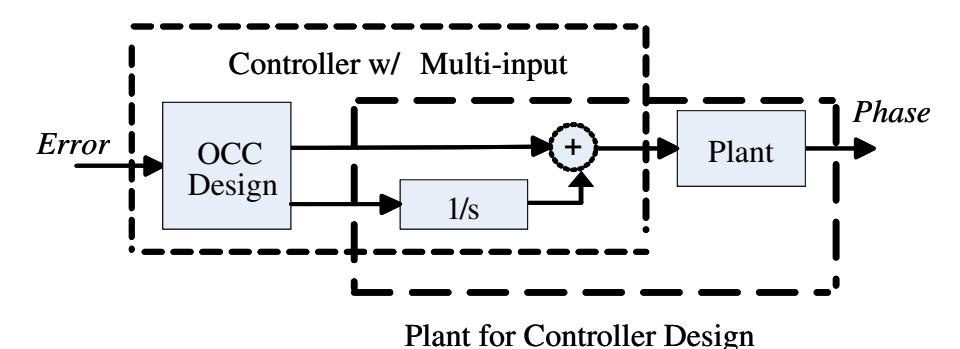


Figure 3-22. Multi-input OCC design framework

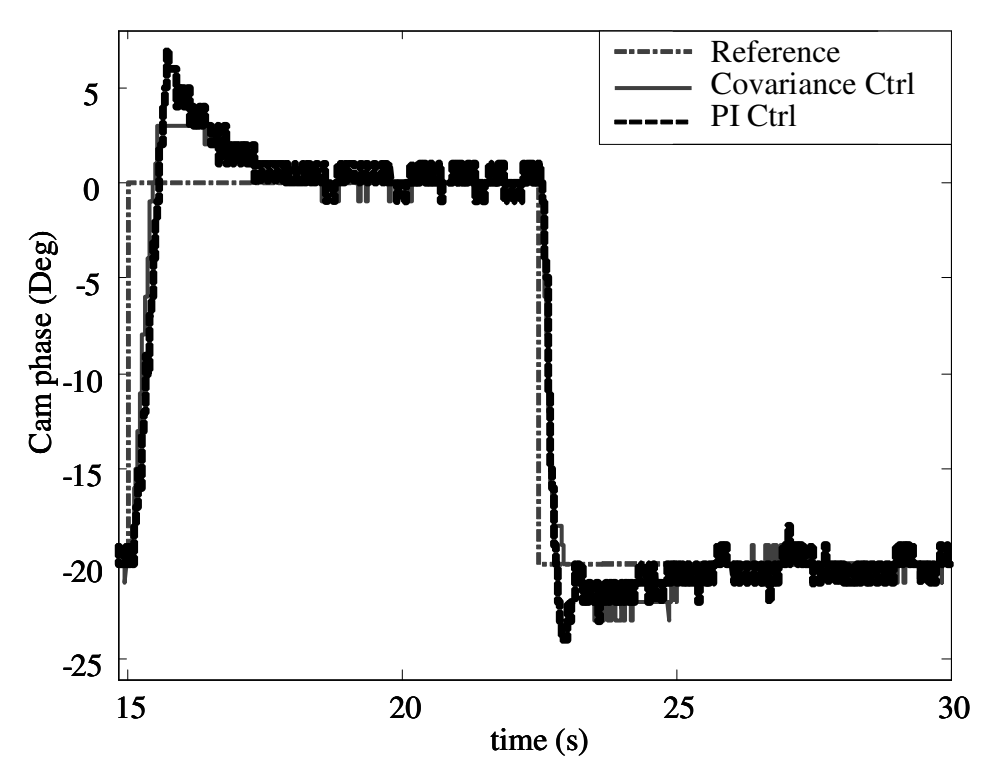


Figure 3-23. Step response comparison

3.6.5 Controller Performance Comparison

Table 3-4 shows the system response comparison of the PI and multi-input OCC closed-loop systems. Both controllers have zero steady-state error, with oscillation magnitude of 1 degree (lowest possible and limited by measurement resolution). Both controllers have almost identical 5% (within 1 degree) settling time and 10~90% rising time. Compared with the base line PI controller, the OCC controller has much lower overshoot. In some operational conditions, the OCC controller reduces PI controller's overshoot by 50%. For the advance step (from -20 to

0 degree), multi-input OCC controller uses less control effort than the PI controller. In the retard step, the control effort difference is small (Figure 3-24). The reason is that in the advance step, all the control effort is created by the actuator; while in the retard step, engine oil pressure is working with the actuator. At steady-state, the dual-input OCC controller shows larger oscillation magnitude than that of the PI controller. This is due to the fact that the designed OCC controller has a higher gain than the PI controller and therefore is more sensitive to the change in the error signal, which has the resolution of one crank degree in this experiment. In the following section, robust gain scheduling control design using identified models at different operating conditions will be studied.

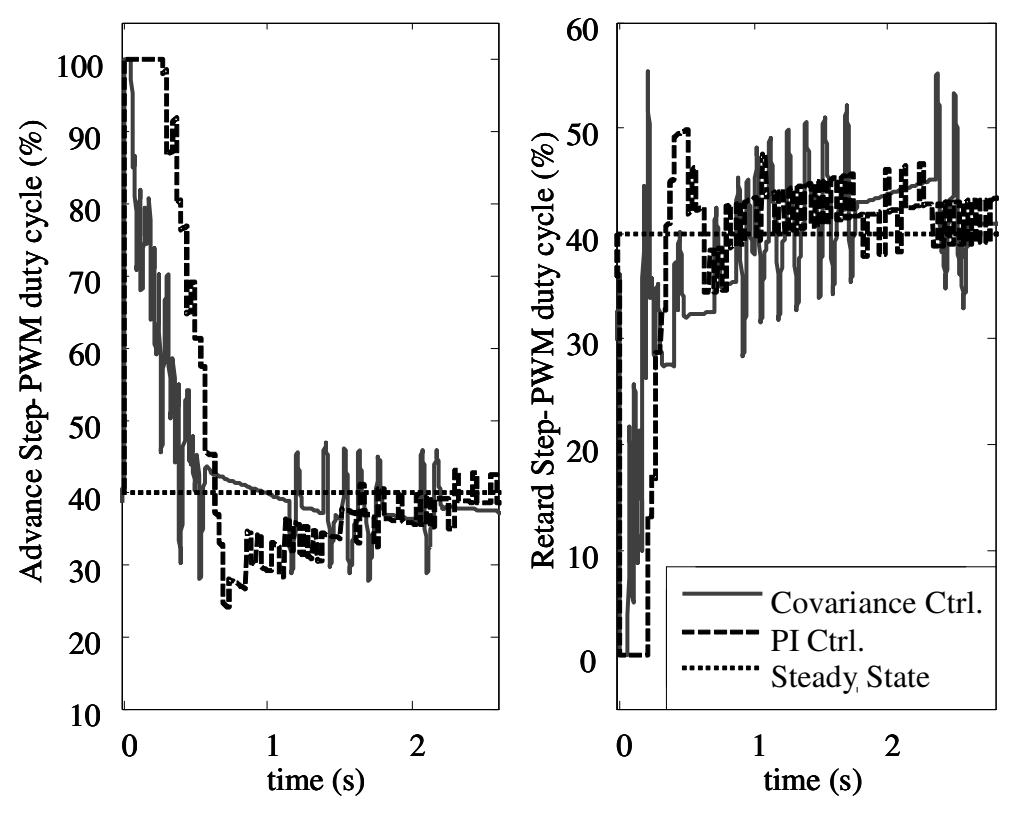


Figure 3-24. Control effort comparison at 900 rpm with 45 psi oil pressure

Table 3-4. Controller performance comparison

Engine	Oil	Advanced Performance					
Speed pre	pressure	Overshoot (deg)		Settling Time (s)		Rising Time (s)	
	(psi)	PI	OCC	PI	OCC	PI	OCC
900	45	7	3	2.16	2.24	0.39	0.34
1200		5	4	2.39	2.20	0.36	0.32
1500	43	5	4	2.01	2.26	0.32	0.28
1800		6	4	2.10	1.98	0.33	0.26
900		6	3	2.26	2.01	0.33	0.24
1200	60	6	3	2.49	2.00	0.30	0.20
1500	60	6	3	1.71	1.97	0.28	0.18
1800		5	3	1.61	1.84	0.25	0.18
Engine	Oil	Retard Performance					
Speed	pressure (psi)	Oversho	oot (deg)	Settling Time (s)		Rising Time (s)	
(rpm)		PI	OCC	PI	OCC	PI	OCC
900	- 45	4	3	2.38	2.10	0.19	0.17
1200		5	3	1.86	2.03	0.17	0.15
1500		3	3	1.91	2.1	0.20	0.21
1800		4	3	1.82	2.02	0.18	0.21
900	60	6	3	2.57	1.92	0.17	0.14
1200		5	3	1.82	1.88	0.20	0.20
1500		5	3	1.84	1.98	0.16	0.21
1800		5	3	1.84	1.82	0.16	0.20

3.7 LPV Design

A linear parameter varying (LPV) controller was designed as a performance comparison to OCC controller. The tests were done using the same hardware setup as the previous bench tests. In order to obtain parameters at different operating conditions, discrete VVT plant models are identified and simplified. Through the study of the identified models, it is found that the pole

locations of the models are all very close to each other. Engine speed and oil pressure contributes mainly to the DC gain and zero locations of the models respectively. As a result, models are assumed to have the same pole location. Gains of the models are determined by the engine speed (Table 3-5), and zero locations are determined by the engine oil pressure (3.34).

$$G_{45psi} = K \frac{0.0859049z - 0.0608905}{z^2 - 1.954698z + 0.955255}$$

$$G_{60psi} = K \frac{0.0614708z - 0.0364564}{z^2 - 1.954698z + 0.955255}$$
(3.34)

Table 3-5. Plant gains At different operating conditions

Engine Oil	Engine Speed			
Pressure	900 rpm	1500 rpm	1800 rpm	
45 psi	0.70	0.72	0.68	
60 psi	0.95	0.98	0.93	

The system response at 1200 rpm and 60 psi is shown in Figure 3-25. Mean performance of advanced and retard steps are listed in Table 3-6 and Table 3-7. The results show that all the controllers have almost identical rising time for the advance step. LPV and PI controllers have similar settling time and rising time for the retard step, while the OCC controller is slightly slower. The OCC controller has the lowest and the PI controller has the highest overshoot, with the LPV controller in between. The OCC controller has the lowest and the PI controller has the highest control effort, with the LPV controller in the middle (Figure 3-26).

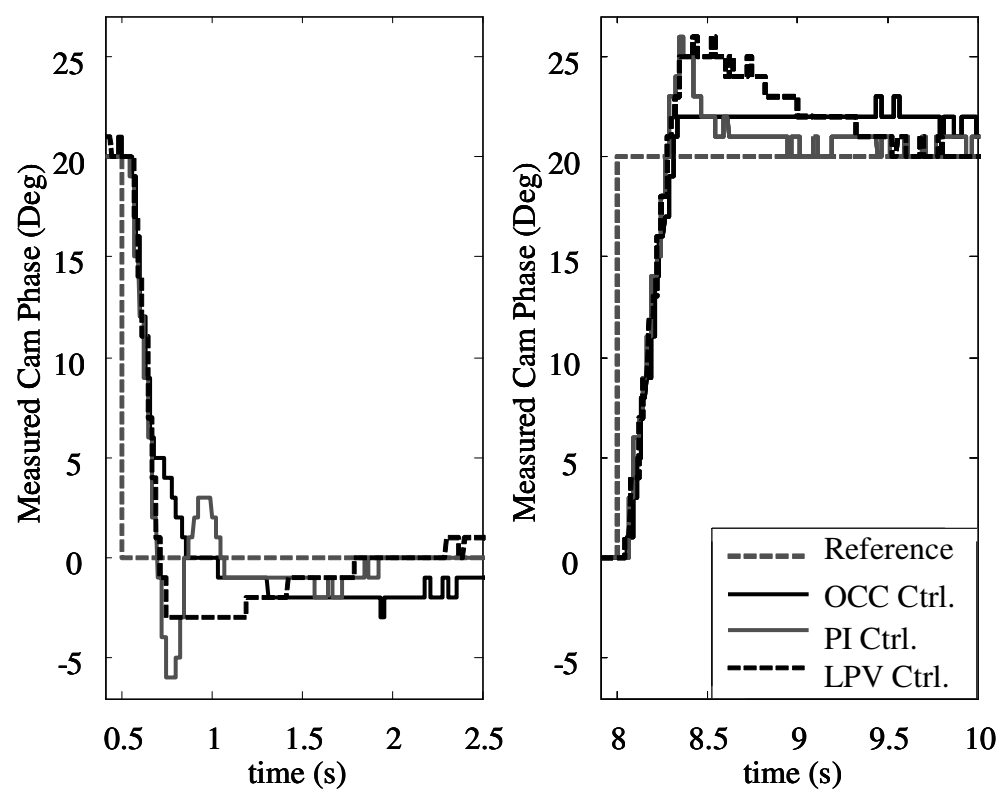


Figure 3-25. Step response comparison of OCC, PI and LPV controllers

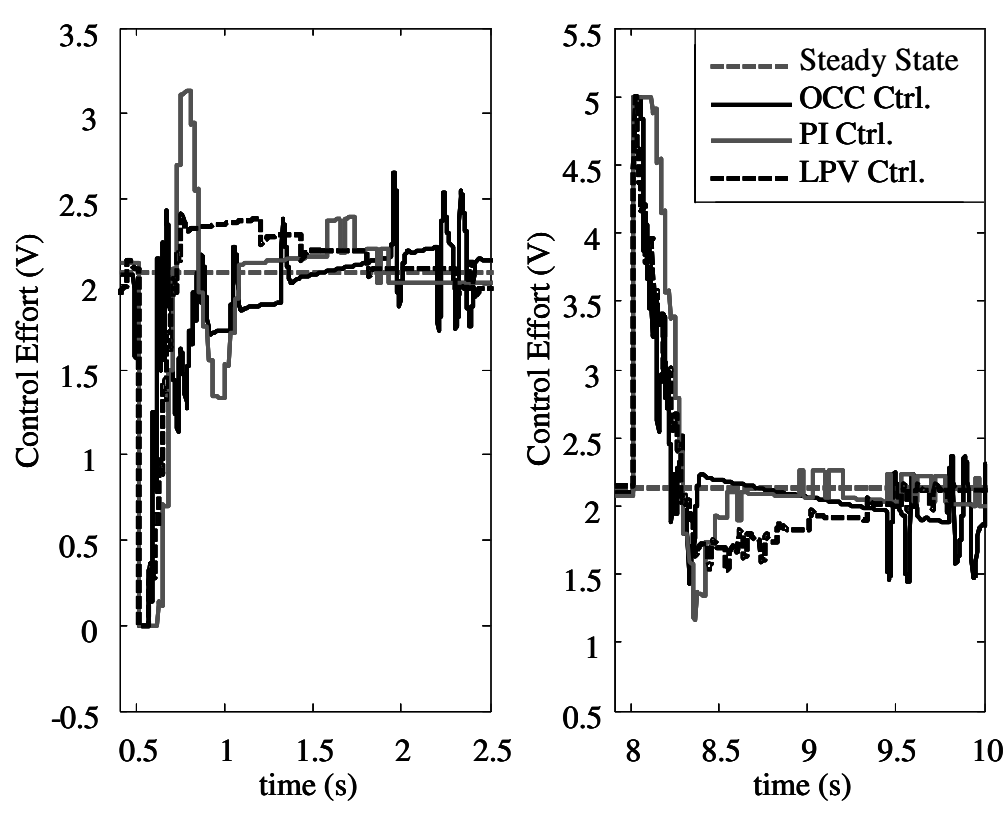


Figure 3-26. Control effort comparison of OCC, PI and LPV controllers

Table 3-6. Controller mean advance performance comparison

Engine Oil Pressure	Engine	Overshoot (deg)			Settling Time (s)			Rising Time (s)		
	Speed (rpm)	OCC	PI	LPV	OCC	PI	LPV	OCC	PI	LPV
	900	4.1	5.7	5.0	2.27	1.59	2.02	0.31	0.31	0.30
45nei	1200	4.0	5.5	4.5	2.23	1.63	2.02	0.31	0.30	0.31
45psi	1500	4.2	5.3	4.5	2.09	1.69	2.07	0.29	0.30	0.30
	1800	4.2	5.5	4.8	2.09	1.59	2.34	0.29	0.28	0.29
	900	3.7	6.1	5.8	2.18	1.84	1.93	0.24	0.25	0.23
60noi	1200	3.5	6.1	5.3	2.05	1.37	1.64	0.20	0.22	0.23
60psi	1500	3.3	5.6	5.1	2.06	1.02	1.62	0.21	0.21	0.21
	1800	3.9	6.0	5.2	1.92	1.73	1.75	0.20	0.20	0.20

Table 3-7. Controller mean retard performance comparison

Engine Oil Pressure	\ \ \ \ \ \ \ \ \ \ \ \ \ \ \ \ \ \ \ \			Settling Time (s)			Rising Time (s)			
	Speed (rpm)	OCC	PI	LPV	OCC	PI	LPV	OCC	PI	LPV
	900	3.6	4.8	3.9	2.21	1.91	1.32	0.23	0.16	0.16
45psi	1200	3.6	4.2	3.6	2.27	1.40	1.61	0.24	0.17	0.16
43psi	1500	3.1	3.6	3.3	2.16	1.45	1.43	0.26	0.16	0.16
	1800	4.0	4.1	3.0	2.00	1.90	2.17	0.23	0.16	0.16
	900	3.0	5.5	4.0	2.32	1.98	0.89	0.18	0.16	0.16
60nci	1200	3.0	5.2	3.9	2.10	1.54	1.20	0.21	0.15	0.14
60psi	1500	3.0	4.7	3.4	2.00	1.55	1.14	0.25	0.13	0.13
	1800	3.5	4.6	3.2	1.90	1.80	1.39	0.21	0.13	0.13

3.8 VVT System Engine Dynamometer Test Setup

The closed-loop system identification and controller design were also conducted on an engine dynamometer (dyno). A single cylinder engine with a dual hydraulic VVT system was used in the test. The test engine is a 0.4 Liter, single cylinder, direct injection (DI) gasoline

engine (Figure 3-27). The VVT system itself is very similar to the one used on the test bench (Figure 3-7). The main difference is that intake and exhaust timings can be adjusted and measured independently on the test engine. Both intake and exhaust cam valves can be advanced or retarded by 20 degrees. Also, the cam phase is calculated every engine cycle instead of 4 times every cycle on the bench. The engine does not require a separate electric oil pump; as a result, the engine oil pressure can no longer be adjusted from outside. The cyclic load disturbance on the cam shaft was much greater than the cam shaft load on the VVT test bench because the engine was combusting during the tests.



Figure 3-27. Single cylinder engine on the engine dyno

The engine dyno is controlled from the control room (Figure 3-28). The engine speed is controlled by the dyno controller and can be maintained at a desired speed. An A&D Technology Combustion Analysis System (CAS) system is used to monitor the combustion stability. An

Opal-RT system is used as an engine controller, and it collects all the sensor signals from the engine and sends out control signals to the engine. The throttle is fixed at a low load position. An oxygen sensor, similar to the one used on a passenger vehicle, is used to monitor the air-fuel ratio. The fuel quantity is manually controlled in the Opal-RT system so that air-fuel ratio is at stoichiometric point.

An Opal-RT system used in the dyno test is able to calculate cam position with a resolution of 1/64 degree. However, the cam phase calculation in Opal-RT was calibrated using CAS. Due to the resolution limit of the CAS system (1 crank degree), the cam phase calculation only has an accuracy of one crank degree.

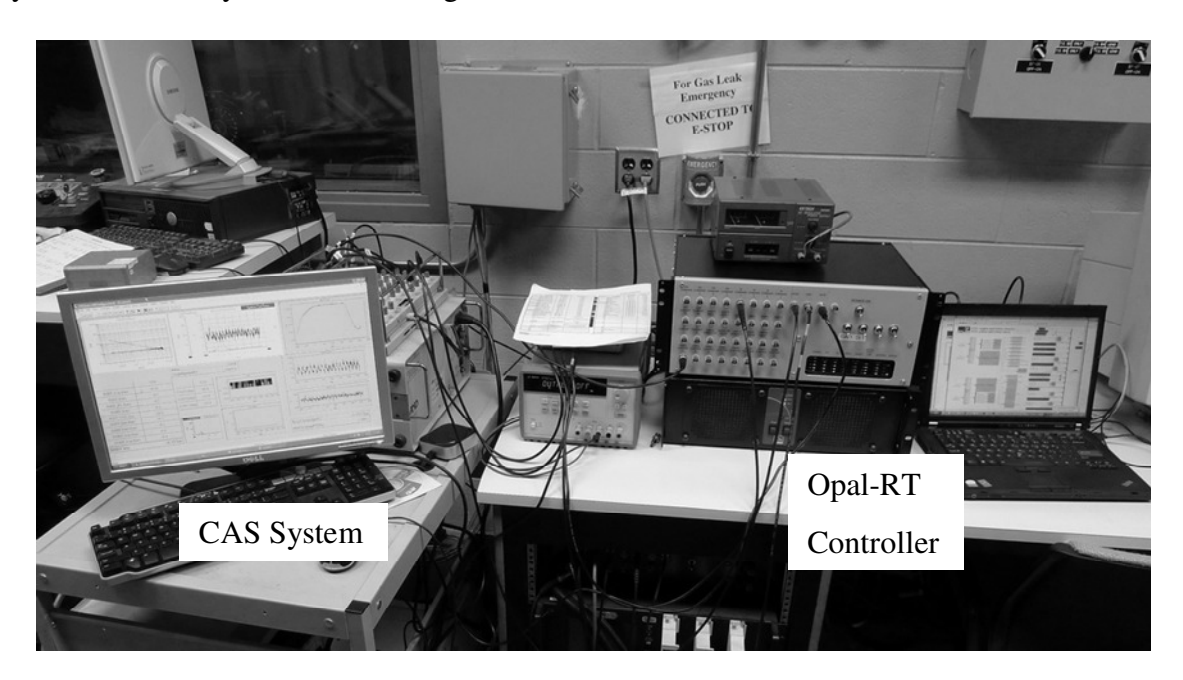


Figure 3-28. Dyno control room

3.9 Engine Dyno Test Results

3.8.1 Closed-loop Identification Setup the Engine Dyno

The selections of PRBS signal and closed-loop control design are very similar to those of the test bench. For the engine dyno test, the PRBS order was selected as 13, with magnitude 15, and a proportional controller gain of 0.1 was used. Similar to the bench test, the model was identified at different engine speeds to obtain a family of VVT models. Both intake and exhaust VVT systems were identified separately at 1200 and 1500 rpm. On the engine, the oil pressure is a function of engine speed and cannot be adjusted from outside. In both of the engine speeds, the engine oil pressure was 40~42 psi. Since the hydraulic VVT system fitted on the engine was very similar to the one that was fitted on the test bench, the order of the identified models was selected to be two. In order to get more accurate models, the feedback cam phase signal was sampled at 4 times per engine cycle during the closed-loop system identification. The rest of the system identification parameters are listed in Table 3-8.

Table 3-8. System identification parameters for engine dyno

Engine Speed (rpm)	1200	1500
Input Sample Rate (ms)	5	5
Output Sample Rate (ms)	25	20
Output/Input Sample Ratio	0.2	0.25
PRBS order	13	13
Signal length (s)	81.88	81.88
Markov parameter. #	100	100
ID open-loop model order	2	2

3.8.2 Closed-loop Identification Results

The closed-loop VVT models were identified and open-loop plant models were calculated using the method same as the one used in the bench identification (3.2). The identified models (Table 3-9) show that at different engine speeds, the system responses are very close to each other. The responses of the intake and exhaust VVT systems are also very similar (Figure 3-29).

Table 3-9. Identified intake and exhaust VVT system models

System	Open-loop Plant Transfer Function
Intake VVT @1200 rpm	$G_{i_1200rpm}(s) = \frac{0.0199s^2 - 27.8s + 911}{s^2 + 7.09s + 34.4}$
Intake VVT @1500 rpm	$G_{e_1200rpm}(s) = \frac{-0.000283s^2 - 13.8s + 675}{s^2 + 5.92s + 20.2}$
Exhaust VVT @1200 rpm	$G_{i_{1500rpm}}(s) = \frac{0.00519s^{2} - 31.2s + 1191}{s^{2} + 8.33s + 46.1}$
Exhaust VVT @1500 rpm	$G_{e_1500rpm}(s) = \frac{0.00609s^2 - 13.4s + 954}{s^2 + 6.34s + 25.8}$

As a result, a single second-order model is used for both intake and exhaust cam phaser at all engine speed for controller design. This approach allows for a simplified controller design process. Three plant models were identified and calculated at each engine speed for both VVT systems, and a nominal second-order model (3.35) was obtained by averaging all the calculated plant models.

$$G = \frac{0.003585s^2 - 21.69s + 900.4}{s^2 + 6.928s + 31.68}$$
 (3.35)

3.8.3 Validation of Identified Model

In order to evaluate the quality of the nominal model, the closed-loop response of the nominal model is compared with the ones from the engine dyno. A proportional gain of 0.1 Volts/degree was used for the step response test. On the engine dyno, a step of 20 degree cam phase change was used as a reference signal. For the nominal model, the step response was simulated in MATLAB. The normalized step responses are compared in Figure 3-30. From Figure 3-30, the nominal model has a very similar transient response to the actual VVT system

response. The DC gain of the normalized model is smaller than the real system. This is mainly due to the length limit of the PRBS excitation signal.

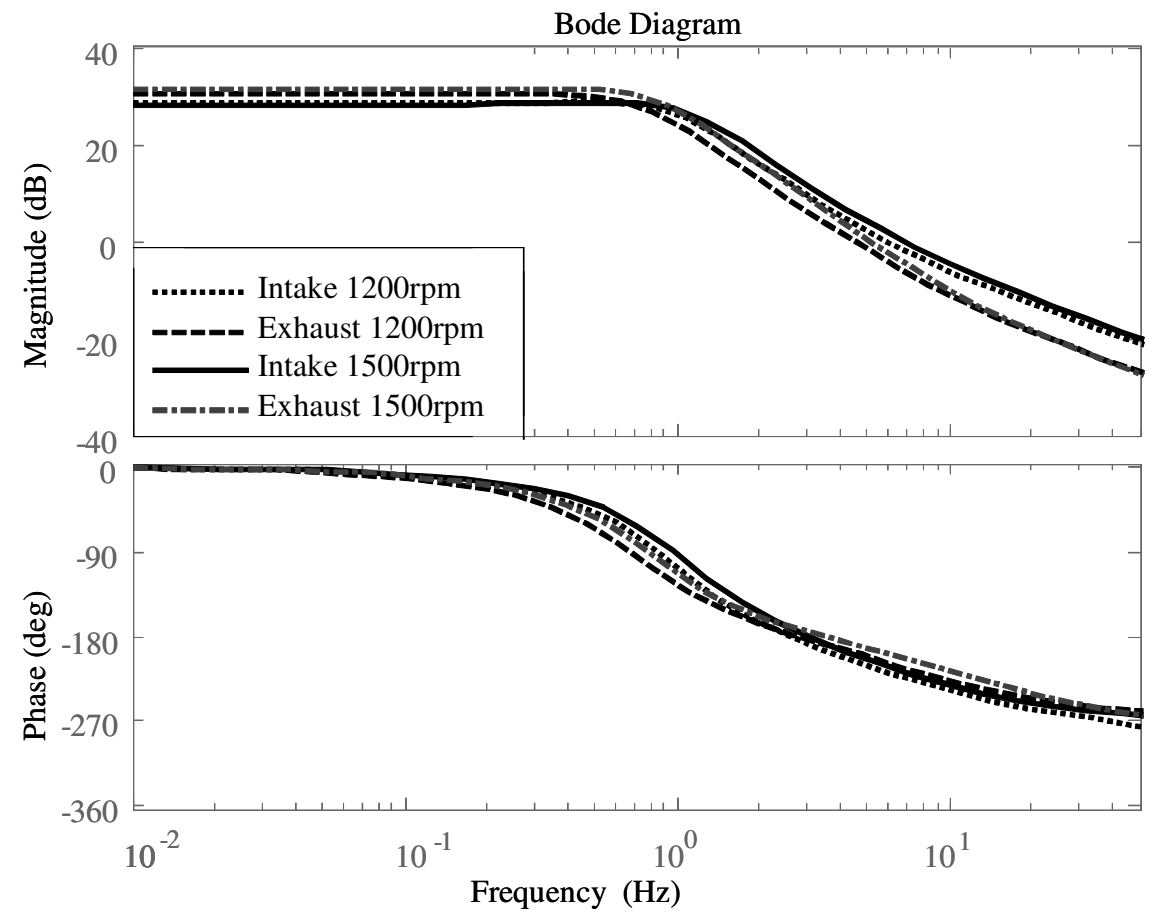


Figure 3-29. Bode diagram for the identified VVT system models

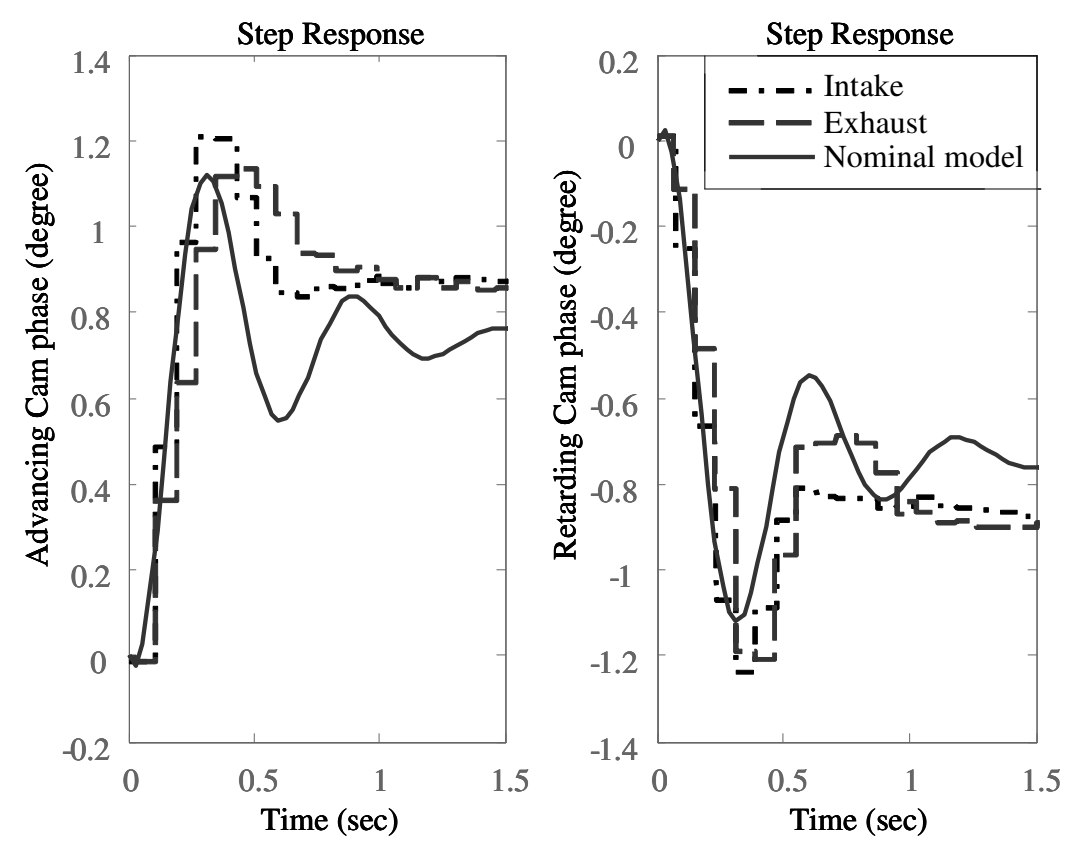


Figure 3-30. Step response of the physical systems and nominal model

3.8.4 Controller Design for VVT System on the Engine Dyno

In this section, an OCC controller was designed and its performance was validated on the engine dyno. Similar to the bench test case, a step input varying between -10 and -30 crank degrees was used as reference signal for both intake and exhaust VVT system. A well-tuned PI controller was used on the engine dyno as a baseline performance comparison to the OCC controller. The PI controller was tuned at different engine speeds to ensure balance between fast response time and low overshoot. The baseline PI controller used on the engine dyno is

$$K_{base} = 0.07 + 0.01s \tag{3.36}$$

For OCC design, system matrices of the nominal plant model were calculated from the transfer function (3.35)

$$\mathbf{A} = \begin{bmatrix} -6.93 & -31.69 \\ 1 & 0 \end{bmatrix} \qquad \mathbf{B} = \begin{bmatrix} 1 \\ 0 \end{bmatrix}$$

$$\mathbf{C} = \begin{bmatrix} -21.7 & 900.7 \end{bmatrix} \qquad \mathbf{D} \cong \mathbf{0}$$
(3.37)

Due to the controller design results from the bench test, an input with an integrator was added to the plant to eliminate the steady-state error. The resulting system matrices of the new multi-input plant are

$$\mathbf{Ap} = \begin{bmatrix} -6.93 & -31.69 & 1 \\ 1 & 0 & 0 \\ 0 & 0 & 0 \end{bmatrix} \qquad \mathbf{Bp} = \mathbf{Dp} \begin{bmatrix} 1 & 0 \\ 0 & 0 \\ 0 & 1 \end{bmatrix}$$

$$\mathbf{Cp} = \mathbf{Mp} = \begin{bmatrix} -21.7 & 900.7 \end{bmatrix} \qquad \mathbf{D} \cong \mathbf{0}$$
(3.38)

Controller design parameters were selected as

$$W_p = 1, \quad V = 0.01, \quad R = diag [1 \ 20]$$
 (3.39)

and resulting OCC controller with integrator is

$$K_{occ} = \frac{119.2s^3 + 1083s^2 + 1503s + 292.4}{s^4 + 265.8s^3 + 1.43 \times 10^4 s^2 + 5281s}$$
(3.40)

Performance tests were conducted at 1200 and 1800 rpm. The intake and exhaust cam phaser responses and control efforts were compared between those of the PI and OCC controllers. Figure 3-31 shows the step response of the closed-loop VVT systems at 1800 rpm with engine combustion. It can be observed that both controllers lead to zero steady-state error, with the steady-state oscillation of less than 1 degree. Both controllers have similar 10~90% rising time of 2 to 3 engine cycles. The main advantage for the OCC controller in this case is that the OCC controller has much less overshoot than that of the PI controller. The OCC controller reduces the response overshoot by more than 50% compared to the PI controller in most cases. Compared to the baseline PI controller, the OCC controller has a longer settling time. Although the OCC controller has a much lower control effort on the test bench, both control efforts on the dyno are

very similar (Figure 3-32). The main reason is that the feedback sample rate on the dyno is much slower than on the bench. The slow sample rate penalizes OCC much more than the PI, because the OCC is a higher order dynamic controller. As a result, the advantage of OCC in control effort is not shown on the engine dyno.

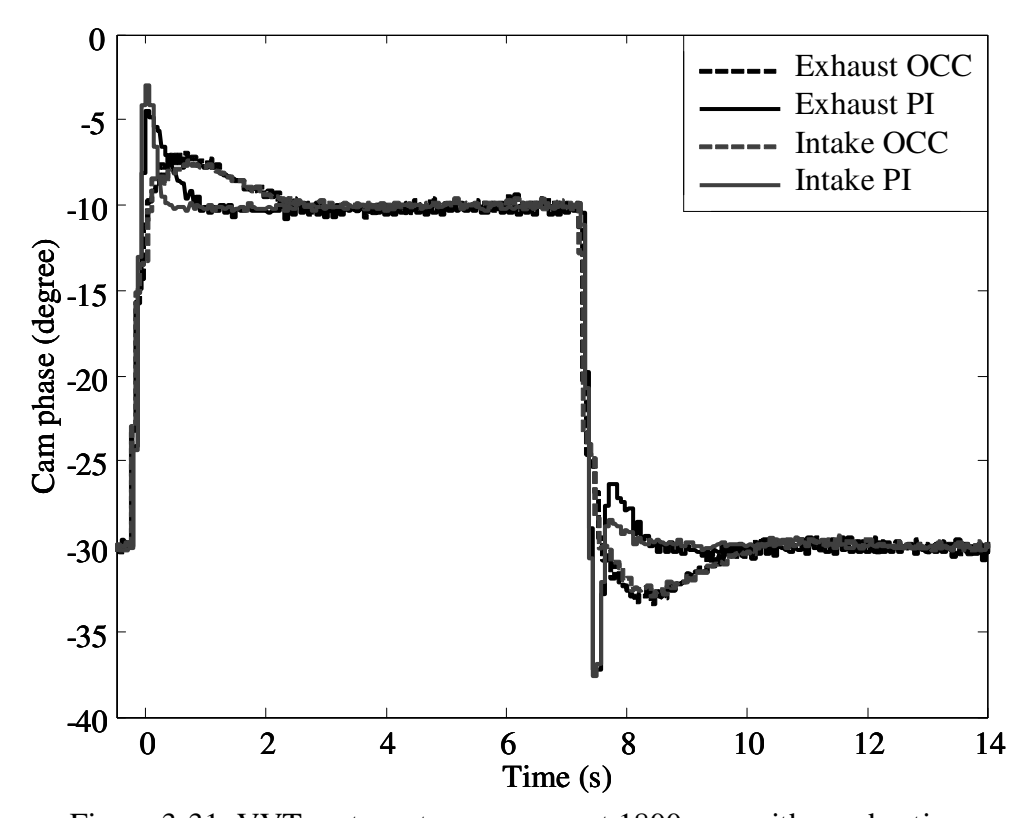


Figure 3-31. VVT system step response at 1800 rpm with combustion

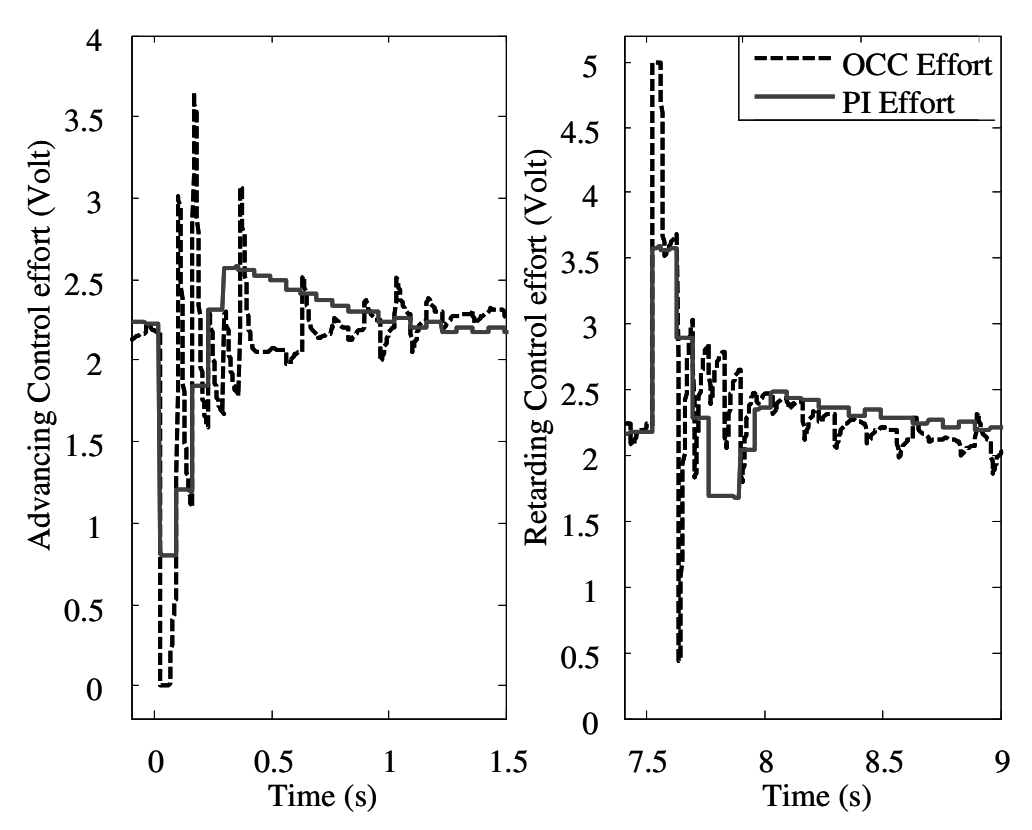


Figure 3-32. VVT control effort on the engine dyno

Table 3-10. Cam phaser performance when motoring

		Advanced Performance							
Engine Speed (rpm)	Cam	Overshoot (deg)		Settling Time (s)		Rising Time (s)			
		PI	OCC	PI	OCC	PI	OCC		
1200	Intake	10.60	3.10	1.00	2.17	0.20	0.20		
1800	Ппаке	7.10	2.50	0.50	2.10	0.13	0.13		
1200	Exhaust	6.90	1.90	0.90	2.30	0.20	0.30		
1800		6.20	3.30	0.90	2.00	0.20	0.20		
	Cam	Retard Performance							
Engine Speed (rpm)		Oversho	ot (deg)	Settling	Time (s)	Rising Time (s)			
		PI	OCC	PI	OCC	PI	OCC		
1200	Intoleo	9.00	2.80	1.70	2.60	0.20	0.20		
1800	Intake	8.00	2.80	1.20	2.60	0.13	0.20		
1200	Exhaust	8.20	2.80	2.90	2.30	0.20	0.20		
1800		8.30	3.40	1.30	2.30	0.13	0.20		

Table 3-11. Cam phaser performance when combusting

		Advanced Performance							
Engine Speed (rpm)	Cam	Oversho	oot (deg)	Settling Time (s)		Rising Time (s)			
		PI	OCC	PI	OCC	PI	OCC		
1200	Intake	9.80	2.90	2.30	2.40	0.20	0.20		
1800	intake	7.10	2.50	0.50	2.20	0.13	0.20		
1200	Exhaust	7.80	2.90	1.50	2.60	0.20	0.20		
1800		5.60	3.00	0.90	2.20	0.13	0.13		
		Retard Performance							
Engine Speed (rpm)	Cam	Overshoot (deg)		Settling Time (s)		Rising Time (s)			
		PI	OCC	PI	OCC	PI	OCC		
1200	Intake	9.00	2.90	1.10	2.70	0.20	0.20		
1800.	intake	7.60	2.90	0.70	2.30	0.20	0.20		
1200	Exhaust	8.10	3.00	2.20	2.30	0.20	0.20		
1800		7.30	3.40	0.90	2.40	0.13	0.20		

3.10 Conclusion

This chapter applies integrated system modeling and control design process to a hydraulic continuously variable valve timing (VVT) actuator system. Constrained by the sample rate of the crank-based cam position sensor (a function of engine speed) and time based control scheme, the actuator control sample rate is different from the cam position sensor sample rate. Due to the cam shaft torque load disturbance and the high actuator open-loop gain, it is also almost impossible to maintain the cam phase at the desired level with an open-loop controller. To obtain an adequate control design model, the closed-loop multi-rate system identification is required. Closed-loop system identification using the PRBS q-Markov Cover was tested on a Hardware-In-the-Loop simulator. The HIL simulation result shows that the closed-loop identification successfully retrieved a lumped plant model, from the control input to the sensor output. The closed-loop identification approach was then applied to obtain open-loop system models of a VVT cam actuator system from a test bench. The proposed closed-loop system identification approach provides models whose time responses are fairly close to bench responses. An output covariance constraint controller was designed based on the identified model and tested on the test bench. The controller utilizes an extra integrator to eliminate the steady-state error. Compared to the PI controller, the multi-input OCC controller uses less energy and has the similar closed-loop response time. OCC controller also reduces response overshoot by up to 50%. A Linear Parameter Varying (LPV) system was developed based on the family of models identified at different operating conditions. The LPV controller has lower control effort and lower overshoot than PI, and has faster settling time than the OCC controller. A hydraulic VVT system was modeled using closed-loop identification method on an engine dynamometer and an OCC controller was designed based on the identified model. It is shown that the closed-loop

identification method was able to retrieve hydraulic VVT system model from a working engine. Similar to the bench results, the OCC controller has a much lower overshoot than PI controller. However, due to the low sampling rate on the engine, the OCC controller does not demonstrate the reduced control effort advantage on the engine dynamometer tests.

Chapter 4 Electric Variable Valve Timing System Modeling and Controller Design

4.1 Introduction

Continuously variable valve timing (VVT) systems used in an internal combustion engine were developed in the nineties [1] and have since been widely used due to the growing fuel economy demands and emission regulations. VVT systems improve fuel economy and reduce emissions at low engine speed, and improve engine power and torque at high engine speed. Conventional electronic-hydraulic VVT ([1], and [2]), also called hydraulic VVT, is the most widely used in the industry today. The hydraulic VVT systems require minor changes when applied to a previously non-VVT valve-train [1], which makes design and engineering relatively easy. However due to its mechanism, the hydraulic VVT system also has its limitations [3]. The response and performance of hydraulic VVT systems are significantly affected by the engine operating conditions such as engine oil temperature and pressure. For instance, at low engine temperature, the hydraulic VVT system cannot be activated and has to remain at its default position so that the cold start performance and emissions cannot be improved [3]. This leads to the study of other variable valve-train systems, such as electromagnetic [4], hydraulic [5], electro-pneumatic [6], and electric motor driven planetary gear system ([7] and [8]). Electric motor driven VVT operational performance is independent of engine oil temperature and pressure [3]. Compared to the hydraulic VVT system, the electric motor driven VVT systems are less limited to engine operating conditions and therefore give better performance and better emission in a wider operational range. Especially, since the electric VVT (EVVT) systems are independent of the engine oil pressure, their response times are greatly improved.

The major advantage of homogeneous charge compression ignition (HCCI) combustion is realized by eliminating the formation of flames. That results in much lower combustion temperature. As a consequence of the low temperature, the formation of NOx (nitrogen oxides) is greatly reduced. The lean burn nature of the HCCI engines also enables un-throttled operation to improve engine fuel economy. Unfortunately, HCCI combustion is feasible only over a limited engine operational range due to engine knock and misfire. To make a HCCI engine work in an automotive internal combustion engine, it has to be capable of operating at both a spark ignition (SI) combustion mode at high load and an HCCI combustion mode at low and medium load ([9] and [10]). This makes it necessary to have a smooth transition between SI and HCCI combustion modes.

Achieving the HCCI combustion and controlling the mode transition between SI and HCCI combustions in a practical engine require implementation of enabling devices and technologies. There are a number of options, and the necessary prerequisite for considering any of them is their ability to provide control of thermodynamic conditions in the combustion chamber at the end of compression. The range of devices under consideration includes variable valve actuation (cam-based or camless), variable compression ratio, dual fuel systems (port and direct fuel injection with multiple fuel injections), supercharger and/or turbocharger, exhaust energy recuperation and fast thermal conditioning of the intake charge mixture, spark-assist, etc. Variable Valve Actuation can be used for control of the effective compression ratio (via the intake valve closing time), the internal (hot) residual fraction via the negative valve overlap (also called recompression) ([11] and [12]), or secondary opening of the exhaust valve (residual reinduction) ([11] and [12]). In addition to providing the basic control of the HCCI combustion, i.e., ignition timing and burn rate or duration, VVT systems play a critical role in accomplishing

smooth mode transitions from SI to HCCI and vice versa ([13], [15], and [16]). In this paper, the EVVT system is selected to control the engine valve timings when it is operated at SI and HCCI combustion modes, and during the combustion mode transition the electric VVT is controlled to track a desired trajectory.

In order to control the electric planetary VVT system, a feedback controller was introduced in [8]. Due to the steady state and transient control accuracy requirements of the HCCI combustion, the closed-loop EVVT system needs not only to meet steady-state performance requirement but also needs to track a desired trajectory during the combustion mode transition. Therefore, a feedback controller with feedforward control was developed in the simulation. In an EVVT system, the cam phase is the integration of speed difference between the electric VVT motor and crankshaft. This leads to using the rate of the reference cam phase as the feedforward command. An Output covariance constraint (OCC) controller ([33], [34], and [35]), an H_2 controller, is used in feedback to reduce the tracking error. Performance of the OCC controller was compared to well-tuned proportional-derivative (PD) controllers, and the OCC controller with feedforward provides better cam phase tracking performance than PD controllers. Different cam phase sample rates were also studied and results show that 4 samples per engine cycle are sufficient for OCC feedback.

The physical based model and simulation results provided a control framework for the EVVT bench. The EVVT system with a local speed controller was mounted on an engine head. An electric motor was used to simulate the crankshaft of the engine. The EVVT pulley was connected to the motor through a timing belt. Closed-loop system identification was used to retrieve a plant model. An OCC controller was designed based on the identified model.

Simulation result shows that OCC has a lower overshoot and lower phase delay than a tuned proportional controller, while having similar or faster response time.

It was also observed from the EVVT bench test that the engine oil viscosity has a large impact on EVVT performance. The engine oil is used to lubricate the planetary gear system. Friction of the engine oil limits the top speed of the EVVT motor. As a result the maximum phasing speed is limited. Two different engine oil viscosity weightings were tested on the test bench. The results show that at room temperature, the EVVT system response is 1.6 times slower using SAE 30 than using SAE 5W20 engine oil.

Modeling and simulation of EVVT introduced in this chapter can be found in [53].

This chapter is organized as following. Section 4.2 describes the electric VVT model and system architecture. Section 4.3 presents the feedforward control strategy and the closed-loop controller design using OCC. Section 4.4 provides the simulation results. EVVT test bench setup is introduced in Section 4.5, and test results are shown in Section 4.6. Section 4.7 investigates engine oil viscosity's impact on EVVT performance. Conclusions are drawn in Section 4.8.

4.2 Modeling

4.2.1 Planetary VVT Components

The planetary gear VVT system studied in this paper consists of four major components (see Figure 4-1). The ring gear, which serves as the VVT pulley, is driven directly by the crankshaft through a timing belt at half crankshaft speed. The planet gear carrier is driven by an electric VVT motor. Planet gears engage both ring and sun gears. The sun gear is connected to the camshaft. The sun and planet gears are passive components that obtain kinetic energy from the carrier and ring gears. Compared to other components, the inertia of engine flywheel and crankshaft is very large. As a result, dynamics of the ring gear is ignored in this study. All other

components have known mechanical properties and their dynamics are considered in the modeling.

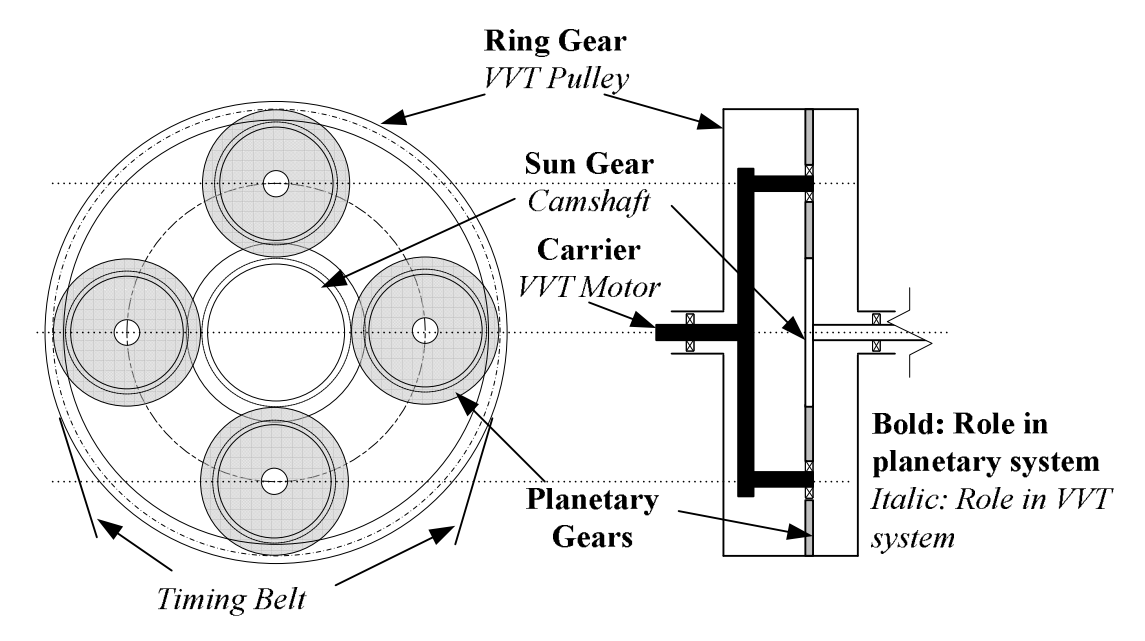


Figure 4-1. Electric planetary gear VVT system

4.2.2 Planetary Gear System Kinematics

In a planetary gear system [54] shown in Figure 4-1, angular velocities of components are determined by

$$\frac{\omega_{S}(t) - \omega_{C}(t)}{\omega_{r}(t) - \omega_{C}(t)} = -\frac{n_{r}}{n_{S}}$$
(4.1)

where ω_s , ω_c , and ω_r are angular velocities of the sun, carrier, and ring gears respectively. n_r and n_s are the teeth numbers of ring and sun gears. Laplace transformation of (4.1) can be expressed as

$$\Omega_{s}(s) = -\frac{n_{r}}{n_{s}}\Omega_{r}(s) + \frac{n_{r}}{n_{s}}\Omega_{c}(s) + \Omega_{c}(s)$$
(4.2)

The cam phase angle ϕ is two times of the integration of the difference between camshaft and crankshaft speeds. That is

$$\phi = 2 \int_0^t [\omega_s(\tau) - \omega_r(\tau)] d\tau \tag{4.3}$$

and its Laplace transformation is

$$\Phi(s) = \frac{2}{s} [\Omega_s(s) - \Omega_r(s)]$$
(4.4)

Substituting (4.2) into (4.4), we have

$$\Phi = \frac{2}{s} \left(\frac{n_s + n_r}{n_s} \right) (\Omega_c - \Omega_r) \tag{4.5}$$

Equation (4.5) shows that the cam phase is an integral function of speed difference between carrier and ring gears. In other words, by controlling the VVT motor speed with respect to the engine speed, the cam phase can be adjusted. When the carrier speed is equal to the ring speed, the cam phase is held; when the carrier speed is greater than the ring speed, the cam phase is advancing; and when the carrier speed is slower than the ring speed, the cam phase is retarding. Notice that equation (4.5) contains an integrator, and the target cam phase reference cannot be used as feedforward control directly.

4.2.3 Planetary Gear System Dynamics

Planetary gear system dynamics with an electric motor are modeled in this section. In this study, the gear system friction is ignored. Figure 4-2 shows free body diagrams of planetary gear components.

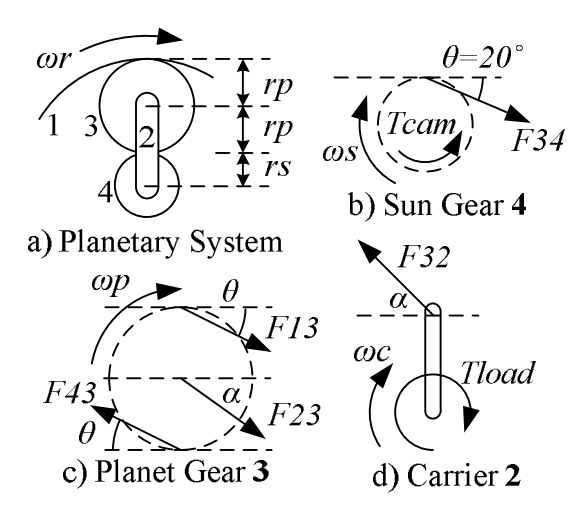


Figure 4-2. Free body diagrams of planetary gear components

Without loss of generality compared to the system in Figure 4-1, the system is treated as having only one planet gear (Figure 4-2a). Since all the gears are properly engaged, we have

$$\frac{n_s}{r_s} = \frac{n_p}{r_p} = \frac{n_r}{r_r}, \quad r_r = 2r_p + r_s \tag{4.6}$$

where n_p is the number of teeth on the planet gear, and r_s , r_p , and r_r are the pitch circle radii of the sun, planet, and ring gears. In this study, the gears use a standard pressure angle θ of 20 degrees. Since the ring has a very large inertia compared to the other components, angular velocity of the ring ω_r is assumed to be constant during the phase shift. From (4.2)

$$\dot{\omega}_{S} = \frac{n_{r} + n_{S}}{n_{S}} \dot{\omega}_{C} \tag{4.7}$$

There are two torques applied to the sun gear (Figure 4-2b). They are camshaft load T_{cam} and torque from tooth force F_{34} .

$$F_{34} \cdot r_s \cdot \cos \theta - T_{cam} = J_s \dot{\omega}_s \tag{4.8}$$

where J_s is sun gear's moment of inertia with respect to its center of gravity.

Two tooth forces (F_{43} and F_{13}) and one bearing force from carrier F_{23} are applied to the planet gear (Figure 4-2c) which rotates around the bearing on the carrier at ω_p

$$\frac{\omega_p(t) - \omega_c(t)}{\omega_s(t) - \omega_c(t)} = -\frac{n_s}{n_p}$$
(4.9)

and from torque balance with respect to bearing point

$$(F_{43} + F_{13}) \cdot r_p \cdot \cos \theta = J_p \dot{\omega}_p \tag{4.10}$$

where \boldsymbol{J}_p is the planet gear's moment of inertia with respect to its center of gravity.

The planet gear also rotates about the center of sun gear. Therefore

$$[F_{13}(2r_r) - F_{43}r_s]\cos\theta + F_{23}(r_p + r_s)\cos\alpha = J_{ps}\dot{\omega}_c$$
(4.11)

where the direction and magnitude of bearing force F_{23} are unknown. The planet gear's moment of inertia with respect to the center of sun gear J_{ps} can be calculated by

$$J_{ps} = J_p[1 + m_p(r_s + r_p)^2]$$
(4.12)

Since the carrier is driven directly by the motor shaft, the carrier's inertia is also considered to be part of motor shaft inertia, and modeled in the next sub-section. Torque balance of the carrier is

$$F_{32}\cos\alpha(r_p + r_s) = T_{load} \tag{4.13}$$

where T_{load} is the mechanical load to the motor shaft and F_{32} is the bearing force from planet gear.

Using (4.7) in (4.8), we have

$$F_{34} \cdot r_s \cdot \cos \theta = J_s \frac{n_r + n_s}{n_s} \dot{\omega}_c + T_{cam}$$
(4.14)

From (4.9) and (4.7)

$$\omega_{p} = -\frac{n_{s}}{n_{p}} \omega_{s} + \frac{n_{s} + n_{p}}{n_{p}} \omega_{c}$$

$$\dot{\omega}_{p} = -\frac{n_{s}}{n_{p}} \frac{n_{r} + n_{s}}{n_{s}} \dot{\omega}_{c} + \frac{n_{s} + n_{p}}{n_{p}} \dot{\omega}_{c}$$

$$= \frac{-n_{r} + n_{p}}{n_{s}} \dot{\omega}_{c}$$
(4.15)

As a result, from (4.10)

$$(F_{43} + F_{13}) \cdot r_p \cdot \cos \theta = J_p \frac{-n_r + n_p}{n_s} \dot{\omega}_c$$
 (4.16)

Use (4.12) and (4.13) in (4.11)

$$[F_{13}(2r_r) - F_{43}r_s]\cos\theta + T_{load} = J_p[1 + m_p(r_s + r_p)^2]\dot{\omega}_c$$
(4.17)

Use (4.14) in (4.16)

$$J_{s} \frac{n_{r} + n_{s}}{n_{s}} \frac{r_{p}}{r_{s}} \dot{\omega}_{c} + \frac{r_{p}}{r_{s}} T_{cam} + F_{13} \cdot r_{p} \cdot \cos \theta = J_{p} \frac{-n_{r} + n_{p}}{n_{s}} \dot{\omega}_{c}$$
(4.18)

Use (4.14) in (4.17)

$$F_{13}(2r_r)\cos\theta - J_s \frac{n_r + n_s}{n_s} \dot{\omega}_c - T_{cam} + T_{load} = J_p [1 + m_p (r_s + r_p)^2] \dot{\omega}_c$$
 (4.19)

Use (4.19) in (4.18)

$$-T_{cam} - \frac{2r_r}{r_s} T_{cam} + T_{load}$$

$$= J_p [1 + m_p (r_s + r_p)^2 - \frac{2r_r}{r_p} \frac{-n_r + n_p}{n_s}] \dot{\omega}_c + J_s (\frac{n_r + n_s}{n_s} \frac{2r_r}{r_s} + 1) \dot{\omega}_c$$
(4.19)

Equations (4.6-4.13) can be simplified as follows.

$$T_{load} = J_{gears} \dot{\omega}_c + kT_{cam} \tag{4.20}$$

where constant J_{gears} is an equivalent inertia of the planetary gear system, and k is a factor of the gear ratio, and

$$J_{gears} = J_p [1 + m_p (r_s + r_p)^2 - \frac{2n_r}{n_p} \frac{-n_r + n_p}{n_s}] + J_s (\frac{n_r + n_s}{n_s} \frac{2n_r}{n_s} + 1)$$

$$k = (1 + \frac{2n_r}{n_s})$$
(4.21)

4.2.4 Electric VVT Motor Dynamics

An electric motor is used to drive carrier in the planetary system. A local closed-loop speed governor is used to control both the motor speed and direction. The input to the local motor controller is the reference speed and direction. In this study, the motor and its controller are treated as an actuator (Figure 4-3). It is modeled with two inputs of motor velocity command and cam load, and one output of motor shaft speed.

The mechanical load of the motor can be modeled [55] as

$$J_c \dot{\omega}_c = \tau - B\omega_c - T_{load} \tag{4.22}$$

where J_c is the moment of inertia of motor shaft and carrier, B is the friction coefficient, and τ is the motor torque. Substituting (4.21) into (4.22) leads to

$$(J_c + J_{gears})\dot{\omega}_c + B\omega_c = \tau - kT_{cam}$$
 (4.23)

and the associated transfer function can be written as

$$\Omega_{c}(s) = \frac{1}{(J_{c} + J_{oears})s + B} [T(s) - kT_{cam}(s)]$$
(4.24)

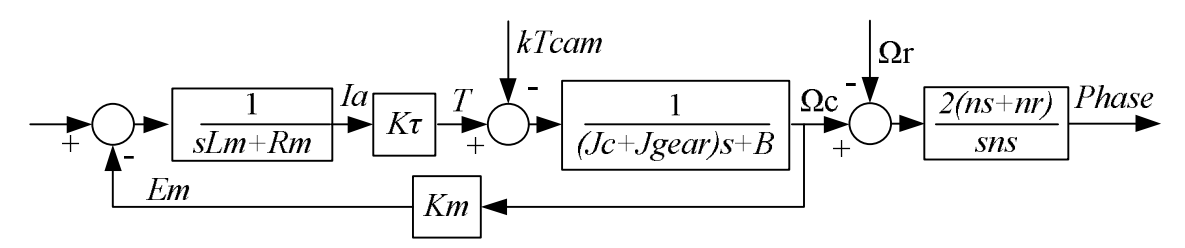


Figure 4-3. Block diagram of electric motor with planetary gear system

The modeling procedure of the electric portion can be found in [55]. Let $J = J_c + J_{gears}$, and the electric motor with planetary gear load (Figure 4-3) can then be represented by

$$\Omega_c(s) = G_e(s)E_a(s) + G_m(s)T_{cam}(s) \tag{4.25}$$

where the voltage input transfer function is

$$G_e = \frac{K_{\tau}}{(L_m s + R_m)(Js + B) + K_{\tau} K_m} \cong \frac{K_{\tau}}{R_m (Js + B) + K_{\tau} K_m}$$
(4.26)

and the mechanical input transfer function is

$$G_m = \frac{-(L_m s + R_m)}{(L_m s + R_m)(J s + B) + K_\tau K_m} \cong \frac{-R_m k}{R_m (J s + B) + K_\tau K_m}$$
(4.27)

and K_{τ} , K_{m} , L_{m} , and R_{m} are the motor parameters representing motor torque constant, back EMF (electric magnetic field) constant, armature inertia and resistance, respectively [55].

4.3 Controller Design

4.3.1 Control Design Parameters

The electric motor VVT system model includes the VVT controller, the local motor controller, motor/planetary dynamics, and planetary kinematics (Figure 4-4). The system parameters are listed as the following and the controllers were designed based on these parameters.

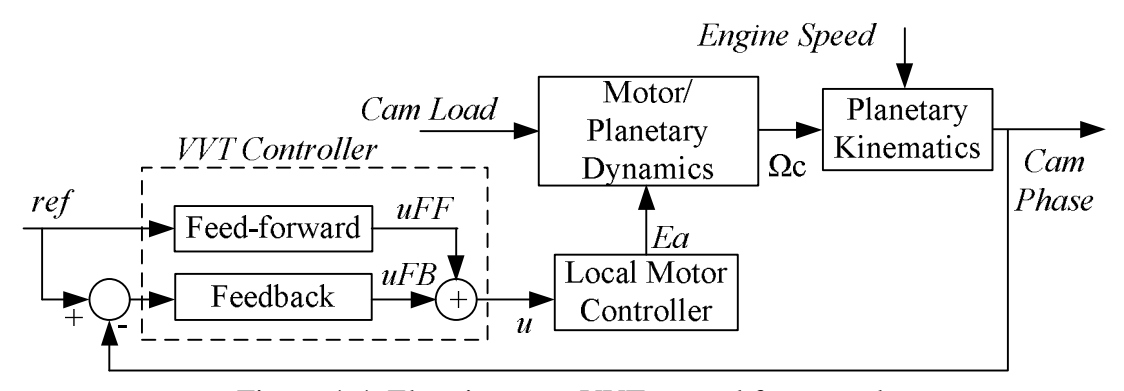


Figure 4-4. Electric motor VVT control framework

The voltage input transfer function is

$$G_e = \frac{45}{0.2s + 1} \tag{4.28}$$

and the mechanical input transfer function is

$$G_m = \frac{-5}{0.2s + 1} \tag{4.29}$$

and the motor has a local PI controller defined by

$$K_{motor} = \frac{s + 0.1}{s} \tag{4.30}$$

Table 4-1. Planetary system parameters

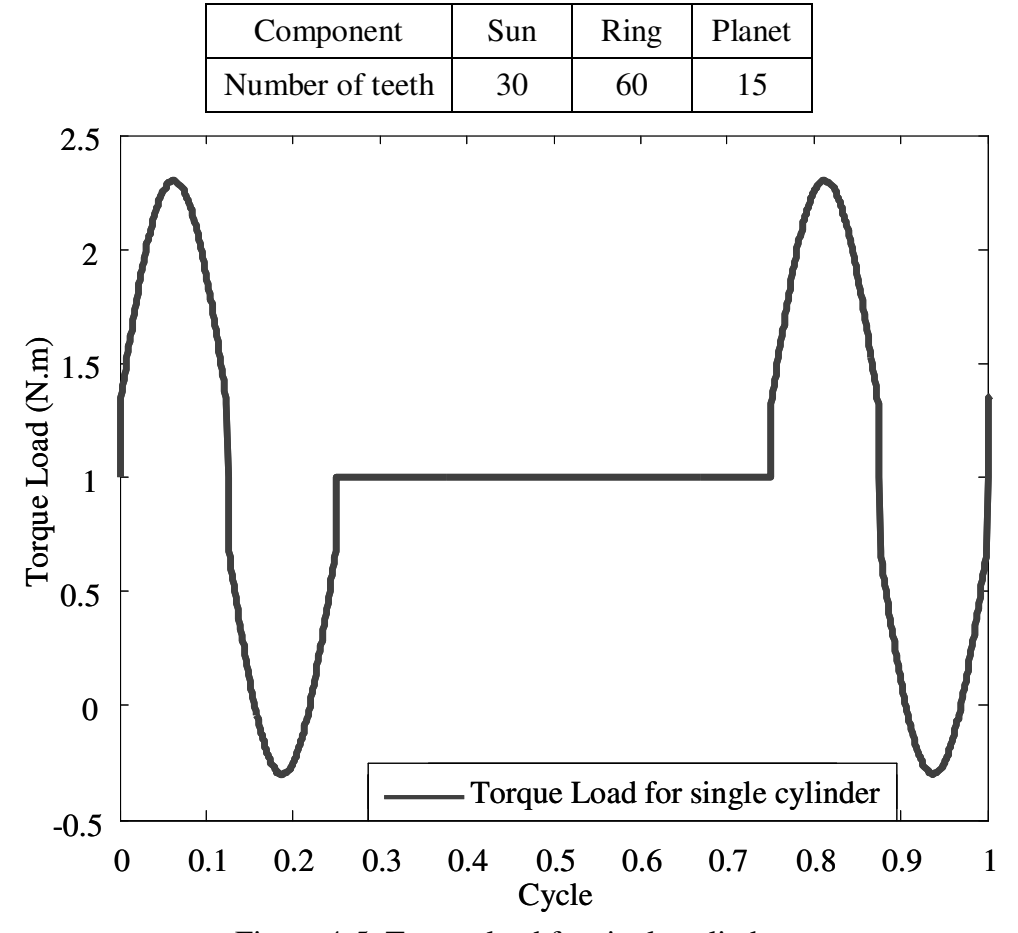


Figure 4-5. Torque load for single cylinder

The teeth numbers of the gear train components are listed in Table 4-1. Substituting these values into (4.5), the planetary kinematics can be represented as

$$\Phi = \frac{6}{s}(\Omega_c - \Omega_r) \tag{4.31}$$

The cam torque load for each cylinder (Figure 4-5) consists of three portions: constant friction load, sinusoidal load representing cam profile, and steps representing the valve spring pre-load. In the study, a 4-cylinder engine is simulated. The total load is a combination of four single-cylinder loads with 180 degree phase shift for each cylinder.

4.3.2 Feedforward Controller

In order to improve the system response, a feedforward controller was employed in the control design. Due to the physical characteristics of the EVVT system stated in the previous section, the reference signal was not used directly as the feedforward; instead, the derivative of the cam phase reference signal was used as a feedforward controller.

The feedforward gain was determined by the ratio between desired cam phase slope and the motor speed. Using (4.21), feedforward gain K_{FF} can be determined as

$$u_{FF} = K_{FF}r\dot{e}f + \omega_r = \frac{1}{6}r\dot{e}f + \omega_r \tag{4.32}$$

where u_{FF} is the feedforward control effort, and $r\dot{e}f$ is the filtered derivative of the reference signal ref

$$r\dot{e}f = \frac{s}{0.05s + 1}ref \tag{4.33}$$

4.3.3 Baseline Controllers

Since the electric phase actuator plant contains an integrator, proportional-derivative (PD) controllers were used as our baseline controllers. These baseline feedback controllers were tuned as performance comparison, where K_1 was tuned without feedforward and K_2 was tuned with feedforward, and they are

$$K_1 = 7 + 0.03s$$

$$K_2 = 1 + 0.005s$$
(4.34)

4.3.4 OCC feedback Controller

For OCC design, considering mechanical cam load as a disturbance, VVT controller output as a plant input, and the cam phase as an output, system matrices of the electric VVT system (Figure 4-4) can then be written as

$$\mathbf{A}\mathbf{p} = \mathbf{A} = \begin{bmatrix} 0 & 225 & 0 & -25 \\ 0 & -230 & 0.1 & 0 \\ 0 & -225 & 0 & 0 \\ 0 & 0 & 0 & -5 \end{bmatrix}, \quad \mathbf{B}\mathbf{p} = \mathbf{B} = \begin{bmatrix} 0 \\ 1 \\ 1 \\ 0 \end{bmatrix}$$

$$\mathbf{C}\mathbf{p} = \mathbf{M}\mathbf{p} = \mathbf{C} = \begin{bmatrix} 6 & 0 & 0 & 0 \end{bmatrix}, \quad \mathbf{D}_{\mathbf{p}} = \begin{bmatrix} 0 & 0 & 0 & 1 \end{bmatrix}^{\mathbf{T}}$$

$$(4.35)$$

The control design parameters were chosen as

$$W_p = 2, V = 0.01, R = [1]$$
 (4.36)

Using the control design algorithm introduced in [35], the resulting OCC controller is

$$K = \frac{-164s^3 - 3.9 \times 10^4 s^2 - 2.9 \times 10^5 s - 2.8 \times 10^4}{s^4 + 298.8s^3 + 1.8 \times 10^4 s^2 + 3.27 \times 10^5 s + 3.25 \times 10^4}$$
(4.37)

4.4 Simulation and Results

Simulations were conducted in Simulink. To simulate the engine valve operation under SI and HCCI transition, the reference signal was selected as a 40 crank degree phase retard that completes in 3 engine cycles. For simplicity, the transition reference signal was divided into three stages with a constant slope. For the first engine cycle the retard phase is 50% (20 degrees), the second cycle is 33.3% (40/3 degrees), and the third 16.7% (20/3 degrees). The phase controller output signal is sampled every 5ms and the feedback signal is updated 4 times per engine cycle. For instance, at 1500 rpm the cam phase is sampled every 20ms. The closed-loop system performance at two engine speeds, 1500 and 2000 rpm, were evaluated.

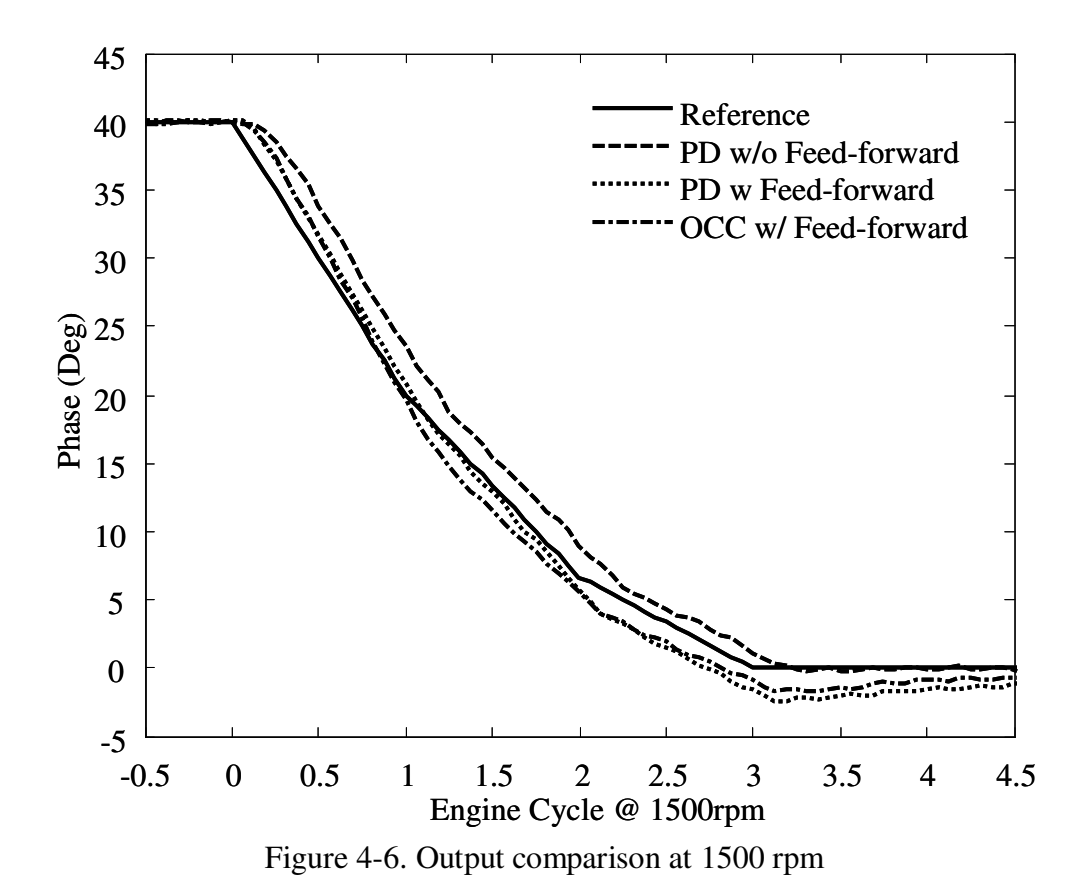


Figure 4-6 compares the cam phase responses between three controllers (OCC, PD with feedforward, and PD without feedforward controllers) at 1500 rpm. It shows that the initial response of the PD controller with feedforward is much faster than the PD controller without feedforward. However, due to the relatively low gain of the PD controller with feedforward, after the second cycle, it has a larger overshoot with longer settling time than the PD controller without feedforward. The OCC controller has the advantage of fast response with small overshoot. Table 4-2 shows output phase angles at the end of each engine cycle after the SI and HCCI transition starts. The OCC controller with feedforward has the lowest overall tracking errors. It is noticed that performance is quite different at different engine speeds of 1500 and 2000 rpm (see Figure 4-7 and Table 4-2) due to the different feedback sampling rates of the cam phase signal at different engine speeds.

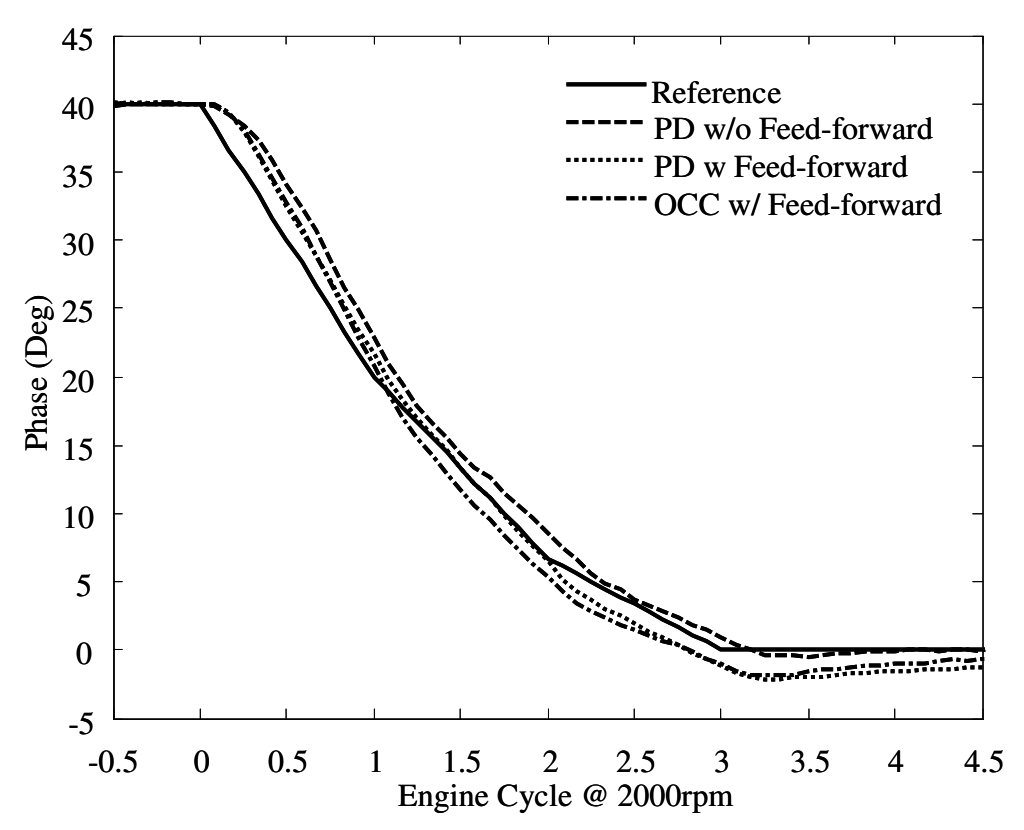


Figure 4-7. Output comparison at 2000 rpm

Table 4-2. Output comparison at end of each cycle

Engine	Cycle	Error (Deg)				
speed	Number	PD	PD w/ ff	OCC w/ ff		
	1	+3.5	+0.9	-0.5		
1500	2	+2.3	-0.8	-1.0		
rpm	3	+1.1	-1.5	-0.9		
	4	-0.1	-1.5	-0.8		
	1	+2.8	+1.6	+1.3		
2000	2	+1.8	-0.2	-0.5		
rpm	3	+0.8	-1.2	-0.6		
	4	-0.1	-1.5	-0.8		

Table 4-3. Output comparison at 1500 rpm with different sample rate

Sampla	Cyclo	Error (Deg)				
Sample Rate	Cycle Number	PD	PD w/ ff	OCC w/ ff		
	1	+2.6	+1.2	+0.3		
8/	2	+1.7	+0.0	-0.3		
cycle	3	+0.9	-0.6	-0.4		
	4	+0.1	-0.9	-0.4		
	1	+2.6	+1.8	+1.0		
16/ cycle	2	+1.8	+0.7	+0.5		
	3	+0.9	-0.1	+0.2		
	4	+0.1	-0.5	+0.0		

As an investigation, the tracking error performances with higher feedback sampling rates were also studied (Table 4-3). The simulation data shows that the tracking error reduces when the sample number increased from 4 samples per engine cycle to 8 samples, but further increment of sample number does not reduce the tracking error significantly. Especially, with the OCC design, the tracking error is fairly small with 4 samples per cycle. Therefore, considering the limited tracking error reduction and increased computational requirement, 4 samples per cycle of the cam phase signal is proper for this application.

4.5 The Electric VVT Bench Setup

In order to model and design a controller for the EVVT actuator system, a test bench was constructed. The test setup was very similar to the hydraulic VVT system bench, except the hydraulic VVT was replaced by an EVVT system. The EVVT system has a phasing range of 45 degrees and is controlled by an AC motor with its own speed governor. An Opal-RT real-time prototype controller adjusts the cam phase by adjusting the reference speed PWM signal sent to

the motor speed governor. The PWM signal frequency is directly proportional to the command rpm and the local motor controller has its cut-off frequencies at both high and low motor speeds.

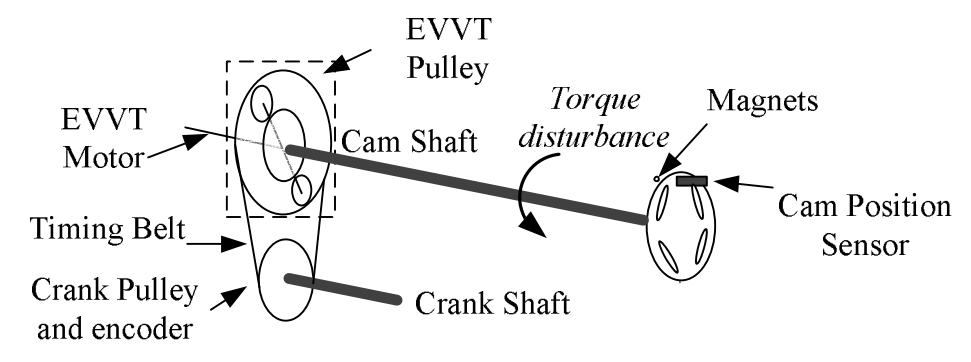


Figure 4-8. EVVT system test bench diagram

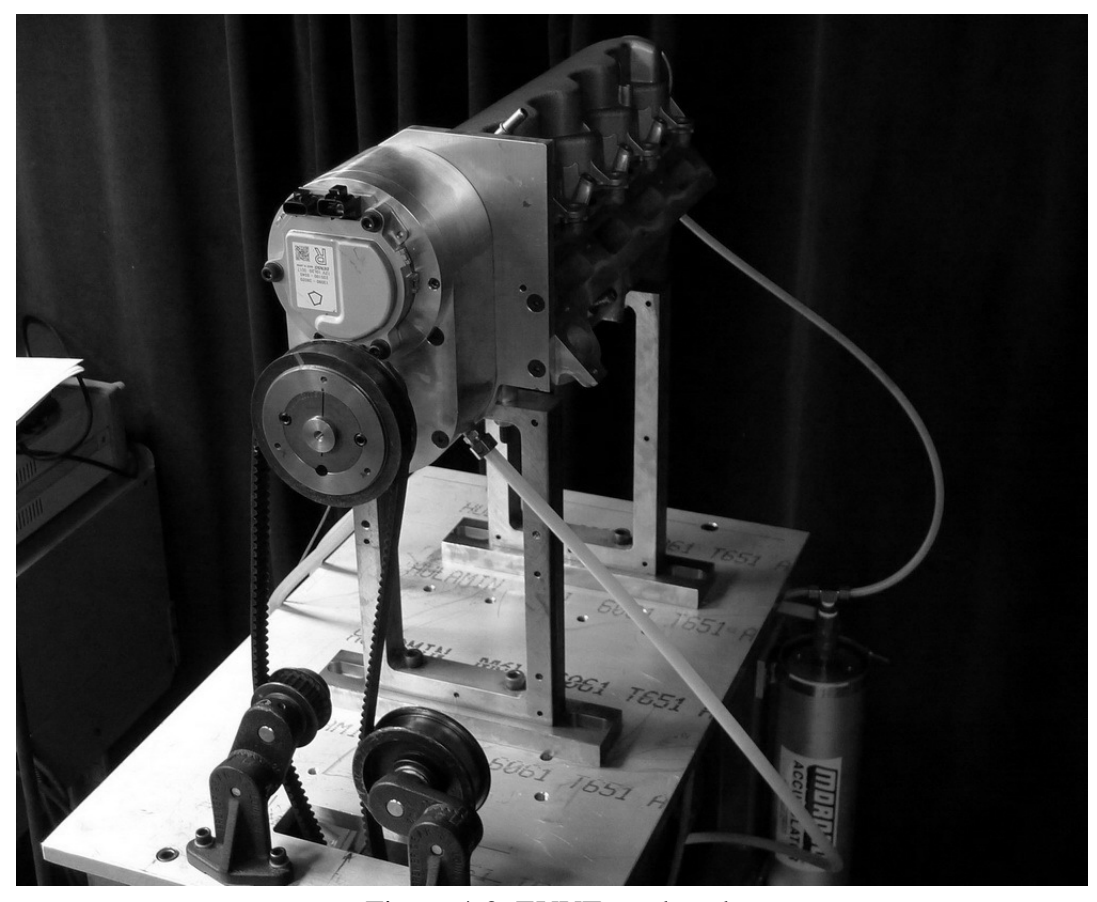


Figure 4-9. EVVT test bench

The Ford 5.4L V8 engine head is the same as the hydraulic test bench. An electric motor is used for simulating the crank shaft of an engine. An encoder was installed on the motor shaft

generates crank angle signal and gate signal (360 degrees per pulse). A cam position magnetic sensor was installed at other side of the engine head. A disc with 4 slot holes was mounted on the extended cam shaft and between the magnetic sensor and the magnet. This setup generates four pulses per engine cycle and the cam position is updated 4 times every engine cycle (Figure 4-8 and Figure 4-9). The cam position sensor system has a theoretical calculation resolution of 1/64 degree. However, it is calibrated manually by using an oscilloscope, so the actual resolution is lower than the theoretical value. An electric oil pump was used to supply oil for cam shaft and planetary gear lubrication. The EVVT bench was running at room temperature (25°C)

4.6 Electric VVT System Test the Test Bench

4.6.1 Closed-loop Identification for Electric VVT System on Test Bench

The bench test of closed-loop system identification process of the EVVT system is very similar to that of the hydraulic system. The main difference is that the engine feedforward speed is used in the system identification process. The main reason is that the EVVT model uses the speed difference between the motor and half engine speed as the input (4.5). The engine speed has much slower dynamics than that of the EVVT system, and can be considered as a constant during the cam phasing. The resulting indentified model has the following form:

$$\Phi = G_{evvt}(s)(u - \frac{1}{2}RPM_{engine})$$
(4.38)

where Φ is the cam phase, $G_{evvt}(s)$ is the identified EVVT model, u is the speed command from the controller and the constant $1/2 \cdot RPM_{engine}$ is half engine speed. The PRBS was used as reference signal for the closed-loop identification and its amplitude was selected to be 10 degrees centered at 20 degrees from the most retarded position. A proportional controller with gain of 70 was used for the system identification.

Table 4-4. Closed-loop identification parameters for the EVVT system

Engine Speed (rpm)	1000	1500
Input Sample Rate (ms)	5	5
Output Sample Rate (ms)	30	20
Output/Input Sample Ratio	0.167	0.25
PRBS order	13	13
Signal length (s)	81.88	81.88
Markov parameter. #	100	100
ID open-loop model order	4	4

Due to the speed limitation on the test bench, the EVVT system was identified at 1000 and 1500rpm. A nominal system model was obtained as

$$G_{evvt}(s) = \frac{-9.72s^3 + 139s^2 + 5760s + 5785}{s^4 + 12.17s^3 + 158.9s^2 - 62.33s + 11.2} (^{\circ}/1000rpm)$$
(4.39)

A proportional controller (4.40) was tuned for performance comparison. The proportional controller was tuned to achieve balance between fast response time and low overshoot at both 1000 and 1500 rpm.

$$K_{evvt-P}(s) = 80(rpm/°) \tag{4.40}$$

4.6.2 Control Design for Electric VVT System Test Bench

An OCC controller was designed for the EVVT system bench. The system plant matrices of the nominal model were obtained from equation (4.39)

$$\mathbf{A}\mathbf{p} = \mathbf{A} = \begin{bmatrix} -12.17 & -158.9 & 62.31 & -11.19 \\ 1 & 0 & 0 & 0 \\ 0 & 1 & 0 & 0 \\ 0 & 0 & 1 & 0 \end{bmatrix} \qquad \mathbf{B}\mathbf{p} = \mathbf{D}\mathbf{p} = \mathbf{B} = \begin{bmatrix} 1 \\ 0 \\ 0 \\ 0 \end{bmatrix}$$

$$\mathbf{C}\mathbf{p} = \mathbf{M}\mathbf{p} = \mathbf{C} = \begin{bmatrix} -9.64 & 139.9 & 5756 & 5783 \end{bmatrix} \qquad \mathbf{D} \cong \mathbf{0}$$

$$(4.41)$$

Controller design parameters were selected as

$$W_p = 1, \quad V = 0.01, \quad R = [1]$$
 (4.42)

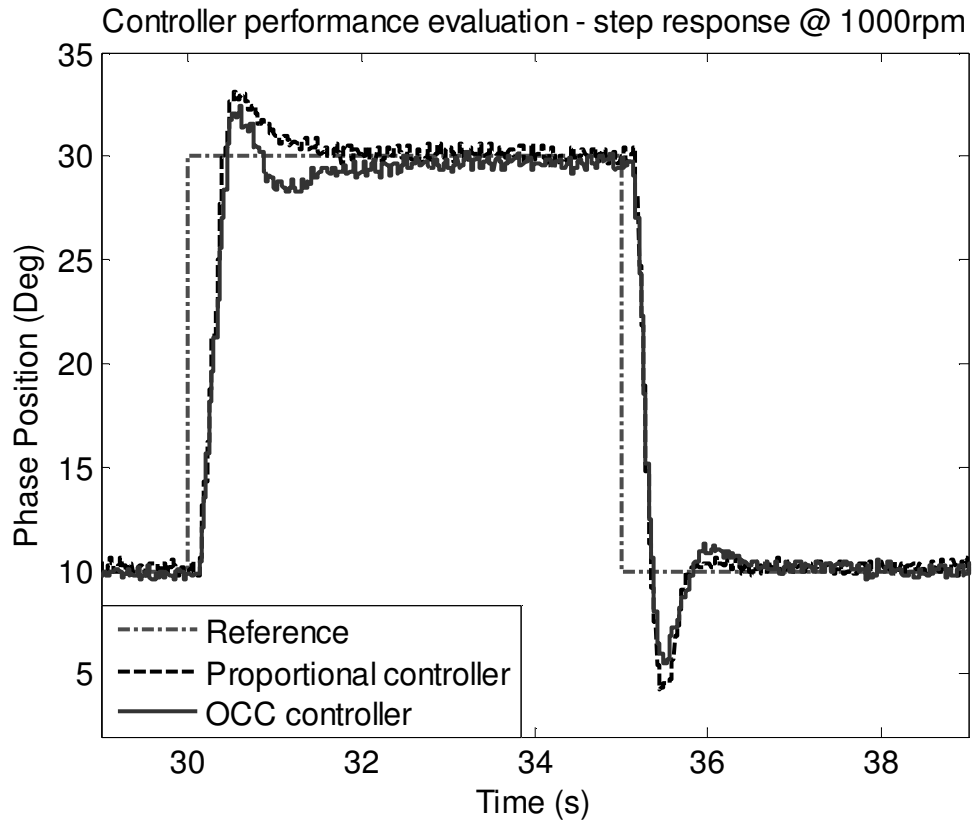
Using the OCC iterative control design algorithm in [35], an OCC controller can be obtained

$$K_{evvt-OCC}(s) = \frac{6.35 \times 10^4 s^3 + 8.465 \times 10^5 s^2 + 1 \times 10^7 s + 6.7 \times 10^7}{s^4 + 147.6s^3 + 6937s^2 + 8.62 \times 10^4 s + 8.17 \times 10^4} rpm/^{\circ}$$
(4.43)

4.6.3 Control Performance Evaluation

The controllers were tested at 1000 and 1500 rpm. Both proportional and OCC controllers have feedforward portions from engine speed as in (4.38). Different reference signals were used to validate the trajectory tracking performance of the EVVT system.

The first reference signal was a square wave ranging from 10 and 30 degrees from most retarded position. As shown in the plots Figure 4-10, both controllers achieves zero steady-state error. The rising time for the proportional controller is almost identical to that of OCC controller at 1000 rpm. At 1500 rpm, both controllers have a similar rising time for the retarded steps, while the OCC controller has a faster rising time than that of the proportional controller. At 1000 rpm, the proportional controller has about 3.5 degrees overshoot for the advancing step and 5.5 degrees overshoot for the retard step. The OCC controller has about 20% less overshoot than the proportional controller at 1000 rpm. At 1500 rpm, the proportional controller has almost zero overshoot, while the OCC controller has overshoot of about 1 degree. Similar to hydraulic VVT, the proportional controller settles faster than the OCC controller, but the OCC controller provides consistent performance over a wider speed range



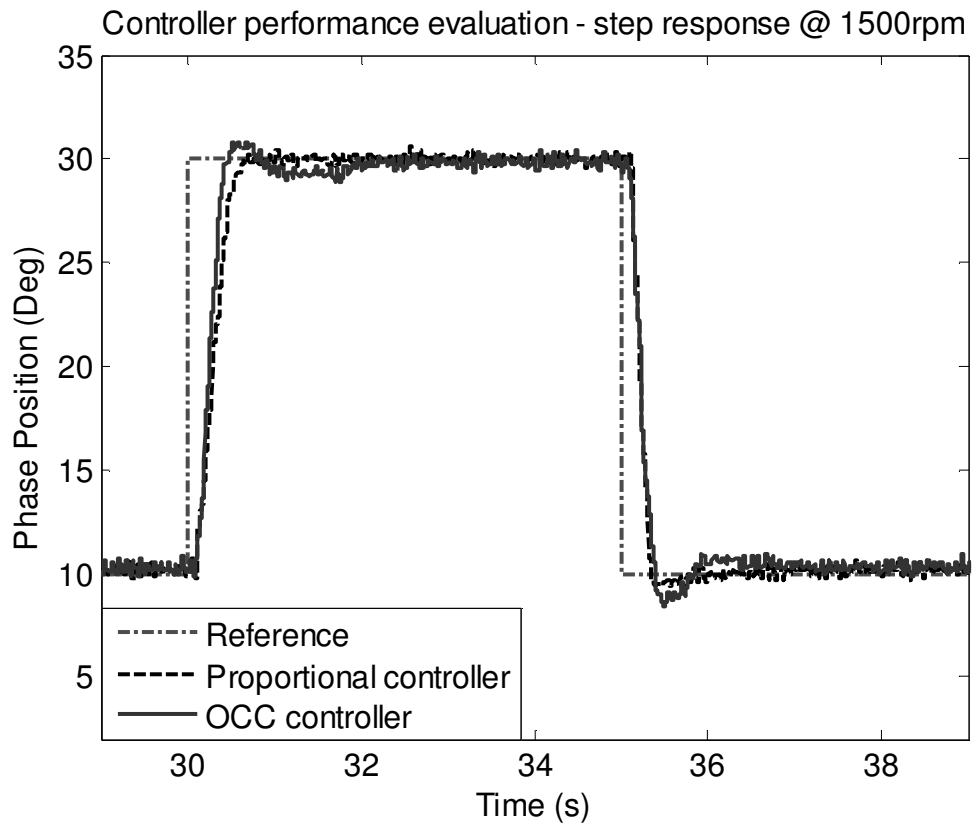
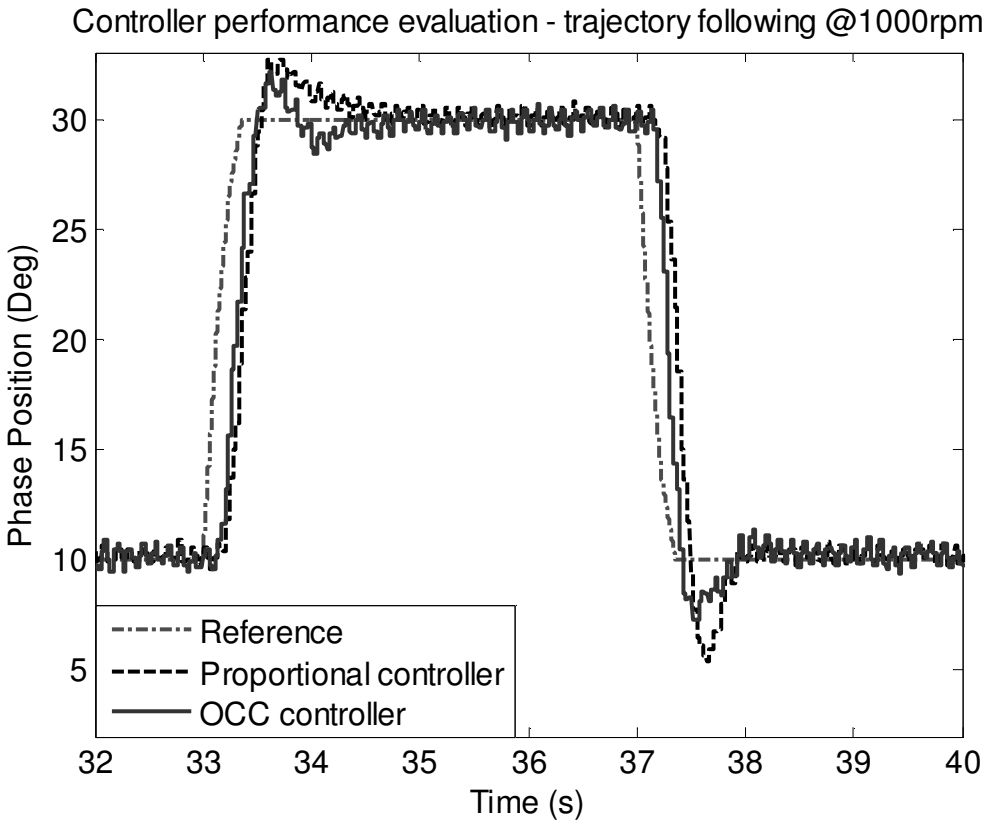


Figure 4-10. Step response comparison on EVVT bench



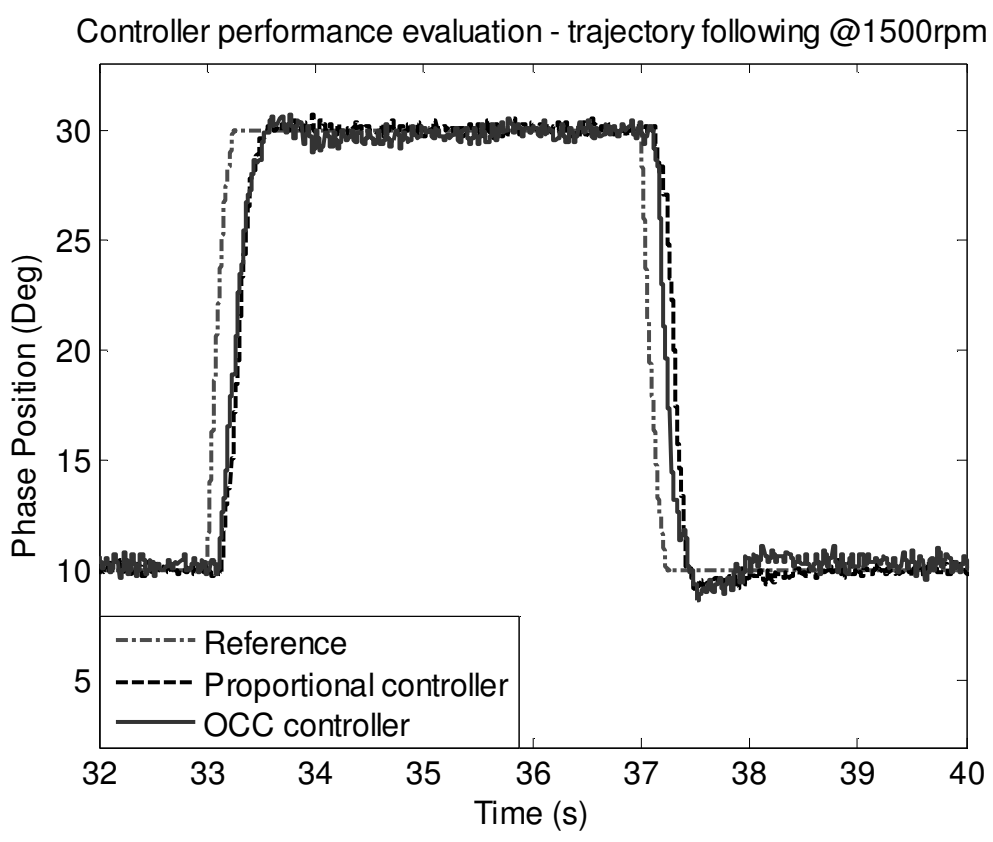


Figure 4-11. Trajectory tracking comparison on EVVT bench

A 20 crank degree phase advance/retard that completes in 3 engine cycles, with the phase changed by 10 (50%), 6.67 (33%) and 3.33 (16.7%), respectively, was also used as reference signal to simulate the phase change during the SI-HCCI mode transition (Figure 4-11). From the plot, it is shown that the OCC controller has less overshoot than the proportional controller at 1000 rpm. At 1500 rpm, overshoots for both controllers are very low. The OCC controller has a faster response time than the proportional controller in both engine speeds. Settling times for the two controllers are also very close to each other.

In order to further investigate trajectory tracking performance for the EVVT controllers, a series of sinusoidal waves was used to test the frequency response of the closed-loop systems. The amplitude of the sinusoidal signal was set to be 10 and centered at 20 degrees from the most retarded position, and the frequencies of the signals vary from 0.01 Hz to 2 Hz. The test results show that both controllers have very good tracking performance at low frequency (Figure 4-12 and Table 4-5). When the excitation frequency increases, both controllers have performance decay. The two controllers have almost identical gains at different frequencies, but the OCC has a lower phase delay compared to the proportional controller.

It is observed that when the engine is running at 1000 rpm, the closed-loop EVVT system has overshoots when the excitation frequency is closed to 1 Hz. After 1.5 Hz, the system gain quickly decays. The identified fourth order nominal model in (4.39) does not show similar behavior at 1 Hz. A seventh order model was obtained using closed-loop identification at 1000 rpm and its predicted performance was compared to the measured data (Figure 4-13). The overshoot of the closed-loop system is able to be duplicated under simulation environment using the identified model at 1000 rpm. However the physical dynamics behind the phenomenon are still unknown and will be investigated in the future.

Table 4-5. Frequency response of close-loop EVVT system

	1000 rpm				1500 rpm			
	Gain		Phase (deg)		Gain		Phase (deg)	
	P	OCC	P	OCC	P	OCC	P	OCC
0.01 Hz	1	1	6	5	1	1	4	4
0.1 Hz	0.98	0.98	21	16	0.97	0.97	21	9
0.2 Hz	0.97	0.96	30	19	0.95	0.96	33	19
0.4 Hz	0.95	0.97	46	30	0.93	0.95	50	21
0.8 Hz	1.18	1.18	74	49	0.96	1.02	66	46
1 Hz	1.33	1.35	94	58	0.95	0.98	87	58
1.5 Hz	1.05	1.04	161	108	0.82	0.78	119	91
2 Hz	0.70	0.72	202	137	0.60	0.61	144	115

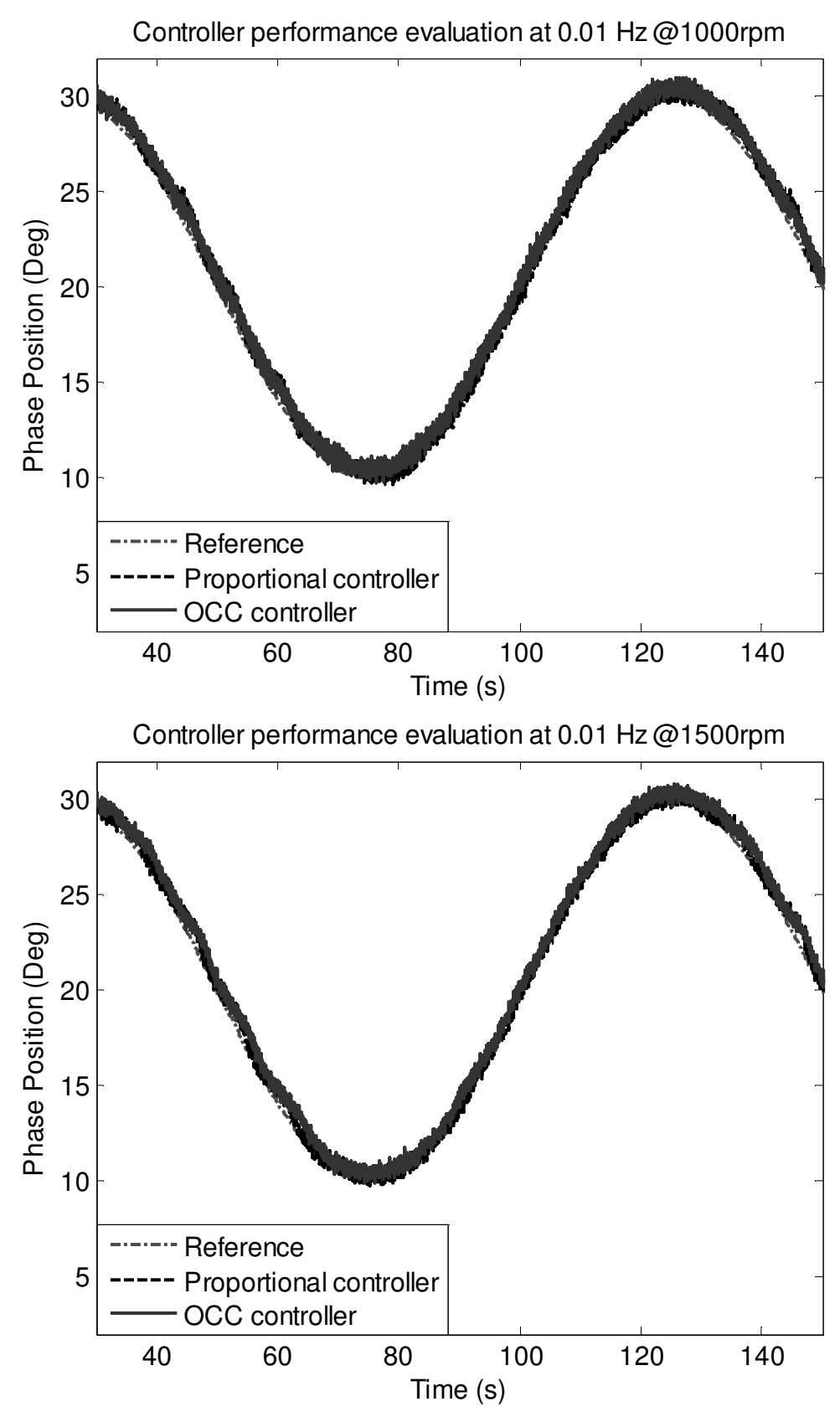


Figure 4-12. Frequency response of the closed-loop EVVT system

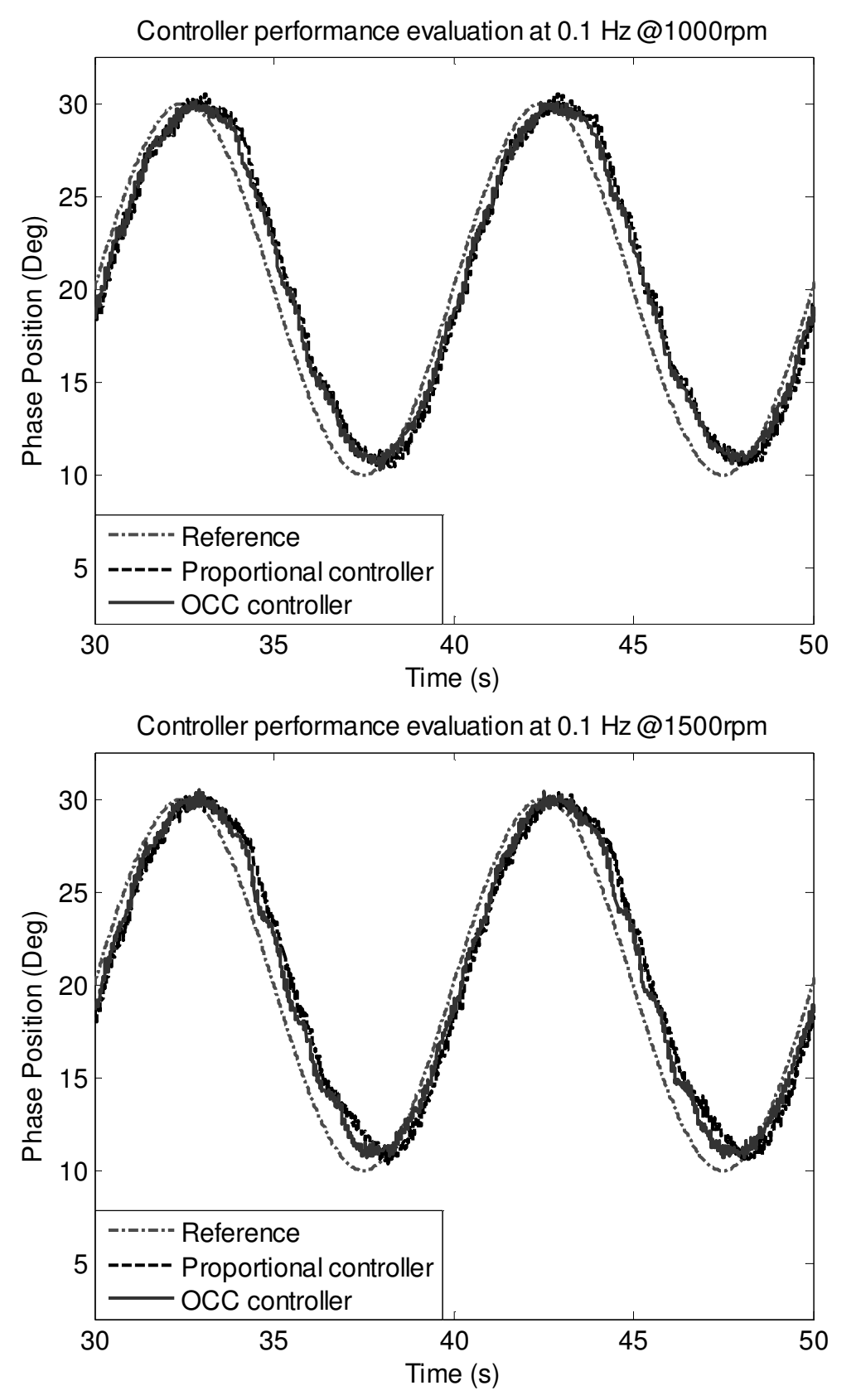


Figure 4-12. Frequency response of the closed-loop EVVT system (continued)

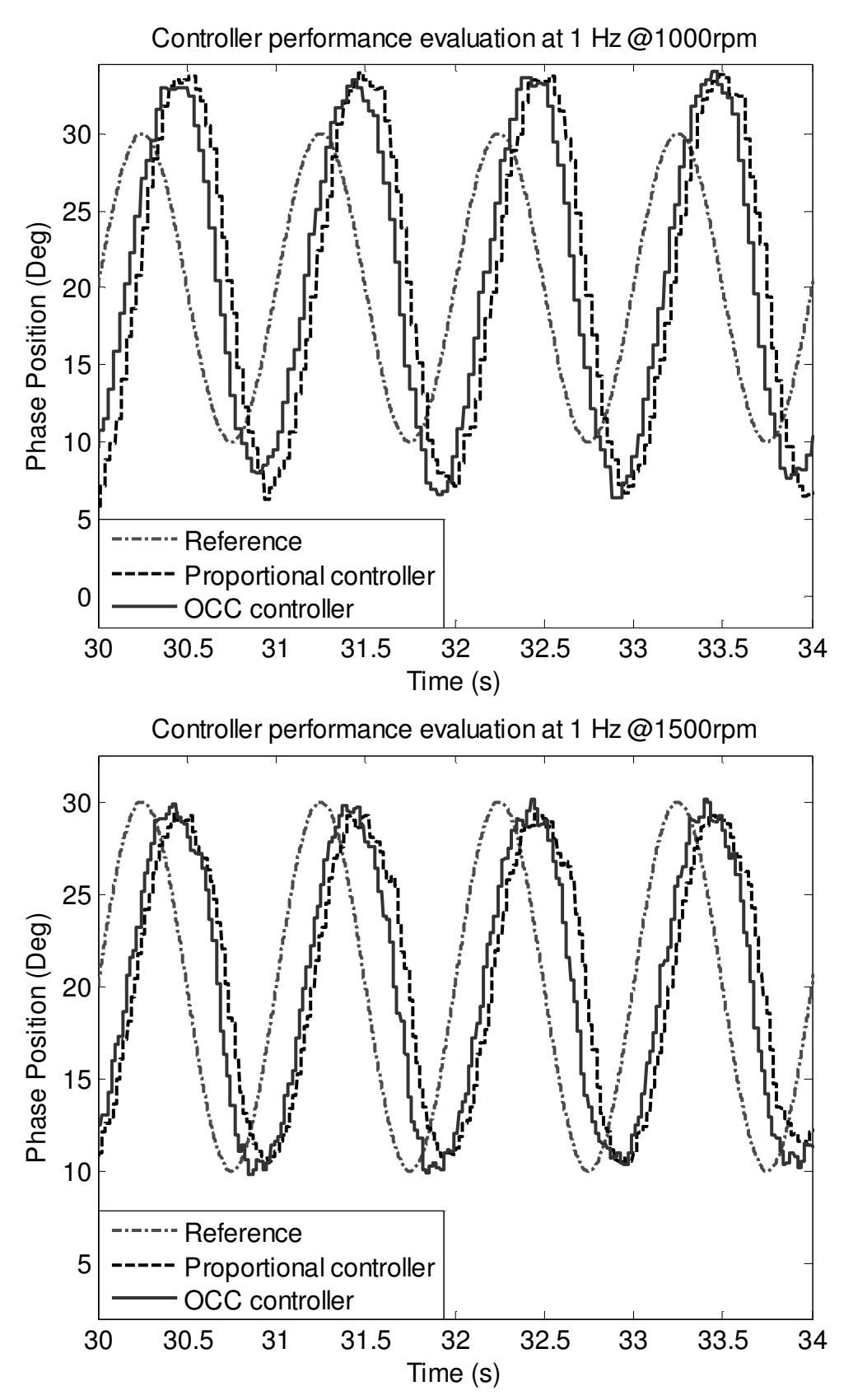


Figure 4-12. Frequency response of the closed-loop EVVT system (continued)

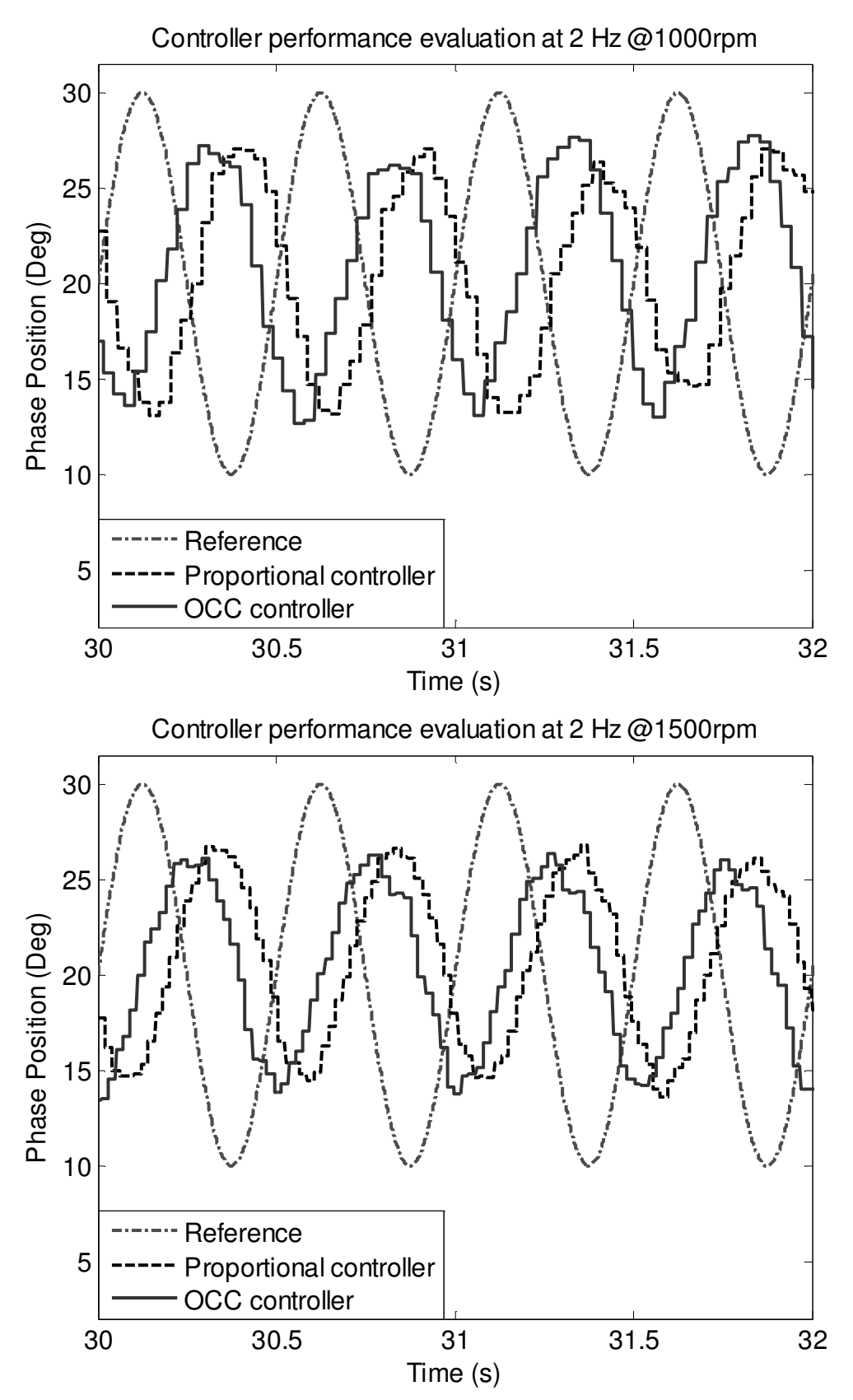


Figure 4-12. Frequency response of the closed-loop EVVT system (continued)

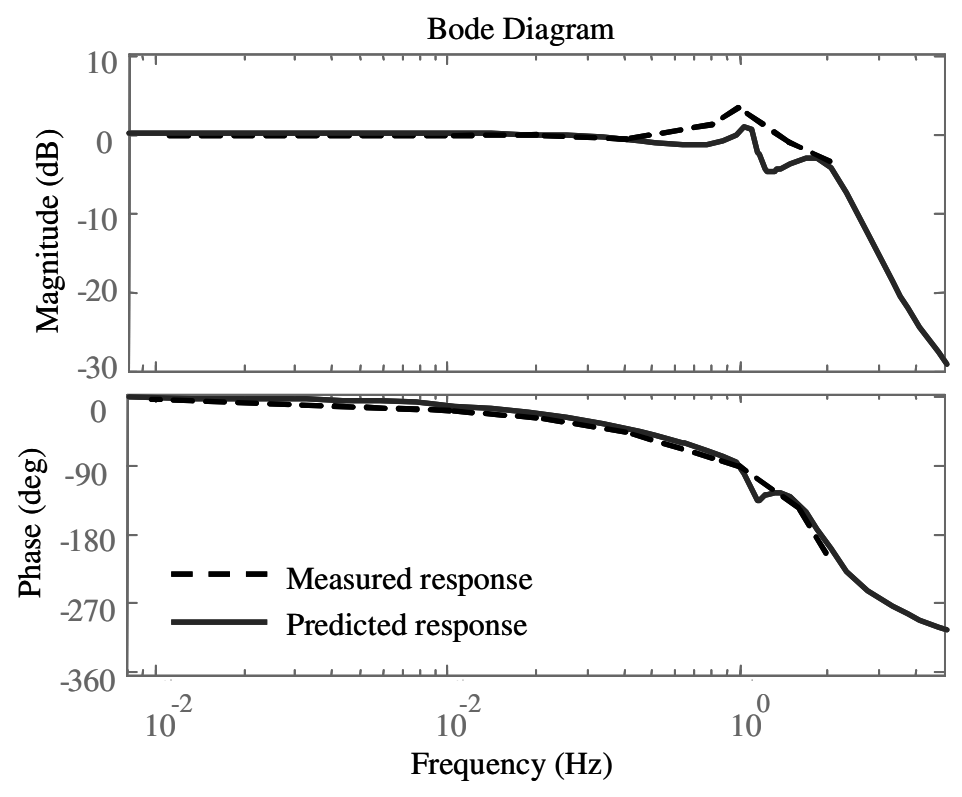


Figure 4-13. Measured and predicted VVT frequency response at 1000 rpm

4.7 Engine Oil Viscosity

Two different types of engine oil, SAE 5W20 and SAE 30, were used during the bench test. The engine was running at 1500 rpm at room temperature (25°C), and OCC controller (4.43) was used in both cases. The reference signal was a 20 degree advance step. The 10 to 90 percent rising time was 0.3 second with SAE 5W20, and 0.48 second with SAE 30 engine oil. The response time difference is due to the friction in the planetary gear system caused by the engine oil viscosity. Figure 4-14 shows the system response and normalized speed difference between the EVVT motor and half engine speed (750 rpm). The VVT motor speed was saturated at 30 units above 750 rpm with SAE 30. With SAE 5W20, the motor speed was saturated at about 50 units above 750 rpm. The system response time is inversely proportional to the difference between the EVVT motor speed and half of the engine speed. Notice that the EVVT motor speed

is measured by calculating PWM frequency from the EVVT local speed controller and has some error (spikes) during the calculation process.

The test result also suggests that the no-friction assumption during the simulation study is not true. On an engine, the nominal operating temperature is much higher than room temperature of the test bench and the engine oil has lower viscosity as a result. The EVVT system will respond much faster when it is installed on an engine than on the test bench.

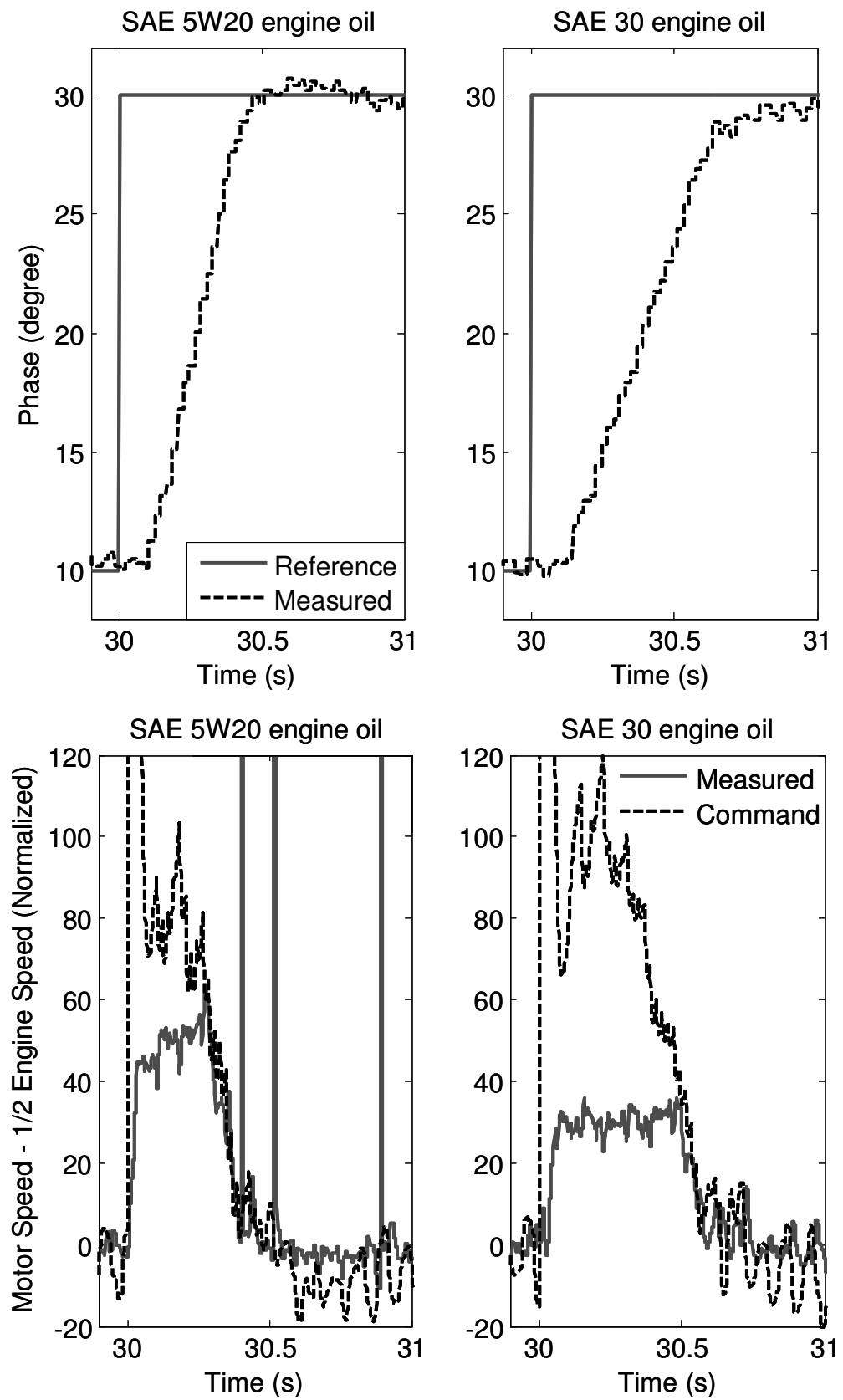


Figure 4-14. Impact of engine oil viscosity on EVVT response

4.8 Conclusion

An electric VVT system with planetary gear train was modeled based upon individual component dynamics and kinematics. A closed-loop OCC control with feedforward control is proposed to reduce the cam phase tracking error during SI and HCCI combustion mode transition. Due to the physical characteristics of the electric VVT system, the filtered derivative of the cam phase reference is used as the feedforward control. Compared to the well-tuned PD controllers, simulation results show that the OCC controller provides fast response with low overshot and low tracking error. It was shown in Simulink environment that with OCC controller the cam phase signal sampled at 4 times per engine cycle is sufficient to meet the maximum tracking error requirement of less than 1.5 degree. The simulation constructed a control framework for the EVVT bench test.

An EVVT system was installed on an engine head and bench tests were conducted. The EVVT system plant model was obtained by using closed-loop system identification. The model has very similar closed-loop response compared to the physical system. An OCC controller was developed based on the identified model. Different signals were used as reference to test the controller performance. The test results showed that the OCC controller has a faster response time compared to a well-tuned proportional controller. The OCC controller performance also has less phase delay than the proportional controller under high frequency sinusoidal reference inputs. The bench test results show that the OCC has a better overall performance and is suitable for using in an HCCI engine.

The impact of engine oil viscosity was also investigated. The test results showed that the engine viscosity has a heavy impact on EVVT response time. When operating at room temperature, the EVVT motor speed is limited by the viscous friction due to the engine oil. As a

result, the system with higher viscosity engine oil (SAE 30 single weight) responds proportionally slower than the system with low viscosity oil (SAE 5W20 weight). The results suggested that it is necessary to use low viscosity engine oil to achieve the maximum performance. This could mean either operating at a high temperature or using low viscosity weight engine oil.

Chapter 5 Conclusions and Future Works

5.1 Conclusions

A low frequency system identification error was discovered when an integral controller was used for PRBS q-Markov Cover closed-loop system identification using an indirect approach. Using the proportional controller in the closed-loop system identification leads to the most accurate plant model. If possible, it is recommended not to use a dynamic integral controller in the closed-loop system identification when PRBS is used as excitations. This study shows that controller setup with a proportional controller is an effective framework for the VVT system closed-loop identification.

Due to the physical properties of the VVT systems, open-loop or single-rate system identification was not feasible. Closed-loop multi-rate system identification is required. Simulation results show that closed-loop identification retrieves plant models representing system dynamics very well. Closed-loop system identification and control design processes were then conducted on hydraulic VVT actuator systems. OCC controllers were designed based on the identified model and tested on test benches and engine dyno with hydraulic VVT systems. The simulation, bench and dyno tests proved that:

- Closed-loop system identification retrieves hydraulic VVT models suitable for controller design purpose.
- The OCC controller demonstrated its advantages of lower overshoot and lower control effort than proportional and integral controller on hydraulic VVT systems.
- With lower feedback sampling rate, the OCC controller still has lower overshoot than the
 PI controller, but its control effort is penalized.

Physical based modeling and simulation was used to construct control framework for the EVVT system. An EVVT system plant model was obtained by using closed-loop system identification on the test bench. OCC controller was designed based on the identified model and tested on the bench. The controller performance was compared with a well-tuned proportional controller. The test results conclude:

- An electric VVT system model was obtained using closed-loop system identification method
- The model based OCC controller has lower overshoot and less phase delay than proportional controller on EVVT systems, while having similar response time.
- The engine oil viscosity has a huge impact on electric VVT system response time. Low viscosity engine oil or high temperature is required for achieving short response time.

5.2 Suggestions for Future Works

The electric VVT system was only tested on the bench and its performance was evaluated at low speed. The performance difference at different engine speed was neglected during modeling and control design process. An engine operates at a much wider speed range than the bench. Due to the kinematics of the EVVT system, its performance varies with the engine speed. For example, as the engine speed increases, the EVVT will have a faster retarding response and a slower advancing response. This difference challenges controller design at higher engine speed and it will be important to test the EVVT system at higher engine speed.

The EVVT system was tested at room temperature (25°C), and its full potential was limited during the bench test. In an engine, the EVVT system will be operating at a higher temperature (95°C). A faster response can be achieved due to the lower engine oil viscosity at higher temperatures. At different engine oil temperature, the maximum EVVT motor speed is

different. Also, the battery voltage at engine start is much lower than standard 13.5 Volts used in the test. The engine speed, engine oil temperature and battery voltage can be included in an LPV system as varying parameters.

During the EVVT bench test, the controller used only engine speed as feedforward portion. On an engine, the controller needs to track arbitrary phase trajectory with as little tracking error as possible. The controller will be able to further reduce tracking error if it contains inverse dynamics of the EVVT plant as feedforward. During the design process, both feedforward and feedback needs to be considered simultaneously, so that optimality is guaranteed with both portions.

Last but not least, the EVVT system will be working with dual-lift valves on the HCCI engine. The camshafts have two switchable cam profiles and switching between the cam profiles introduces torque disturbance to the camshaft. The EVVT controller needs to compensate for the disturbance from switching profile and combustion.

Bibliography

Bibliography

- [1] Y. Moriya, A.Watanabe, H. Uda, H. Kawamura, M. Yoshiuka, M. Adachi, "A Newly Developed Intelligent Variable Valve Timing System Continuously Controlled Cam Phasing as Applied to New 3 Liter Inline 6 Engine", *SAE Technical paper*, 960579, 1996.
- [2] P. H. Dugdale, R. J. Rademacher, B. R. Price, J. W. Subhedar, R. L. Duguay, "Ecotec 2.4L VVT: A Variant of GM's Global 4-Cylinder Engine", *SAE Technical paper*, 2005-01-1941, 2005.
- [3] M. Hattori, T. Inoue, Z. Mashiki, A. Takenaka, H. Urushihata, S. Morino, T. Inohara, "Devalopment of Variable Valve Timing System Controlled by Electric Motor", *SAE Technical paper*, 2008-01-1358, 2008.
- [4] M. Theobald, B. Lequesns, and R. Henry, "Control of Engine Load via Electromagnetic Valve Actuators," *SAE Technical paper*, 940816, 1994.
- [5] Z. Sun, and T. Kuo, "Transient Control of Electro-Hydraulic Fully Flexible Engine Valve Actuation System", *IEEE Transactions on Control Systems Technology*, Vol. 18, No. 3, May, 2010, pp 613-621.
- [6] J. Ma, G. Zhu, and H. Schock, "A dynamic model of an electro-pneumatic valve actuator for internal combustion engines," *ASME Journal of Dynamic Systems, Measurement and Control*, Vol. 132, March, 2010 (DOI: 10.1115/1.4000816).
- [7] R. J. Pierik, J. O. Wilson, "Engine Timing Drive with Fixed and Variable Phasing", U.S. Patent 5,327,859, 1994.
- [8] H. Urushihata, H. Iida, "Variable Valve Timing Control Device of Internal Combustion Engine", U.S. Patent 7,363,896 B2, 2008.
- [9] Zhang, Y., H. Xie, N. Zhou, T. Chen, and H. Zhao, "Study of SI-HCCI-SI Transition on a Port Fuel Injection Engine Equipped with 4VVAS," *SAE Technical paper*, 2007-01-0199, 2007.
- [10] A. Cairns and H. Blaxill, "The Effects of Two-Stage Cam Profile Switching and External EGR on SI-CAI Combustion Transitions," *SAE Technical Paper*, 2007-01-0187, 2007.
- [11] G. M. Shaver, et al, "Dynamic modeling of residual-affected homogeneous charge compression ignition engines with Variable Valve Actuation," *ASME Journal of Dynamics, Measurement, and Control*, Vol. 127, September, 2005, pp. 374-381.
- [12] G. M. Shaver, *Physics based modeling and control of residual-affected HCCI engines using Variable Valve Actuation*, PhD thesis, Stanford University, September, 2005.
- [13] D. Law, D. Kemp, J. Allen, G. Kirkpatrick, T. Copland, "Controlled Combustion in an IC-Engine with a Fully Variable Valve Train", *SAE Technical paper*, 2001-01-0251, 2001.

- [14] M. Ogura, T. Sasaki and Y. Kawaguchi, "HCCI Combustion Control by Intake and Exhaust Continuous Variable Valve Timing Mechanism in Premixed Gasoline Engine", *SAE Technical paper*, 2004-32-0096, 2004
- [15] N. Milovanovic, R. Chen, J. Turner, "Influence of the Variable Valve Timing Strategy on the Control of a Homogeneous Charge Compression (HCCI) Engine", *SAE Technical paper*, 2004-01-1899, 2004.
- [16] F. Agrell, H. Angstrom, B. Eriksson, J. Wikander, J. Linderyd, "Integrated Simulation and Engine Test of Closed Loop HCCI Control by Aid of Variable Valve Timings", *SAE Technical paper*, 2003-01-0748, 2003.
- [17] X. Yang, Modeling and Control of SI and SI-HCCI Hybrid Combustion Engines, PhD dissertation, Michigan State University, 2011
- [18] J. Poole, J. Patton, B. Goodwin, "Modeling and Simulating a VVT System for Robust Design", *SAE Technical paper*, 2008-01-0901, 2008
- [19] G. I. Gustavsson, L. Ljung, and T. Soderstorm, "Identification of process in closed-loop identifiability and accuracy aspects," *Automatica*, Vol. 13, pp59-75.
- [20] M. Leskens, L. B. M. Van Kessel, and P. M. J. Van den Hof, "MIMO closed-loop identification of an MSW incinerator," *Control Engineering Practice*, Vol. 10, pp.315-326.
- [21] U. Forssel and L. Ljung, "Closed-loop identification revisited", *Automatica*, 35, pp. 1215-1241, 1999
- [22] P. M. J. Van Den Hof, and R. J. P. Schrama, "Identification and control closed-loop issues", *Automatica*, Vol. 31, No. 12, pp. 1751-1770, 1995.
- [23] R. E. Skelton and B.D.O. Anderson, "Q-Markov covariance equivalent realization," *International Journal of Control*, Vol. 53, No. 1, 1986
- [24] K. Liu and R. E. Skelton, "Identification and control of NASA's ACES structure," *Proceedings of American Control Conference*, Boston, Massachusetts, USA, 1991.
- [25] G. G. Zhu, R. E. Skelton, and P. Li, "Q-Markov Cover identification using pseudo-random binary signals," *International Journal of Control*, Vol. 62, No. 1, 1995, pp. 1273-1290.
- [26] G. Zhu, "Weighted multirate q-Markov Cover identification using PRBS an application to engine systems," *Mathematical Problems in Engineering*, Vol. 6, pp. 201-224, 2000.
- [27] M. Jung and K. Glover, "Calibratable Linear Parameter-Varying Control of a Turbocharged Diesel Engine," *IEEE Transactions on Control System Technology*, vol. 14, no. 1, pp. 45-62, 2006

- [28] X. Wei and L. del Re, "Gain Scheduled H_{∞} Control for Air Path Systems of Diesel Engines Using LPV Techniques," *IEEE Transactions on Control Systems Technology*, vol. 15, no. 3, pp. 406–415, 2007.
- [29] J. Salcedo and M. Martnez, "LPV identification of a turbocharged diesel engine," *Applied Numerical Mathematics*, vol. 58, pp. 1553-1571, 2008
- [30] R. A. Zope, J. Mohammadpour, K. M. Grigoriadis, and M. Franchek, "Air-fuel ratio control of spark ignition engines with TWC using LPV techniques," *Proceedings of ASME Dynamic System and Control Conference*, 2009
- [31] F. Zhang, K. M. Grigoriadis, M. A. Franchek, and I. H. Makki, "Linear Parameter-Varying Lean Burn Air-Fuel Ratio Control for a Spark Ignition Engine," *Journal of Dynamic System, Measurement and Control*, vol. 192, pp. 404-414, 2007
- [32] A. U. Genc, Linear Parameter-Varying Modelling and Robust Control of Variable Cam Timing Engines, Ph.D. dissertation, University of Cambridge, 2002
- [33] G. Zhu, R. E. Skelton, "Integrated Modeling and Control for the Large Spacecraft Laboratory Experiment Facility", *Journal of Guidance, Control and Dynamics*, Vol. 17, No. 3, pp. 442-450, 1994
- [34] G. Zhu, K. M. Grigoriadis, R. E. Skelton, "Covariance Control Design for Hubble Space Telescope", *Journal of Guidance, Control and Dynamics*, Vol. 18, No. 2, pp. 230-236, 1995
- [35] G. Zhu, M. A. Rotea, R. Skelton, "A Convergent Algorithm for the Output Covariance Constraint Control Problem", *SIAM J. Control Optim.*, Vol. 35, No.1, pp. 341-361, 1997
- [36] A. White, J. Choi, R. Nagamune, and G. Zhu, "Gain-scheduling control of port-fuel-injection processes", *IFAC Journal of Control Engineering Practice*, 2010, DOI: 10.1016/j.conengprac.2010.12.007
- [37] A. White, G. Zhu and J. Choi, "Hardware-in-the-loop Simulation of Robust Gain-Scheduling Control of Port-Fuel-Injection Processes," *IEEE Transaction on Control System Technology*, 2010, DOI: 10.1109/TCST.2010.2095420
- [38] Z. Ren, G. G. Zhu, "Pseudo-random binary sequence closed-loop system identification error with integration control", *Journal Proceedings of the Institution of Mechanical Engineers, Part I: Journal of Systems and Control Engineering*, Vol. 233, pp877-884, 2009
- [39] W. W. Peterson, *Error Correcting Coding*, MIT Technical Press, Cambridge, Massachusetts, USA, 1961
- [40] P. Van Den Hof, "Closed-loop issues in system identification," *Annual Reviews in Control*, 22, pp. 173-186, 1998.

- [41] L. Ljung, System Identification Theory for the User, second edition, Prentice Hall PTR, 1999
- [42] R. Simpson, "Worm gear driven variable cam phaser," US Patent 6622667, 2003
- [43] Z. Ren, G. Zhu, "Multi-rate closed-loop system identification of a variable valve timing actuator for an internal combustion engine," *Proceedings of 2010 American Control Conference*, Baltimore, MD, June-July 2010
- [44] Z. Ren, G. Zhu, "Integrated System Identification and Control design for an IC engine variable valve timing system," *ASME Journal of Dynamic Systems, Measurement, and Control*, 2011, DOI: 10.1115/1.4003263
- [45] A. White, Z. Ren, G. Zhu, and J. Choi, "Mixed H_2/H_∞ Observer-Based LPV Control of a Hydraulic Engine Cam Phasing Actuator", accepted by *IEEE Transactions on Control Systems Technology*, 2011
- [46] B. Codrons, B. D. O. Anderson, M.Gevers, "Closed-loop identification with an unstable or nonminimum phase controller," *Automatica*, 38, pp. 2127-2137, 2002
- [47] B. D. O. Anderson, R. E. Skelton, "The Generation of all q-Markov Covers", *IEEE Transactions on Circuits and Systems*, Vol. 35, No. 4, pp. 375-384, 1988
- [48] A. M. King, U. B. Desai, R. E. Skelton, "A Generalized Approach to q-Markov Covariance Equivalent Realization for Discrete Systems", *Automatica*, Vol. 24, No. 4, pp. 507-515, 1988
- [49] S. Meerkov, T. Runolfsson, "Output residence time control", *IEEE Trans. Automat. Control*, 34, pp. 1171-1176, 1989
- [50] D. A. Wilson, Convolution and Hankel, "Operator norms for linear systems", *IEEE Trans. Automat. Control*, 34, pp. 94-97, 1989
- [51] G. Zhu, M. Corless, R. Skelton, "Robustness properties of covariance controllers", in *Proceedings of Allerton Conf.*, Monticello, IL, 1989
- [52] A. G. Stefanopoulou, J. S. Freudenberg, J. W. Grizzle, "Variable Camshaft Timing Engine Control", *IEEE Transactions on Control Systems Technology*, Vol. 8, No.1, pp. 23-34, 2000
- [53] Z. Ren, G. Zhu, "Modeling and control of an electric variable valve timing system for SI and HCCI combustion mode transition", *Proceedings of 2011 American Control Conference*, San Francisco, CA, June-July 2011
- [54] J. E. Shigley, and C. R. Mischke, *Mechanical Engineering Design*, 6th Edition, McGraw-Hill, 2001.

[55] C. L. Phillips, and R. D. Harbor, *Feedback Control System*, 4th Edition, Prentice Hall, 2000.